INSTITUTO POTOSINO DE INVESTIGACIÓN CIENTÍFICA Y TECNOLÓGICA, A.C.

POSGRADO EN CIENCIAS APLICADAS

Magnetism of carbon nanostructures and *in situ* TEM dynamic transformations of carbon-based nanomaterials

Tesis que presenta

Julio Alejandro Rodríguez Manzo

Para obtener el grado de

Doctor en Ciencias Aplicadas

En la opción de

Nanociencias y Nanotecnología

Codirectores de la Tesis:

Dr. Humberto Terrones Maldonado
Dr. Mauricio Terrones Maldonado
Dr. Florentino López Urías

San Luis Potosí, S.L.P., febrero de 2007.

Constancia de aprobación de la tesis

La tesis **Magnetism of carbon nanostructures and *in situ* TEM dynamic transformations of carbon-based nanomaterials** presentada para obtener el Grado de Doctor en Ciencias Aplicadas en la opción Nanociencias y Nanotecnología fue elaborada por **Julio Alejandro Rodríguez Manzo** y aprobada el **1 de febrero de 2007** por los suscritos, designados por el Colegio de Profesores de la División de Materiales Avanzados del Instituto Potosino de Investigación Científica y Tecnológica, A.C.

_____
Dr. Humberto Terrones Maldonado
Codirector de la tesis

_____
Dr. Mauricio Terrones Maldonado
Codirector de la tesis

_____
Dr. Florentino López-Urías
Codirector de la tesis

_____
Dr. Emilio Muñoz Sandoval
Comité tutorial

Créditos institucionales

Esta tesis fue elaborada en la División de Materiales Avanzados del Instituto Potosino de Investigación Científica y Tecnológica, A.C., bajo la codirección de los doctores Humberto Terrones Maldonado, Mauricio Terrones Maldonado y Florentino López-Urías.
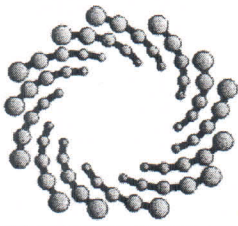
Instituto Potosino de Investigación Científica y Tecnológica, A.C.

Acta de Examen de Grado

El Secretario Académico del Instituto Potosino de Investigación Científica y Tecnológica, A.C., certifica que en el Acta 021 del Libro Primero de Actas de Exámenes de Grado del Programa de Doctorado en Ciencias Aplicadas en la opción de Nanociencias y Nanotecnología está asentado lo siguiente:

En la ciudad de San Luis Potosí a los 23 días del mes de febrero del año 2007, se reunió a las 09:00 horas en las instalaciones del Instituto Potosino de Investigación Científica y Tecnológica, A.C., el Jurado integrado por:

Dr. Humberto Terrones Maldonado	**Presidente**	**IPICYT**
Dr. Mauricio Terrones Maldonado	**Secretario**	**IPICYT**
Dr. David J. Smith	**Sinodal externo**	**ASU**
Dr. Emilio Muñoz Sandoval	**Sinodal**	**IPICYT**
Dr. Florentino López Urías	**Sinodal**	**IPICYT**

a fin de efectuar el examen, que para obtener el Grado de:

DOCTOR EN CIENCIAS APLICADAS
EN LA OPCIÓN DE NANOCIENCIAS Y NANOTECNOLOGÍA

sustentó el C.

Julio Alejandro Rodríguez Manzo

sobre la Tesis intitulada:

Magnetism of carbon nanostructures and in situ TEM dynamic transformations of carbon-based nanomaterials

que se desarrolló bajo la dirección de

Dr. Florentino López Urías
Dr. Humberto Terrones Maldonado
Dr. Mauricio Terrones Maldonado

El Jurado, después de deliberar, determinó

APROBARLO

Dándose por terminado el acto a las 11:15 horas, procediendo a la firma del Acta los integrantes del Jurado. Dando fé el Secretario Académico del Instituto.

A petición del interesado y para los fines que al mismo convengan, se extiende el presente documento en la ciudad de San Luis Potosí, S.L.P., México, a los 23 días del mes febrero de 2007.

Dr. Marcial Bonilla Marín
Secretario Académico

L.C.C. Ivonne Lizette Cuevas Velez
Jefa del Departamento de Asuntos Escolares

INSTITUTO POTOSINO
DE INVESTIGACIÓN
CIENTÍFICA Y TECNOLÓGICA, A.C.
IPICYT
SECRETARIA ACADEMICA

Acknowledgments

Anybody who knows about the subject will say that searching for a good advisor is a difficult task. Finding two, in quantum mechanics terms, is highly improbable. If both are brothers, good luck must be involved. During these years, Humberto and Mauricio Terrones have been excellent advisors. Always available in their office, they transmitted their joy for science and research and made me feel part of the scientific community dedicated to the study of carbon nanostructures that goes back to Alan Mackay and Harry Kroto, among others, and continues with them. My gratitude to both.

The advice given by Florentino López was fundamental for obtaining results on the magnetic properties of carbon nanostructures. I thank him for his willingness to share his programming knowledge, as well as his availability to work as a team. In addition, I thank him and Emilio Muñoz for their generosity: they shared their office with me during the 99% of my stay at IPICYT.

The time at IPICYT would have been less fortunate without the support, the share frustration and the enthusiasm of my fellow travelers: Ana Laura Elías and Adalberto Zamudio, to whom I am grateful. Also, I wish to acknowledge José Romo, for being there to hear and talk about ideas related to carbon nanostructures, among other subjects; Eduardo Cruz, for his help with anything related to my computer's software; David Meneses, who helped me in the analysis of X ray data, and saved me from a row in Guanajuato; and Xavier Lepró, who at the end of this stage helped me with everything about Latex.

One of the most pleasing aspects of carrying out scientific research is the possibility to meet people in different places who are more than happy to share their expertise and knowledge. I thank David Smith, Martha McCartney and Lin Gu from Arizona State University, for being there to teach me the different techniques that can be used in the transmission electron microscope (TEM). It was during the

Contents

List of Tables

List of Figures

Resumen

Durante las últimas dos décadas se ha logrado sintetizar materiales de carbono con distintas formas estructurales y dimensiones en el orden de nanómetros, siendo los fullerenos y los nanotubos de carbono (NTC) dos ejemplos sobresalientes. El hecho de que las propiedades físicas y químicas de los nanomateriales difieren de las propiedades mostradas por átomos individuales, moléculas o materiales en bulto, sirve como motivación para continuar investigando las nanoestructuras de carbono.

En este trabajo se presentan resultados teóricos concernientes a fenómenos magnéticos en nanoestructuras de carbono, así como resultados experimentales sobre la síntesis de diversos NTC y las modificaciones que éstos experimentan cuando son irradiados con electrones.

En particular, se analizan las propiedades magnéticas de fullerenos (C_{60} y C_{70}) fusionados en cadenas lineales y toroides formados por átomos de carbono, cuando se les aplica un campo magnético externo, utilizando para ello la teoría de London. Las estructuras analizadas tienen enlaces tipo sp^2, y además de anillos de carbono de seis lados muestran polígonos de cinco, siete u ocho lados en la red atómica, lo que produce *curvatura* en las estructuras. A diferencia de estructuras planas de carbono como el grafito y las moléculas aromáticas que son diamagnéticas, algunas de las estructuras analizadas presentan paramagnetismo, con valores de hasta 200 CGS ppm por mol de C en la susceptibilidad magnética.

En el terreno experimental, se presentan resultados que muestran la versatilidad del método de *pirólisis de soluciones atomizadas* para sintetizar nanotubos de carbono de varios tipos, como nanotubos de carbono de una sola capa, nanotubos de carbono de varias capas (NTVC) y nanotubos de carbono dopados con nitrógeno. Durante la síntesis de NTVC un pequeño porcentaje del metal catalizador es encapsulado dentro de la región hueca de los NTVC. Utilizando diferentes catalizadores se logró encapsular Fe, Co, Ni y una aleación de FeCo.

Finalmente, se muestran las modificaciones estructurales que experimentan los NTVC que contienen metales encapsulados cuando son irradiados con electrones a 600°C. Esto se logró utilizando un microscopio de transmisión de electrones como equipo de observación y fuente de irradiación, simultáneamente. Los resultados incluyen la posibilidad de utilizar a los NTVC como celdas de alta presión (~ 40 GPa), observaciones *in situ* del crecimiento de NTC desde partículas metálicas y la formación de uniones tipo NTVC-metal-NTVC.

Abstract

Over the last two decades carbon-based materials exhibiting lengths at the nano-scale and different structural forms have been synthesized; fullerenes and carbon nanotubes (CNTs) being two prominent examples. Further research on carbon nanostructures is motivated by the fact that the physical and chemical properties of nanomaterials differ from the properties of individual atoms, molecules or bulk compounds.

This work presents theoretical results on the magnetic response of carbon nanostructures, as well as experimental results on the synthesis of different types of CNTs and the modifications that these materials undergo when irradiated with fast electrons.

The magnetic properties of fullerenes (C_{60} and C_{70}) coalesced into linear chains and toroidal geometries, that are exposed to an external magnetic field, were studied with the London theory. The analyzed structures have covalent sp^2-like bonding and in addition to six-membered carbon rings, contain 5-, 7- or 8-membered rings within the atomic lattice, inducing *curvature*. Contrary to planar carbon structures such as graphite and aromatic molecules that are diamagnetic, some of the analyzed structures were found to exhibit paramagnetism, with magnetic susceptibility values up to 200 CGS ppm per mol of C.

In the experimental sections, results are shown that demonstrate the versatility of the *pyrolysis of aerosolized solutions* method to synthesize different types of carbon nanotubes, such as single-walled carbon nanotubes (SWNTs), multi-walled carbon nanotubes (MWNTs) and nitrogen-doped carbon nanotubes (CN_x). During the synthesis of MWNTs, a small percentage of the catalyst is encapsulated in the hollow core of MWNTs. Encapsulation of Fe, Co, Ni and a FeCo alloy inside MWNTs was achieved by utilizing different catalyst precursors.

Finally, structural modifications of MWNTs, containing metal particles in their

cores, are observed when irradiated with electrons at 600°C. This was accomplished by using a high resolution transmission electron microscope, both as the observation equipment and as the electron irradiation source. Results include the fact that MWNTs behave as high pressure cells ($\sim$ 40 GPa), *in situ* observation of nanotube growth from encapsulated metal particles and formation of MWNT-metal-MWNT junctions.

Preface

The work presented in this thesis was inspired by previous work and, in some parts, carried out in collaboration with others. Of course, mistakes or misinterpretations are my sole responsibility.

Chapter 2, deals with the magnetic response of carbon nanostructures that contain polygons other than hexagons, and is mostly based on three papers, that we published in *Nano Letters*, *Small* and the *Journal of Computational and Theoretical Nanoscience**. The idea to explore this subject was proposed to me by my supervisors Humberto and Mauricio Terrones and Florentino López-Urías as a research subject. The structures analyzed are based on the previous work of Humberto and Mauricio Terrones on curved carbon nanostructures. The program developed to calculate the magnetic properties was built upon an early version made by Florentino López-Urías.

The samples analyzed in chapter 3 were synthesized by myself with the exception of single-walled nanotubes (SWNTs) and multi-walled nanotubes (MWNTs) containing an encapsulated FeCo alloy. The SWNTs were produced at both the IPICYT and Max-Planck-Institut für Metallforschung laboratories, in collaboration with Ana Laura Elías, Adalberto Zamudio and Fabio Lupo. I also collaborated with Ana Laura Elías and Adalbeto Zamudio in the synthesis of the FeCo alloy sample. The characterization of these samples was greatly enhanced thanks to the facilities

---

***Induced ring currents in polymerized C_{60} and C_{70} molecules**. F. López-Urías, J. A. Rodríguez-Manzo, M. Terrones, and H. Terrones. *Journal of Computational and Theoretical Nanoscience* , 4:252-256 (2007). **Anomalous paramagnetism in doped carbon nanostructures**. J. A. Rodríguez-Manzo, F. López-Urías, M. Terrones, and H. Terrones. *Small*, 3:120-125 (2007). **Magnetism in corrugated carbon nanotori: the importance of symmetry, defects, and negative curvature**. J. A. Rodríguez-Manzo, F. López-Urías, M. Terrones, and H. Terrones. *Nano Letters*, 11:2179-2183 (2004).

and expertise provided by David Smith, Martha McCartney and Lin Gu at Arizona State University; Manfred Rühle and Fabio Lupo at the Max-Planck-Institut für Metallforschung; Morinobu Endo, M. Muramatsu, T. Hayashi and Y. A. Kim at Shinshu University; and Dimitri Golberg, Y. Bando and C. C. Tang at the NIMS institute in Tsukuba. These collaborations resulted in two publications[†].

Chapter 4 is heavily influenced by Florian Banhart's previous work on the electron irradiation of carbon nanostructures inside the Transmission Electron Microscope (TEM). The idea to do this type of experiment with MWNTs containing encapsulated metals was discussed with Mauricio and Humberto Terrones together with Florian Banhart. The experiments shown in this chapter were done at the University of Mainz facilities. Part of this chapter is based on a Science paper, where I participated in the samples synthesis and characterization, and the TEM experimental observations together with Litao Sun[‡]. The theoretical calculation of this particular section was performed by Arkady Krasheninnikov. The *in situ* carbon nanotube growth observations resulted in a paper, already accepted for publication in *Nature Nanotechnology*[§].

A complete list of the published articles during my research investigation at IPICYT is given at the end of this thesis.

[†]**Pyrolytic synthesis of long strands of large diameter single-walled carbon nanotubes at atmospheric pressure in the absence of sulphur and hydrogen**. F. Lupo, J. A. Rodríguez-Manzo, A. Zamudio, A. L. Elías, Y. A. Kim, T. Hayashi. M. Muramatsu, R. Kamalakaran, H. Terrones, M. Endo, M. Rühle, and M. Terrones. *Chemical Physics Letters*, 410:384-390 (2005). **Production and characterization of single-crystal FeCo nanowires inside carbon nanotubes**. A. L. Elías, J. A. Rodríguez-Manzo, M.R. McCartney, D. Goldberg, A. Zamudio, S. E. Baltazar, F. López-Urías, E. Muñoz-Sandoval, L. Gu, C. C. Tang, D. J. Smith, Y. Bando, H. Terrones, and M. Terrones. *Nano Letters*, 3:467-472 (2005).

[‡]**Carbon nanotubes as high-pressure cylinders and nanoextruders**. L. Sun, F. Banhart, A. V. Krasheninnikov, J. A. Rodríguez-Manzo, M. Terrones, and P. M. Ajayan. *Science*, 312:1199-1202 (2006).

[§]**In-situ nucleation of carbon nanotubes by the injection of carbon atoms into metal particles**. J. A. Rodríguez-Manzo, M. Terrones, H. Terrones, H. W. Kroto, L. Sun and F. Banhart. Accepted for publication in *Nature Nanotechnology* (2007).

Chapter 1

General introduction

1.1 Carbon nanostructures and related materials

Carbon, the sixth element of the periodic table, can be found in a great variety of structural forms either in nature or in synthetically produced materials. These carbon materials cover a wide range of properties and their dimensionality varies from 0D molecules to 3D crystals. This versatility is inherited by the ability of carbon to combine with itself or other atoms via three available types of valence bonds. Physicists refer to chemical bonds as the hybridization of atomic orbitals, and the three forms of hybridization present in carbon compounds are: sp, sp^2 $(sp^{2+\epsilon})$ and sp^3. Solid carbon structures such as diamond and graphite correspond to 3D materials and a single layer of graphite (graphene sheet) to a 2D material [1]. In addition, carbon nanotubes are considered as 1D structures [2], and the family of fullerenes as 0D molecules [3]. Over the past 15 years research on carbon-based materials at the nanoscale has been intensively promoted.

This section presents the different types of hybridization that carbon can acquire, describing different carbon allotropes such as diamond, graphite, graphene, carbon nanotubes (CNTs) and fullerenes. The emphasis is placed on nanostructures possessing sp^2 hybridized bonding.
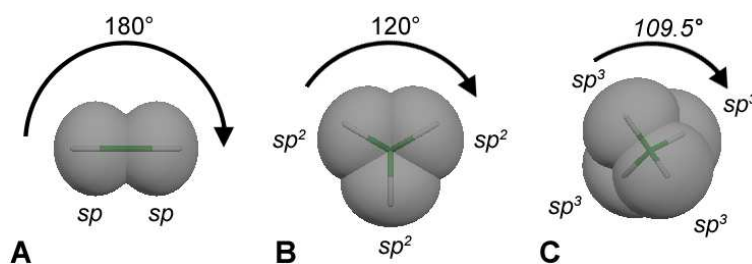
Figure 1.1: (Color) Different sp^n hybridizations in carbon: (**A**) sp, (**B**) sp^2, and (**C**) sp^3.

1.1.1 sp^n hybridizations in carbon

The electronic ground state configuration of the carbon atom corresponds to $1s^2 2s^2 2p^2$. Two of the six electrons occupy the $1s$ orbital and are strongly bound. The remaining four (valence electrons) occupy the next energetic orbitals ($2s^2 2p^2$) and are weakly bound. The mixing of a single $2s$ electron with $2p$ electrons is called sp^n hybridization ($n = 1, 2, 3$) [4]. Figure 1.1 shows the different sp^n hybridization states in carbon.

The linear combination ($\pm$) of the $2s$ orbital with one of the $2p$ orbitals (e.g., $2p_x$) forms two sp hybridized orbitals, with an angle of $180°$ between them (Fig. 1.1A). By overlapping these hybridized orbitals with sp orbitals from neighboring atoms, covalent σ bonds are formed. The remaining two p orbitals, which are perpendicular to the σ bonds, generally form π bonds, as in the acetylene (HC≡CH) molecule. The linear combination of the $2s$ orbital with two p orbitals (e.g., p_x and p_y) forms a sp^2 hybridized orbital. The three equivalent sp^2 orbitals form a structure with three-fold symmetry (Fig. 1.1B). The remaining p orbital, perpendicular to the plane defined by the sp^2 orbitals, forms π bonds by overlapping with p orbitals of neighboring carbon atoms. The planarity that the sp^2 hybridization imposes is common in carbon compounds that have hexagonal rings (e.g., aromatic compounds and graphite). However, the planarity can be disrupted, either by bending the structure or incorporating polygons other than hexagons in the structure. In such cases, the angles between the hybridized orbitals change, and the hybridization is somehow intermediate between a sp^2 and a sp^3 state, known as $sp^{2+\epsilon}$ hybridization [5]. For simplicity, when analyzing curved carbon nanostructures whose atoms have three

nearest neighbors, we will refer to them as sp^2 bonded structures, but it should be considered that $sp^{2+\epsilon}$ hybridization is present. When the three p orbitals combine with the $2s$ orbital, sp^3 hybridization occurs (Fig. 1.1C). In this tetragonal configuration, the four equivalent sp^3 orbitals have the maximum spatial separation from each other, and the central carbon atom can form σ bonds with four neighbors, as in diamond.

1.1.2 Carbon allotropes

Figure 1.2 shows representative structural forms of carbon compounds with different dimensionality. With the exception of diamond, the rest of the carbon allotropes possess sp^2 hybridized bonds. This type of hybridization, which permits the bending of planar layers of carbon or the introduction of polygons other than hexagons to the honeycomb lattice, can form carbon nanostructures exhibiting fas-
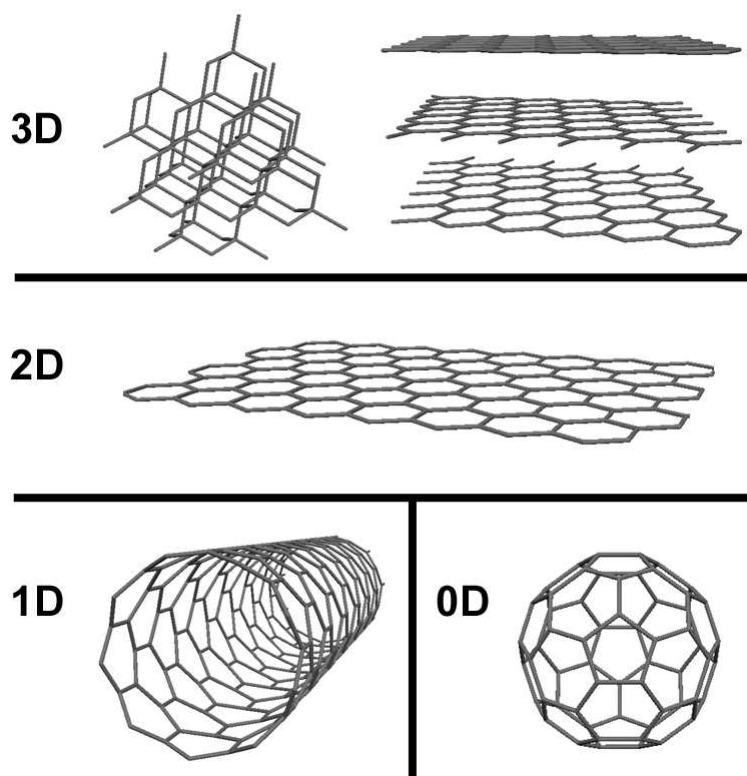
Figure 1.2: Different structural forms of all-carbon-based materials, with different dimensionality. (**3D**) Diamond (left) and graphite (right). (**2D**) Graphene sheet. (**1D**) Single-walled carbon nanotube. (**0D**) C_{60} molecule: Buckministerfullerene.

cinating properties.

Diamond is formed by sp^3 hybridized carbon atoms. Each atom forms strong covalent bonds with four neighbors, with a distance of 1.56 Å, thus resulting in a rigid crystal. For diamond, the overall crystal structure is isotropic (lattice constant $a = 3.567$ Å; space group Fd3m); the classical cubic phase is shown in Fig. 1.2(3D, left). Since all the electrons are localized in the bonds within the sp^3 framework, diamond behaves like an insulator, with an electric resistivity of 10^{11} Ωm. The stable thermodynamic phase of carbon under ambient conditions is graphite (Fig. 1.2(3D, right)). This 3D carbon crystal is composed of an arrangement of stacked layers, that interact through *van der Waals* forces between them and have sp^2 bonding within them. The stacking repeats every two layers (ABAB...) in the hexagonal phase or every three layers (ABCABC...) in the rhombohedral phase. The distance between layers is 3.35 Å, and the sp^2-bonded atoms within the layers form a honeycomb lattice, with a C–C bond length of 1.42 Å. This geometry gives rise to an anisotropic crystal structure ($a = 2.456$ Å, $c = 6.696$ Å, and $\gamma = 120°$; space group P6$_3$/mmc). Contrary to diamond, graphite does conduct electric current and is considered a semi-metal. This is because the electrons in the p orbitals that did not hybridize in sp^2 form, and are responsible for van der Waals interactions, can move within the electronic cloud, thus producing a current. A single layer of graphite is known as a graphene sheet (Fig. 1.2(2D)) and can be produced by micro-mechanical cleavage of graphite [1]. These free-standing atomic crystals are strictly 2D, and do not lose the sp^2 character of the honeycomb lattice. However, the change in dimensionality alters properties such as surface/volume ratio and the density of electronic states.

Although the surface of CNTs are formed by the same honeycomb lattice structure of graphene with sp^2 bonding, because of their tubular structure, with a high length/width aspect ratio and their physical properties, they are more a 1D rather than a 2D physical system. A single-walled carbon nanotube (SWNT) [6, 7] has one atom in wall thickness, is typically microns in length and has a diameter of less than 2 nm (Fig. 1.2(1D)). A group of concentric SWNTs forms a multi-walled carbon nanotube (MWNT). In order to classify SWNTs, it helps to think of them as rolled graphene sheets. A notation was developed where each individual tube is mapped
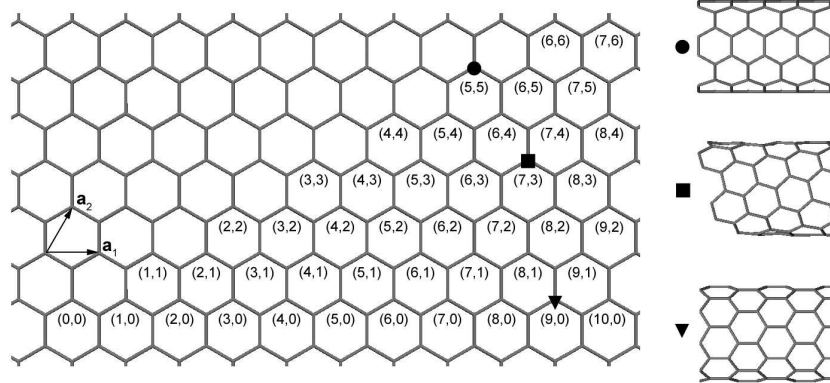
Figure 1.3: Graphene sheet with atoms labeled using the (n, m) notation. The unit vectors $\mathbf{a}_1$ and $\mathbf{a}_2$ of the 2D lattice are shown. Three representative tubes: (•) armchair $(5, 5)$ SWNT; (■) chiral tube, $(7, 3)$ SWNT and (▼) zig-zag $(9, 0)$ SWNT.

to a vector $\mathbf{C}$ [4]. This vector is expressed as

$$\mathbf{C} = n\mathbf{a}_1 + m\mathbf{a}_2,$$

where $\mathbf{a}_1$ and $\mathbf{a}_2$ are the unit cell base vectors of the graphene sheet, and $n \geq m$. Then, each possible single tube is produced by rolling up the graphene sheet so that the two-end points of the $\mathbf{C}$ vector are superimposed. Because of symmetry considerations, only one twelfth of the complete graphene sheet is necessary to classify all SWNTs. Figure 1.3 shows how SWNTs are mapped into the graphene sheet. Atomic positions are labeled by an (n, m) index in the honeycomb lattice, and a (n, m) SWNT is formed by superimposing the atom $(0, 0)$ with the atom (n, m). SWNTs with indexes (n, n) and $(n, 0)$ are highly symmetric, and are known as *armchair* and *zig-zag* tubes, respectively. For the rest of the tubes, the hexagons are arranged helically around the tube axis, thus producing "handedness". These tubes can be distinguished from its mirror image, and are known as chiral SWNTs.

CNTs properties are both scientifically and technologically attractive. Covalent bonding in CNTs, coupled with their cylindrical structure, makes them very stiff. Young's modulus values of ~ 1 TPa, have been measured for both individual MWNTs and ropes of SWNTs [8, 9]. These exceptional mechanical properties combined with the low density of carbon compounds implies that nanotubes are useful as nanoscale fibers in robust, lightweight composite materials. Com-

posite fibers containing 60% SWNTs by weight have reached tensile strengths of 1.8 GPa, which matches that of spider silk [10]. Phonons also propagate easily on nanotubes. For single MWNTs, thermal conductivities over 3000 W/mK have been measured [11], which are greater than that of natural diamond. But even greater values ($\sim$ 6600W/mk) have been theoretically estimated for SWNTs [12]. The specific form in which carbon atoms arrange to form a SWNT has a profound effect on the electronic properties of the system. Depending on their chirality, SWNTs can be either metallic or semiconducting [4]; a remarkable property for all-carbon sp^2 systems.

The discovery of C_{60} in 1985 [3] gave a great impulse to carbon nanostructure research. Carbon 60 (C_{60}, Buckminsterfullerene), is a cage molecule with 60 carbon atoms arranged in an sp^2 fashion, resembling a soccer ball, with 12 pentagons and 20 hexagons (Fig. 1.2(0D)). Besides C_{60}, other molecular forms of carbon that possess the sp^2 bonded cage-like structure of C_{60} can be formed. These include C_{70}, C_{76}, C_{80}, C_{84}, ..., (also known as fullerenes). In fact, capped SWNTs can be considered of as elongated fullerenes [13].

Carbon nanostructures are usually produced with physical rather than chemical methods. These processes involve the condensation of carbon atoms, generated from the evaporation of carbon targets with laser ablation or arc-discharge techniques, in the temperature range of 3000–4000°C or by the decomposition of gaseous carbon (e.g., CH_4) over catalytic particles, from where carbon nanostructures grow, in relatively lower temperatures regimes ($\sim$ 1000°C).

1.2   The concept of curvature

A concept borrowed from differential geometry, which has proved to be quite useful in order to classify carbon nanostructures that contain carbon rings other than hexagons in the atomic lattice, is *curvature* [14]. Intuitively, curvature is the amount by which a geometric object deviates from flatness. Mathematically, the curvature of a point in a curve is defined as the inverse of the radius of a circle which best fits the curve at that point. Thus, the curvature of a line is zero for all
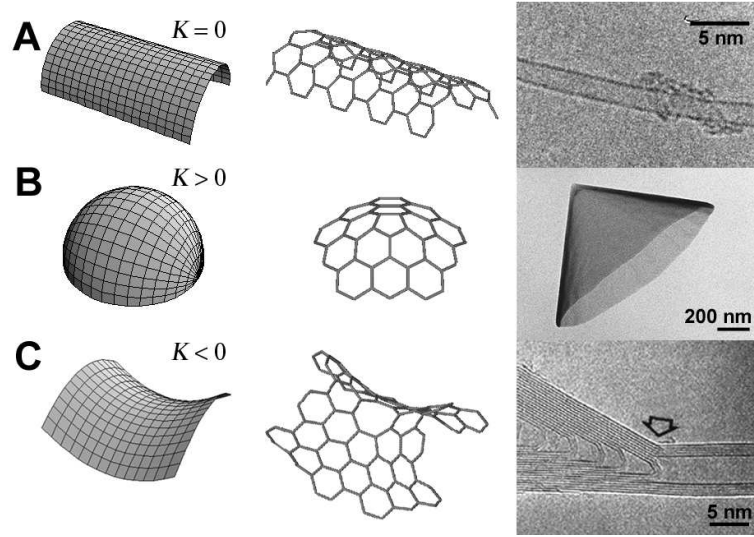
Figure 1.4: Surfaces (left), carbon lattices (middle) and carbon nanostructures (right) with different Gaussian curvature. (**A**) Cylindrical surface with $K = 0$, model of a segment of a SWNT and a SWNT image. (**B**) Convex surface with $K > 0$, carbon cone model with a pentagonal and graphitic cone image [15]. (**C**) Surface with a saddle point ($K < 0$), segment of carbon tetra-pod with a octagonal ring [16] and MWNT image showing a saddle point (arrow) [17].

points and the curvature of a circle of radius r is $1/r$. For a surface the curvature at a point is defined by fitting two circles, with their planes including the normal to the surface and located at right angles to each other. If both curvatures are either maxima or minima, then they are known as principal curvatures k_1 and k_2. The Gaussian curvature K of a surface is defined as the product of the two principal curvatures, $K = k_1 k_2$. For a convex surface $k_1, k_2 > 0$, and for a saddle point k_1 and k_2 have different signs; the Gaussian curvature for a convex surface is positive and that of a saddle point is negative. For cylindrical surfaces $K = 0$, since one of the principal curvatures k is zero. Surfaces with different Gaussian curvature are shown in Fig. 1.4, together with atomic lattice models and electron microscopy images of curved carbon nanostructures.

The honeycomb lattice of graphene has zero Gaussian curvature and could be bent to form a cylinder ($K = 0$), preserving the hexagonal array, as in SWNTs. In reality, SWNTs are not formed in this way, but their existence proves that sp^2 carbon networks are not confined to planar geometries. The sole introduction of a pentagonal ring in graphene causes the modification of the entire sheet, forming a

cone, where the pentagon is the apex (Fig. 1.4B); such graphitic cones have been synthesized [15]. For C_{60}, 12 five-membered rings are necessary among the hexagons to permit topological closure. The introduction of polygons with more than six sides, induces saddle-shaped regions in a graphene layer (Fig. 1.4C). This type of morphology has also been observed experimentally [17], and it was theoretically predicted that such patches could be joined to form periodical minimal surfaces of sp^2 bonded carbon atoms [18].

Thus, in sp^2 hybridized atomic networks (not necessarily of carbon) the introduction of rings exhibiting less than six sides generates positive Gaussian curvature and the introduction of rings with $n > 6$ sides induces negative Gaussian curvature. For graphitic structures, these local modifications do not change the sp^2 bonding characteristic. It is interesting to notice that the introduction of such polygons in the lattice may alter the physical properties of carbon nanostructures.

Convex or cylindrical carbon lattices can serve as vessels able to host foreign materials. Soon after the discovery of C_{60} lanthanum atoms were introduced into its hollow core [19], and soon after the discovery of CNTs it was shown that lead could fill their cores [20]. After this pioneering work, over half of the elements in the periodic table were succesfully introduced into the hollow cores of such cylindrical structures [21, 22].

1.3   Magnetism of *curved* carbon nanostructures

As mentioned above, the introduction of curvature in carbon sp^2 networks may alter their physical properties. Graphite and planar aromatic molecules are highly diamagnetic, because when exposed to an external magnetic field, induced ring currents flow through the hexagonal rings within the structures. Thus, it came as a surprise to find out that C_{60}, which contains 20 hexagons [3], is mildly diamagnetic at room temperature and even becomes paramagnetic at low temperatures [23, 24]. It appears that this effect is influenced by the existence of 12 pentagons in the C_{60} structure. In this context, it becomes important to study the effects of an external magnetic field on nanostructures containing polygons other then hexagons.

1.4   Electron irradiation of carbon nanostructures

Not only new structural forms of carbon have been synthesized recently at the nano-scale, but also the structural modifications that these new materials undergo when exposed to electron irradiation have furnished surprising results. Electron irradiation experiments carried out inside the Transmission Electron Microscope (TEM) allow *in situ* observations of dynamic transformations of carbon nanostructures. For example, carbon *onions* have been produced with this technique by irradiating polyhedral carbon particles [25]. Moreover, modifications like the cutting of CNTs [26] or transformation of a SWNT bundle into a MWNT [27], could be considered as a type of nano-engineering, as Florian Banhart has proposed [27].

1.5   Organization of the thesis

The work presented in this thesis describes three lines of research reflected in three core chapters (2, 3 and 4), carbon nanostructures being the common link to all. The chapters are almost self-contained, so if the reader pleases he/she could read them independently. However, the samples analyzed in chapter 4 were synthesized and characterized with the techniques discussed in chapter 3.

In chapter 2 the response of π-electrons in sp^2 bonded carbon nanostructures under the influence of a magnetic field is studied in the framework of the London theory, which allows the estimation of magnetic susceptibilities and induced inter-atomic ring currents. Carbon nanostructures examined include coalesced fullerenes (C_{60} and C_{70}) and carbon nanotori. These molecular models possess polygons other than hexagons in the atomic lattice, which induce curvature in the structures. Results shown reveal that contrary to planar sp^2 bonded carbon structures, like graphite and aromatic molecules, curved carbon complexes could be paramagnetic. In particular, depending on the geometry of coalescence, some polymerized fullerenes could have ring current magnetic susceptibilities up to ~ 200 CGS p.p.m per mol C, which is twice the total magnetic susceptibility of graphite and of opposite sign. In addition, it is found that paramagnetic moments could be induced in carbon nanotori. To

elucidate these effects, a thorough analysis of the induced inter-atomic ring currents in curved carbon nanostructures is provided.

The synthesis and characterization of SWNTs, MWNTs and nitrogen-doped MWNTs is discussed in chapter 3. The pyrolysis of aerosolized solutions, the method used to synthesize the different types of CNTs, is explained in the first part of the chapter. Briefly, in this method, a compound containing the catalyst necessary for CNT growth is dissolved in a solvent which is the carbon source. Then, the solution is aerosolized and carried to a furnace, where CNT growth takes place. By changing the solvent, different types of CNTs could be grown. Results show that SWNTs grow with ethanol, MWNTs with ethanol or toluene, and nitrogen-doped MWNTs with benzylamine. As a side effect, MWNTs grown with the pyrolysis of aerosolized solutions, a small amount of catalyst particles are found encapsulated within the MWNTs. In this context, the encapsulation of Fe, Co, Ni, and a FeCo alloy is analyzed.

In chapter 4 the response of MWNT-based nanostructures under electron irradiation is investigated. Moreover, the effects are monitored *in situ*. This is achieved by using the beam of a transmission electron microscope as the electron irradiation source during microscopy observations. A brief review of the electron irradiation effects on carbon nanostructures is presented. In particular, the effect of heating ($\sim 600°C$) carbon nanostructures to anneal defects produced by displacement of atoms is discussed. Results presented in this chapter include the possible use of MWNTs as high pressure cells, *in situ* observations of CNT growth and the formation of MWNT-metal-MWNT junctions.

Finally, general conclusions about this thesis are presented as well as possible lines of research that could be interesting to pursues, derived from this work.

References

[1] K.S. Novoselov, D. Jiang, F. Schedin, T. J. Booth, V. V. Khotkevich, S. V. Morozov, and A. K. Geim. Two-dimensional atomic crystals. *PNAS*, 30:10451–10453, 2005.

[2] S. Iijima. Helical microtubules of graphitic carbon. *Nature*, 254:56–58, 1991.

[3] H. W. Kroto, J. R. Heath, S. C. O'Brien, R. F. Curl, and R. E. Smalley. C_{60}: Buckminsterfullerene. *Nature*, 318:162–163, 1985.

[4] R. Saito, G. Dresselhaus, and M. S. Dresselhaus. *Physical properties of carbon nanotubes*, chapter 1. Imperial College Press, 2003.

[5] H. Okuno. *Synthesis and characterization of carbon-based materials*. PhD thesis, Université catholique de Louvain, 2006.

[6] S. Iijima and T. Ichihashi. Single-shell carbon nanotubes of 1-nm diameter. *Nature*, 363:603–605, 1993.

[7] D. S. Bethune, C. H. Klang, M. S. de Vries, R. Gorman, G.and Savoy, J. Vazquez, and R. Beyers. Cobalt-catalysed growth of carbon nanotubes with single-atomic-layer walls. *Nature*, 363:605–607, 1993.

[8] M. M. J. Treacy, T. W. Ebbesen, and J. M. Gibson. Exceptionally high young's modulus observed for individual carbon nanotubes. *Nature*, 381:678–680, 1996.

[9] M.-F. Yu, B.S. Files, S. Arepalli, and R. S. Ruoff. Tensile loading of ropes of single wall carbon nanotubes and their mechanical properties. *Phys. Rev. Lett.*, 84:5552–5555, 2000.

[10] A. B. Dalton, S. Collins, E. Muñoz, V. H. Razal, J. M.and Ebron, J. P. Ferraris, J. N. Coleman, B. G. Kim, and R. H. Baughman. Super-tough carbon-nanotube fibres. *Nature*, 423:703, 2003.

[11] P. Kim, L. Shi, A. Majumdar, and P. L. McEuen. Thermal transport measurements of individual mutiwalled nanotubes. *Phys. Rev. Lett.*, 87:215502, 2001.

[12] S. Berber, Y. K. Kwon, and D. Tomanek. Unusually high thermal conductivity of carbon nanotubes. *Phys. Rev. Lett.*, 84:4613–4616, 2000.

[13] D. T. Colbert and R. E. Smalley. Past, present and future of fullerene nanotubes: buckytubes. In E. Osawa, editor, *Perspectives of fullerene nanotechnology*, pages 3–10. Kluwer Academic Publishers, 2002.

[14] A. L. Mackay and H. Terrones. Diamond from graphite. *Nature*, 352:762, 1991.

[15] A. Krishnan, E. Dujardin, M. M. J. Treacy, J. Hugdahl, S. Lynum, and T. W. Ebbesen. Graphitic cones and the nucleation of curved carbon surfaces. *Nature*, 388:451–454, 1997.

[16] J. M. Romo-Herrera, M. Terrones, H. Terrones, S. Dag, and V. Meunier. Covalent 2D and 3D networks from 1D nanostructures: designing new materials. *Nano Lett.*, 7:570–576, 2007.

[17] S. Iijima, T. Ichihashi, and Y. Ando. Pentagons, heptagons and negative curvature in graphite microtubule growth. *Nature*, 356:776–778, 1992.

[18] H. Terrones and A. L. Mackay. The geometry of hypothetical curved graphite structures. *Carbon*, 30:1251–1260, 1992.

[19] J. R. Heath, S. C. O'Brien, Q. Zhang, Y. Liu, R. F. Curl, F. K. Tittel, and R. E. Smalley. Lanthanum complexes of spheroidal carbon shells. *JACS*, 107:7779–7780, 1985.

[20] P. M. Ajayan and S. Iijima. Capillarity-induced filling of carbon nanotubes. *Nature*, 361:333–334, 1993.

[21] http://homepage.mac.com/jschrier/endofullerenes_table.html.

[22] C. Guerret-Piécourt, Y. Le Bouar, A. Lolseau, and H. Pascard. Relation between metal electronic structure and morphology of metal compounds inside carbon nanotubes. *Nature*, 372:761–765, 1994.

[23] M. S. Dresselhaus, G. Dresselhaus, and P. C. Eklund. *Science of fullerenes and carbon nanotubes: their properties and applications*, chapter 18. Academic Press, 1996.

[24] R. C. Haddon. Magnetism of the carbon allotropes. *Nature*, 378:249–255, 1995.

[25] D. Ugarte. Curling and closure of graphitic networks under electron-beam irradiation. *Nature*, 359:707–709, 1992.

[26] F. Banhart, J. Li, and M. Terrones. Cutting single-walled carbon nanotubes with an electron beam: evidence of atom migration inside nanotubes. *Small*, 1:953–956, 2005.

[27] J. Li and F. Banhart. The engineering of hot carbon nanotubes with a focused electron beam. *Nano Lett.*, 4:1143–1146, 2004.

Chapter 2

Magnetic response of π-electrons in carbon nanostructures

2.1 Introduction

In this chapter, a theoretical study of the magnetic response of π-electrons in sp^2 bonded carbon nanostructures is presented. The magnetic response of some compounds of carbon such as graphite, aromatic molecules and C_{60} is reviewed and in this context the concept of *ring currents* is introduced. The theoretical background (London theory) used to calculate the electronic energies, ring currents and magnetic susceptibilities of sp^2 carbon systems subjected to an external magnetic field is presented.

Geometries of carbon nanostructures containing polygons other than hexagons, such as coalesced C_{60} molecules and carbon nanotori, are shown. These types of structures possess local negative or positive Gaussian curvature. From the study of the magnetic susceptibilities, induced magnetic moments and ring currents, it is found that some of these carbon nanostructures could exhibit a paramagnetic response, contrary to graphite and planar aromatic molecules, which are diamagnetic. Finally, the effect of adding electrons or holes to these systems is analyzed in the context of doped carbon nanostructures.

2.2   Magnetism of carbon allotropes

Diamond and graphite have different physical properties because of their distinct nature of bonding among atoms (see Fig. 1.2). When a magnetic field is applied to diamond (an insulator with an electric resistivity of 10^{11} Ωm), there is not a magnetic response due to the lack of free electrons. For graphite, a semi-metal (3.5×10^{-5} Ωm), it is assumed that the π-electrons (within the p_z orbitals) are free to circulate along the hexagonal rings, thus inducing a magnetic field that opposes the external one. This explanation, given by Raman in 1929 [1], introduced the concept of molecular *ring currents* and still remains as the basis for our understanding of the significant difference between the magnetic susceptibility of diamond (-5.0×10^{-7} emu/g) and that of graphite (-8.1×10^{-6} emu/g)*, where the magnetic susceptibility χ measures the response of the magnetization $\mathbf{M}$ to the applied magnetic field $\mathbf{H}$, through $\mathbf{M} = \chi \mathbf{H}$. The sign of χ differentiates diamagnetic (negative) from paramagnetic (positive) materials. Thus, both diamond and graphite are diamagnetic. For diamond, the overall crystal structure is isotropic whereas for graphite it is anisotropic, and this structural distinction is reflected in their respective χ. Diamond's χ is isotropic, but for graphite the χ is larger for a field parallel to the c axis than for an applied field perpendicular to the c axis. By applying the concept of ring currents to a set of aromatic molecules like benzene (C_6H_6), naphthalene ($C_{10}H_8$), anthracene ($C_{14}H_{10}$), etc., Linus Pauling [3] explained the observed diamagnetic anisotropy. These organic molecules, being planar assemblages of hexagonal carbon rings saturated with hydrogen atoms, allow the circulation of ring currents along the bond paths when a magnetic field is applied normal to the rings, but produce no ring currents when the field is parallel to the rings. Figure 2.1 shows the assumed path of induced currents in anthracene as first derived by Pauling. The anisotropy in χ displayed by these molecules becomes clear if one considers that the induced magnetic moment in a closed loop is equal to the induced current in the loop times

---

*This is an average value from the parallel ($\chi_{||} = -24.0 \times 10^{-6}$ emu/g) and perpendicular ($\chi_{\perp} = -0.2 \times 10^{-6}$ emu/g) magnetic susceptibilities of graphite respect to the c axis [2]. Taking into account the crystal structure of graphite, $\langle \chi \rangle = (\chi_{||} + 2\chi_{\perp})/3$.

**Induced currents
in anthracene**

**Assumed path of
induced currents
in anthracene**
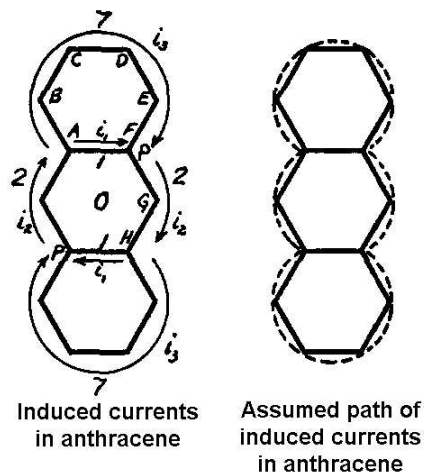
Figure 2.1: The induced current pattern in anthracene as first derived by Linus Pauling for a magnetic field normal to the hexagonal rings [3].

the enclosed area ($\mu = IA$). Then, for fields normal to the carbon rings the χ is larger than for fields parallel to the rings.

The (molar) χ is given by the Larmor-Langevin formula[†]

$$\chi = -\frac{N_A e^2}{6mc^2}\langle r^2 \rangle, \tag{2.1}$$

where N_A is Avogadro's number, c is the speed of light, $\langle r^2 \rangle$ is the mean square of the distance of the electronic circulation, m the electron mass and e the electron charge. This formula considers electronic circulations with spherical symmetry. However, for π-electrons that revolve around in a plane, with one degree of freedom less, the mean electronic circulation is only $r^2 = \langle x^2 + y^2 \rangle$, so the denominator of Eq. (2.1) changes to $4mc^2$. With Eq. (2.1) Kathleen Lonsdale calculated the effective radii for the electronic circulation for carbon compounds with different hybridization and found radius lengths of 0.7 Å (diamond), 0.8 Å (aliphatic), 0.7 Å (aromatic σ-electrons), 1.5–1.6 Å (aromatic π-electrons) and 7.8 Å (graphite π-electrons), where the last value gives an average area equal to that of 30 benzene nuclei [4]. An important point to note is that, as Haddon states: "the magnetic properties provide a length scale for the electronic circulations induced by an applied magnetic field and show that in certain compounds of carbon inter-atomic currents can flow in the same manner as they do in a metal like bismuth" [1].

Nanostructures like fullerenes and carbon nanotubes (CNTs) (Fig. 2.2) that are not confined to planar geometries depart from the classical diamagnetic behavior

---

[†]In CGS units.
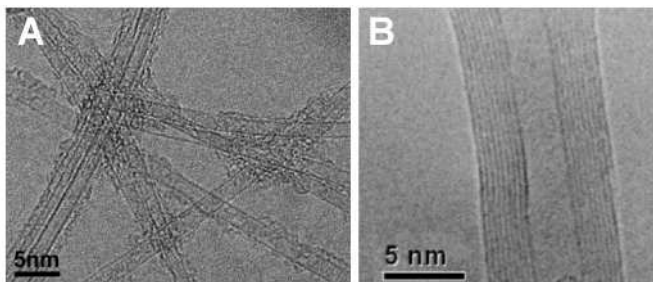
Figure 2.2: Electron microscopy images of (**A**) SWNTs and (**B**) a MWNT.

shown by graphite and aromatic molecules. In the seminal paper where the structure of the C_{60} molecule was first proposed [5], the authors noted that, given the evidence that some foreign atoms could be placed inside the C_{60} cage, "the chemical shift in the NMR of the central atom should be remarkable because of the ring currents [in C_{60}]." In this sentence, essentially, a strong diamagnetic response of Buckminsterfullerene was predicted. However, Haddon *et al.* found out that C_{60} exhibits a smaller χ compared to that of benzene χ_b ($\chi_{C_{60}} \sim 0.2|\chi_b|$) [6, 7]. This surprising result is due to a cancellation effect between paramagnetic and diamagnetic ring currents in the cage [8]. Experimentally, it was demonstrated that the χ of multi-walled carbon nanotubes (MWNTs) is significantly greater than that of highly oriented pyrolitic graphite (HOPG) [9]. Because the measurement was carried out on bundles of MWNTs, anisotropy in the χ was not detected, but the large magnitude of χ suggests that, in at least one of the two principal directions, either parallel or perpendicular to the symmetry axis, χ is larger than in graphite. One possibility is that induced currents may flow around the waist of the tubes. Nevertheless, theoretical calculations have predicted novel magnetic properties for single-walled nanotubes SWNTs (the building blocks of MWNTs), such as magnetic field-induced metal-insulator transitions and χ that can be either diamagnetic or paramagnetic, depending on the chirality of the nanotube and the applied field direction [10].

Pristine fullerite is a van der Waals crystal, and by heating it under high pressure, it can be converted into covalently bonded cages that form crystalline phases. Depending on the experimental parameters the polymerization can occur in one, two or three dimensions [11]. The two-dimensional polymerized phase (Fig. 2.3), known as rhombohedral C_{60} (Rh-C_{60}), resembles HOPG, but the layers consist of covalently bonded C_{60} molecules arranged in a hexagonal pattern. For this phase,
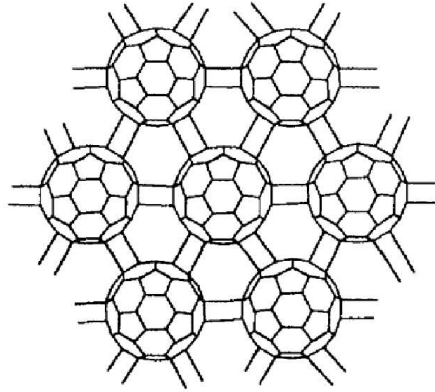
Figure 2.3: Polymerized C_{60} in two dimensions: rhombohedral C_{60}. Adapted from [11].

Makarova *et al.* reported a strong ferromagnetic signal [12]. The authors observed a positive (inductive) χ of Rh-C_{60} and an anisotropic response with ratio $\chi_\perp/\chi_\parallel = 5.5$. The sample also presented a saturation magnetization, large hysteresis loop and attachment to a magnet at room temperature, characteristics that led the authors to conclude that the phase behaves like a ferromagnet with a magnetic moment per electron of 0.4 μ_B, where μ_B is the Bohr magneton[‡].

Recently, the production of a new form of magnetic carbon was reported [13]. The material consists of cluster-assembled carbon nanofoam and is produced by a high-repetition-rate, high-power laser ablation of glassy carbon in Ar atmosphere. The foam contains both sp^2 and sp^3 hybridized carbon atoms, with a higher percentage of the former, and exhibits some remarkable physical properties, including a density of $\sim$ 2–10 mg/cm^3 and a large surface area of 300–400 m^2/g, comparable to that of zeolites. Carbon nanofoam has shown a ferromagnetic-like behavior up to 90 K, a response highly unusual for all-carbon systems [14]. High-resolution transmission electron micrographs of the nanofoam revealed patterns characteristic of hyperbolically curved graphitic sheets. This type of structure branded "Schwarzite" has been predicted theoretically [15] and exhibits negative Gaussian curvature, as opposed to fullerenes and CNTs.

[‡]The paper that contains these findings [12] has been recently retracted (*Nature*, 440:707 (2006)), although not by all the authors.

2.3   Coalescence of C_{60} and carbon nanotori

Molecular models of polymerized C_{60} molecules and carbon nanotori, which preserve the sp^2 graphitic characteristic, are presented. These structures may contain polygons other than hexagons, introducing local positive or negative Gaussian curvature in the structures. Also, some experimental evidence of these types of geometries is discussed.

2.3.1   Coalescence of C_{60}

SWNTs are able to contain C_{60} molecules in their cores [16], and the resulting structures are termed nanopeapods (Fig. 2.4A), for obvious reason. The interaction between the C_{60} molecules and the SWNT that contains them is not covalent. During the first observation of these structures, done in a high resolution transmission electron microscope (HRTEM), it was noticed that under the electron beam coalescence of the endofullerenes occurred [16]. Synthesis of C_{60}@SWNTs in 90% yields has been achieved, thus facilitating both bulk and local property measurements [17]. If nanopeapods are heated to temperatures above 800°C, coalescence of C_{60} molecules also occurs. The coalescence process can be achieved without any interaction of the molecules with the SWNT that encloses the molecules. In a study of Bandow *et al.*, the formation of C_{60} dimers, trimers, tetramers and so on (Fig. 2.4B) was observed as annealing temperature increases [18]. In fact, the authors observed a full transformation from nanopeapods to double-wall nanotubes (DWNTs). Possible mechanisms for the coalescence of C_{60} molecules inside SWNTs triggered by electron irradiation have been proposed [19]. In particular, C_{60} being highly symmetric (icosahedral symmetry) could coalesce in three different ways: along the 2-, 3-, and 5-fold axis of symmetry. Connected fullerenes of these types result in corrugated tubes (Fig. 2.4C). Figure 2.4D shows the theoretical models of these corrugated tubes. Before coalescence, C_{60} contains 12 five-membered carbon rings (5MR) and 20 six-membered rings (6MR). It is important to notice that in the coalesced models seven (7MR) and eight membered rings (8MR) also appear at the junctions, depending on the symmetry of coalescence (Fig. 2.4D).
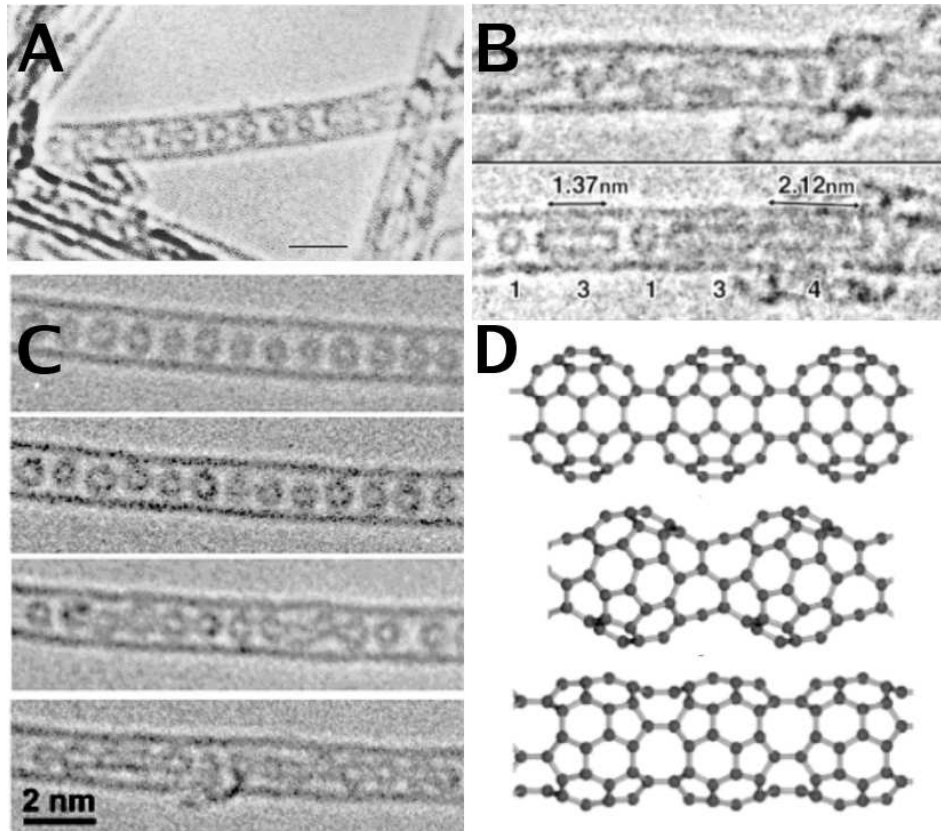
Figure 2.4: (**A**) HRTEM image of encapsulated C_{60} molecules inside a SWNT (nanopeapods) [16]. (**B**) Coalescence of C_{60}, induced by heating, into dimers and trimers [18]. (**C**) Sequence of TEM micrographs showing that electron irradiation promotes the coalescence of C_{60} molecules [19]. (**D**) From top to bottom, the coalesced C_{60} models along the: 2-, 3- and 5-fold axis of symmetry [19].

2.3.2 Carbon nanotori

If a cylinder is bent and the ends are glued together, a torus is formed, with a donut-like topology. Then, by starting with a SWNT with only 6MR a torus can be formed. Figures 2.5A and B show such an example, in particular a (5,5) SWNT section bent into a 900 atom torus with only hexagonal carbon rings. The possibility of forming a torus using sp^2-like hybridized carbon atoms, containing 5MR and 7MR rings in addition to hexagonal rings, was first theoretically predicted by Dunlap [20]. If a (n,n) armchair tube is cut at a $60°$ angle with respect to the tube axis, then a zigzag bonding pattern is inherited for all edge carbon atoms except for the two armchair connections at the highest and lowest points of the cut. Thus,
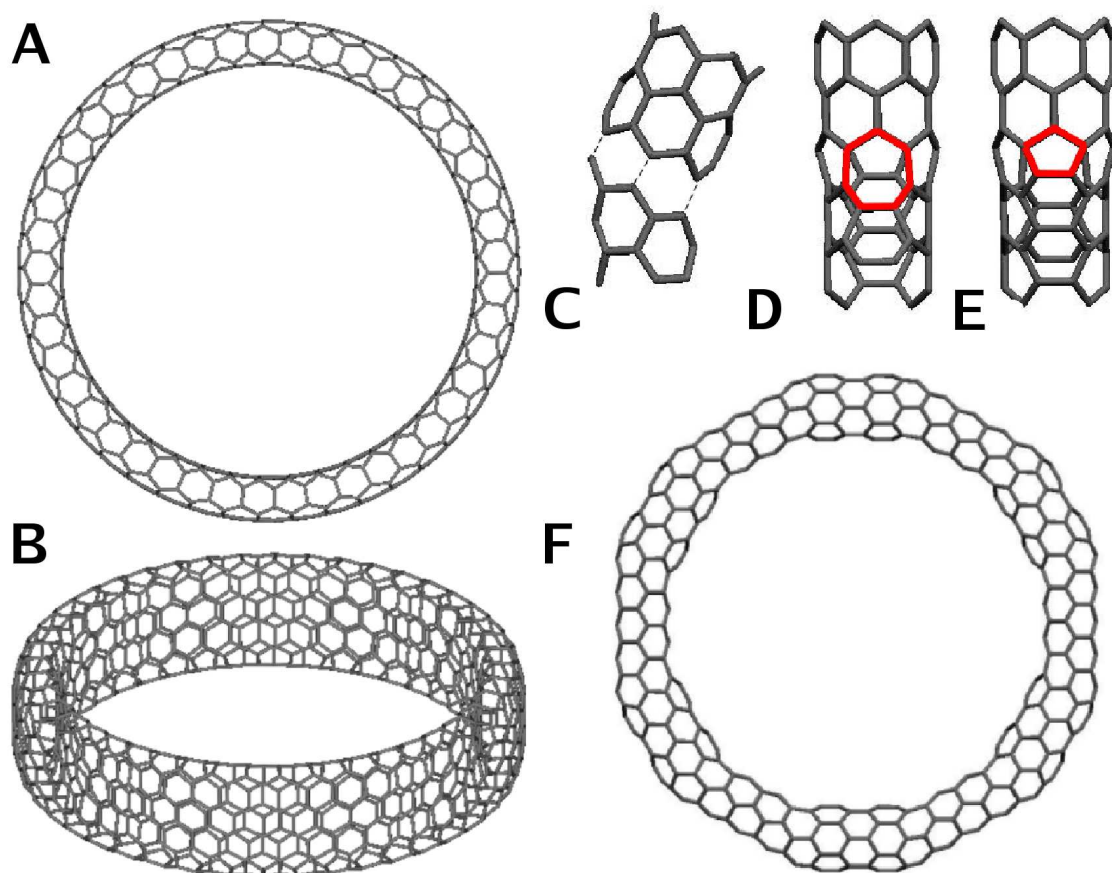
Figure 2.5: (Color) Molecular models of carbon nanotori. (**A**) Top and (**B**) side views of a 900 atom torus generated by joining the ends of a (5,5) SWNT. The structure has only hexagonal rings. (**C**) A (6,0) zigzag tube and a (3,3) armchair tube with a cut at 60° with respect to the tube axis. By connecting these tubes a bent CNT with a (**D**) heptagon and a (**E**) pentagon is created. (**F**) A 540 carbon atom torus, adapted from Dunlap [20].

the appropriate zigzag tube ($2n$,0) couples perfectly at those two points (Fig. 2.5C). In order to compensate for the mismatch in these two regions, a pentagonal and a heptagonal ring need to be added (Figs. 2.5D and E). Tori constructed in this way do not lose the sp^2 bonding nature (Fig. 2.5F). Not long after the report published by Dunlap, a toroidal form of carbon with 5MR, 6MR and 7MR was predicted to have a lower cohesive energy as compared to C_{60} [21].

While examining a batch of SWNT material with scanning force and electron microscopy, Liu *et al.* observed circular formations of SWNT ropes [22]. They called them "crop circles" being skeptical at first of their toroidal nature. However, after a thorough examination, they concluded that some of the tubes in these circular

formations are indeed perfect tori (Figs. 2.6A and B). By employing an acid treatment under sonication on short SWNTs, Martel *et al.* were able to produce rings of SWNTs by a self-organization process [23]. In this case, the analysis suggested that the rings are coiled SWNTs, and not perfect tori (Fig. 2.6C). Carrying out the experiment further, Sano and co-workers lightly etched the tips of SWNTs to obtain oxygen-containing groups at both ends [24]. The ring closure was promoted in these functionalized nanotubes via an organic chemical reaction. The resulting rings apparently were fully closed (Fig. 2.6D). After the experimental observation of carbon tori, special attention was focused on the magnetic response of these types of geometries. Haddon noticed an extremely large and anisotropic ring current diamagnetic susceptibility for a torus containing 5MR and 7MR [25] of about 50 percent that of graphite, on a per-carbon basis. The electronic structure of a polygonal carbon torus obtained by connecting short portions of (6,6) and (10,10) nanotubes with
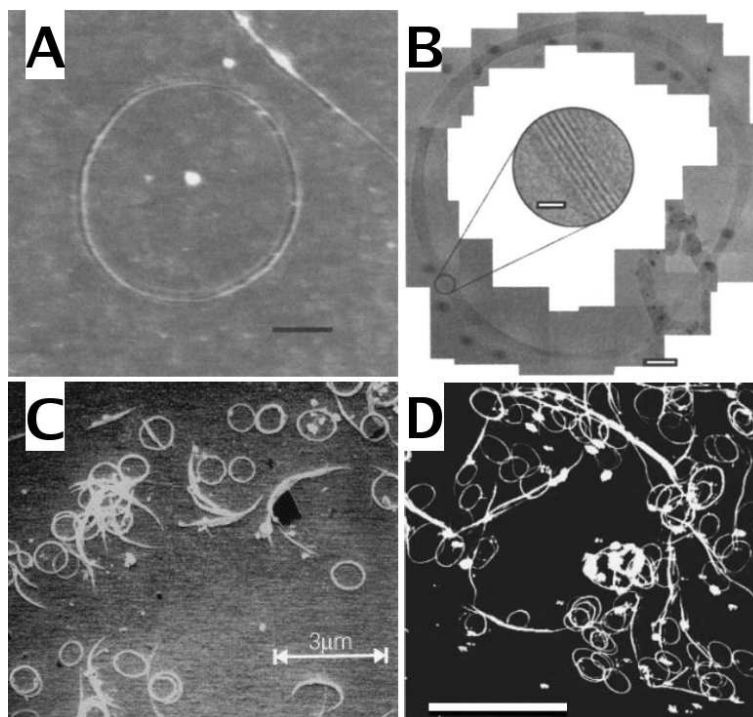
Figure 2.6: Examples of reported experimental carbon tori. (**A**) Scanning force microscopy image (scale bar 100 nm) and (**B**) transmission electron microscopy image (scale bar 15 nm; inset 5 nm) of "crop circle" [22]. (**C**) Rings of SWNTs [23]. (**D**) Atomic force microscopy image of CNTs rings. Scale bar 5 μm. [24]

ten pairs of 5MR and 7MR was predicted to be strongly influenced by a magnetic field of approximately 1.0 T [26]. Surprisingly, an important paramagnetic response was found for carbon nanotori containing only hexagonal carbon rings [27]. It was suggested that the large paramagnetic moment is due to the interplay between the toroidal geometry and the ballistic motion of the π-electrons in the tubes. However, it is noteworthy to emphasize that not all nanotubes bent into a toroidal form exhibit this effect, only those with special characteristics at the Fermi wavelength and radii.

2.3.3 Corrugated carbon nanotori

Topologically, as mentioned above, a carbon nanotorus can be constructed by either cutting and pasting SWNTs of different chirality or by just bending and joining the ends of a SWNT. In the first case, 5MR and 7MR are necessary to close the structure. For the second case, the hexagonal lattice is preserved. By joining the ends of coalesced C_{60} molecules a corrugated torus can be formed, preserving the sp^2-like bonding of graphite. These structures contain 5MR, 7MR and 8MR, besides the hexagonal ones, depending on the symmetry axis of coalescence of the C_{60} units. Figure 2.7 shows examples of the corrugated carbon nanotori as proposed by H. Terrones $et\ al$ [28]. Terrones $et\ al.$ have also proposed a new family of layered sp^2-like carbon crystals by incorporating 5MR, 6MR and 7MR in 2D Bravais lattices. These structures are termed Haeckelites [29]. Particularly, they reported three lattices: (1) Rectangular ($\mathbf{R}_{5,7}$), containing only 5MR and 7MR; (2) Hexagonal ($\mathbf{H}_{5,6,7}$), built by repetitive units of three clustered 7MR, surrounded by alternating 5MR and 6MR; and (3) Oblique ($\mathbf{O}_{5,6,7}$), containing 5MR and 7MR units bound together and surrounded by hexagons (Fig. 2.8). Comparable to the 2D analog of the SWNT, the graphene sheet, these 2D crystals can also form tubular structures [29]. Joining the two ends of the tubular structures forms carbon nanotori. Thus, with the ($\mathbf{R}_{5,7}$) unit, tori containing only pentagons and heptagons can be constructed (Fig. 2.7D).
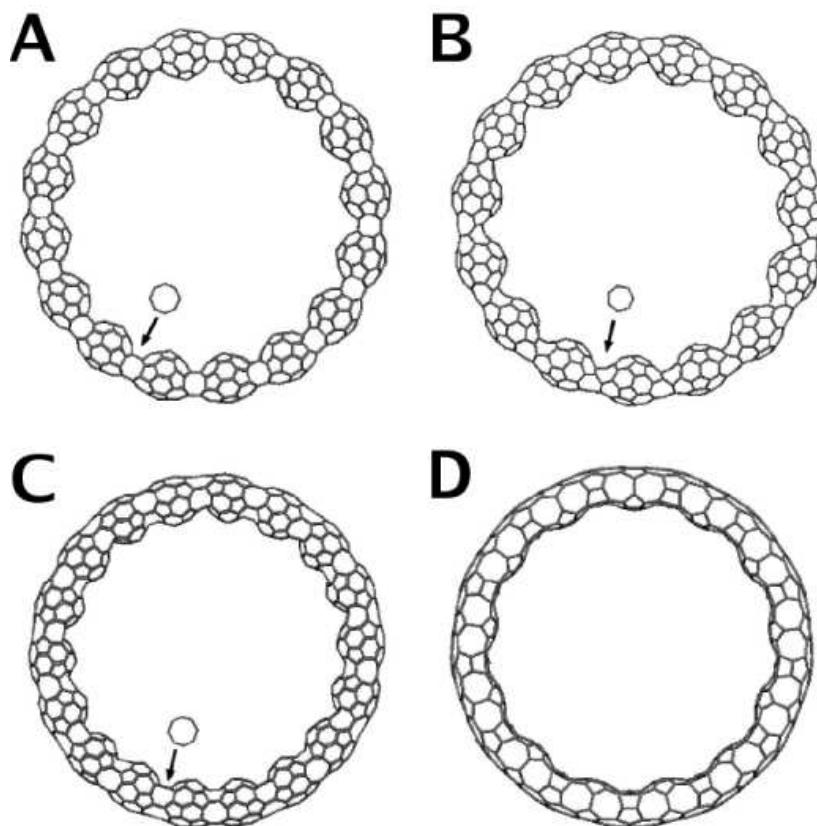
Figure 2.7: Models of carbon nanotori constructed by coalescing C$_{60}$ molecules along the different axes of symmetry: (**A**) 2-fold, 8MR are located at the bottlenecks; (**B**) 3-fold, with 7MR at the bottlenecks and (**C**) 5-fold, with 8MR at the joints. (**D**) Carbon nanotorus constructed by joining the ends of a rectangular Haeckelite nanotube (832 atoms) containing only 5MR and 7MR.
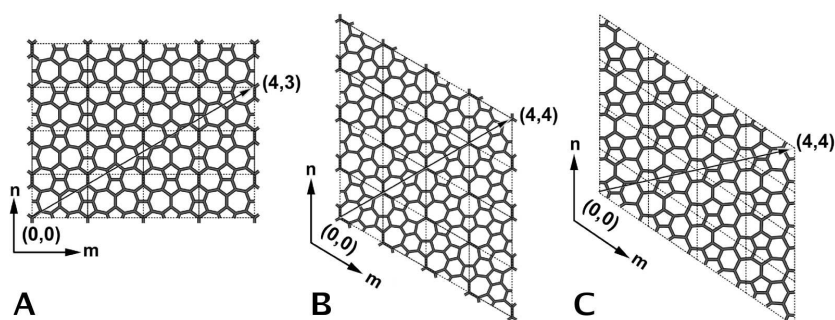
Figure 2.8: Unit cells of layered sp^2-like carbon crystals. (**A**) Rectangular lattice, containing 5MR and 7MR. (**B**) and (**C**) represent the Hexagonal and the Oblique lattices, respectively. Both structures contain 5MR, 6MR and 7MR. Adapted from [29].

2.4   The London theory

The motion of an electron in a uniform static magnetic field $\mathbf{H}^{\S}$ is described in quantum mechanics by the transformation of the momentum operator $\mathbf{p}$ to $(\mathbf{p} + \frac{e}{c}\mathbf{A})$ in the Hamiltonian, where $\mathbf{A}$ is the vector potential $(\mathbf{B} = \nabla \times \mathbf{A})$. Then, for an electron interacting with an electromagnetic field, the complete Hamiltonian is defined as

$$\mathcal{H} = \frac{1}{2m_e}(\mathbf{p} + \frac{e}{c}\mathbf{A})^2 - e\phi, \tag{2.2}$$

where m_e is the electron mass and ϕ the electric potential. If only the magnetic interaction is considered, then $\phi = 0$. In the London approximation [30, 31], first developed to study the response of π-conjugated carbon molecules under the influence of a magnetic field, the molecular orbitals are obtained with a linear combination of gauge-invariant atomic orbitals $|\varphi_i\rangle$

$$|\psi_n\rangle = \sum_i C_i^n |\varphi_i\rangle, \tag{2.3}$$

where

$$|\varphi_i\rangle = \exp\left(-\frac{ie}{\hbar c}\mathbf{A}_i \cdot \mathbf{r}\right)|\phi_i\rangle, \tag{2.4}$$

and the index i identifies the ith atom, $|\phi_i\rangle$ its atomic orbital (in our analysis a p orbital), $\mathbf{A}_i$ is the vector potential at position $\mathbf{R}_i$, and $\hbar$ is Planck's constant divided by two times π. The variation of the vector potential to distances of the bond length is ignored and the phase is calculated at the bond center between atoms. Considering these assumptions together with nearest neighbor electronic hoppings, the following Hamiltonian matrix is derived

$$\mathcal{H}_{ij} = \exp\left(i\theta_{ij}\right)\mathcal{H}_{ij}^0, \tag{2.5}$$

where $\mathcal{H}_{ij}^0$ are the Hamiltonian matrix elements for a zero magnetic field, and where

$$\theta_{ij} = \frac{e}{2\hbar c}\left(\mathbf{A}_i - \mathbf{A}_j\right) \cdot \left(\mathbf{R}_i + \mathbf{R}_j\right). \tag{2.6}$$

---

§In CGS units the permeability of free space is unity, thus the magnetic induction $\mathbf{B}$ and the applied field $\mathbf{H}$ are numerically equivalent in vacuum.

For example, the vector potential $\mathbf{A}$ for a constant magnetic induction $\mathbf{B}$ in the z direction can be expressed as

$$\mathbf{A} = \frac{1}{2}\mathrm{B}\left(-y\hat{\mathbf{i}} + x\hat{\mathbf{j}}\right), \tag{2.7}$$

since

$$\nabla \times \mathbf{A} = \mathrm{B}\hat{\mathbf{k}}. \tag{2.8}$$

In this particular case, if we substitute the vector potential in Eq. (2.6), the phase term takes the following form

$$\theta_{ij} = \frac{e\mathrm{B}}{2\hbar c}\left(x_i y_j - x_j y_i\right). \tag{2.9}$$

An extension of the method gives the ring currents directly [8]. The current $\mathbf{J}_{ij}$ of the site $\mathbf{R}_i$ to the site $\mathbf{R}_j$, to first neighbors, can be expressed as

$$\mathbf{J}_{ij} = \left[\sum_n (C_i^n)^* C_j^n\right] \exp\left\{\frac{ie}{2\hbar c}\left[\mathbf{A}_i - \mathbf{A}_j\right] \cdot (\mathbf{R}_i + \mathbf{R}_j)\right\}\mathbf{j}_{ij}, \tag{2.10}$$

where the sum is over occupied states, and $\mathbf{j}_{ij}$ is a vector with the direction of the bond and can be related with its strength. The sum $\mathbf{J}_{ij} + \mathbf{J}_{ji}$, gives the total current for the ij bond, and it is a real number. For structures with toroidal geometry a *total* magnetic moment can be calculated in terms of the induced total current $\boldsymbol{i}_t$ in the torus and the enclosed area as $\mu = \boldsymbol{i}_t\sigma$, where σ represents the enclosed area [27]. For small values of the magnetic field $\mathbf{H}$, the π-electron ring current magnetic susceptibility χ_{RC} is obtained directly from the energy E with the equation [32]

$$-\frac{1}{2}\chi_{\mathrm{RC}}\mathrm{H}^2 = E(\mathrm{H}) - E(0). \tag{2.11}$$

With this set of equations it is possible to calculate the electronic energy, the induced ring current pattern and the χ_{RC} for carbon structures with sp^2-bonding characteristics.

By convention, the ring current magnetic susceptibility χ_{RC} is quoted in units of the value for benzene with the applied magnetic field perpendicular to the plane of the hexagonal ring, χ_b [33]. Equation (2.11) gives only the π-electron ring current susceptibility. In addition, the contribution from bounded electrons must be taken into account in order to calculate the total magnetic susceptibility. Then, estimated

values of the magnetic susceptibility will depend on the assumed local contribution of the atoms under consideration. In the following discussion, the empirical estimation of localized contributions to the magnetic susceptibility is taken for granted, unless noted otherwise, so we will drop the subscript RC on χ.

2.5 Benzene, C_{60} and C_{70}: case studies

The concepts described so far are first applied to benzene, for various reasons: Benzene (C_6H_6) is well studied and usually used as an example in literature when discussing closed-ring carbon structures. Besides, to rationalize the results shown below, the magnetic susceptibility as well as the inter-atomic current values are given in units of the value for benzene with the magnetic field applied perpendicular to the plane of the ring. The estimated χ of benzene for an external magnetic field perpendicular to the plane of the ring is, from Eq. (2.1), $\chi_b = -49$ CGS p.p.m. mol^{-1}, in close agreement with modern estimates of the quantity (-34 ± 7 CGS p.p.m mol^{-1}) [1, 7]. Since benzene is diamagnetic, the current that is induced produces a magnetic field that opposes the applied one. The inter-atomic currents can be calculated from Eq. (2.10), which gives both the intensity and the direction of the currents. Figure 2.9 shows the resulting current pattern for an applied field of 1.0 kGs (0.1 T). In benzene all carbon atoms are equivalent, so the induced currents $\boldsymbol{i}_{ij}$ ($= \boldsymbol{i}_b$) are all equal in magnitude, and the diamagnetic response can be seen by considering the field that the ring currents induce, which is opposite in direction to the applied one. When applying Eq. (2.1) it was assumed that the charge distribution has cylindrical symmetry about the z axis (the axis of the applied magnetic field), so it correctly describes the ring current magnetism of benzene, because the π-electrons move in an approximately cylindrical potential in benzene. By expanding the Hamiltonian function (Eq. (2.2)) for an electron subjected to an external magnetic field of constant strength H (parallel to the z axis), the next expression is obtained

$$\mathcal{H} = \mathcal{H}^0 + \mathcal{H}' + \mathcal{H}'', \tag{2.12}$$
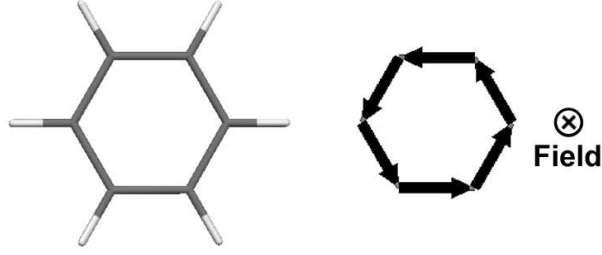
Figure 2.9: Molecular model of benzene (C$_6$H$_6$) (left) and induced ring current pattern (right) for an applied magnetic field perpendicular to the plane of the molecule. Arrows represent the currents between adjacent carbon atoms and their size is proportional to the current magnitude. For benzene all the inter-atomic currents i_{ij} ($= i_b$) are equal and they induce a magnetic field opposite in direction to the applied one.

in which the $\mathcal{H}^0$ is the Hamiltonian function for zero field strength, and the other two terms can be expressed as [3]

$$\mathcal{H}' = -(\mathrm{H}e/2mc)(xp_y - yp_x) \tag{2.13}$$

and

$$\mathcal{H}'' = (\mathrm{H}^2 e^2/8mc^2)(x^2 + y^2). \tag{2.14}$$

By applying perturbation theory to the expanded Hamiltonian, the χ can be calculated. The final expression for the total (molar) χ_t can be divided into two contributions: a diamagnetic part χ_d (negative), and a paramagnetic part χ_p (positive) [34]

$$\chi_t = \chi_d + \chi_p \begin{cases} \chi_d = & -(N_A e^2/6m_e c^2)\langle r^2 \rangle \\ \chi_p = & (N_A e^2/6m_e c^2)\sum_n |l_{0n}|^2/\Delta E_{n0}, \end{cases} \tag{2.15}$$

where the terms have the same meaning as in Eq. (2.1), $l_{0n} = \langle 0|l|n \rangle$ is an angular momentum term and $\Delta E_{n0} = E_n - E_0$. It is important to realize that the paramagnetic term of Eq. (2.15) has nothing to do with electron spin, and unlike spin paramagnetism, is independent of the temperature [34]. The negative part is the Langevin-Larmor expression (Eq. (2.1)) that only takes into account the diamagnetic contribution, but by calculating the χ with Eq. (2.11) both contributions to χ (positive and negative) are taken into account. If the length of the carbon-carbon bond $a = 1.4$ Å is taken as unit length and the resonance integral $\beta = \mathcal{H}_{ij}^0$ as the unit of energy, then the unit for χ is $\beta(e/\hbar c)^2 a^4$ [32]. In these units, Eq. (2.11) gives

a value for benzene of $\chi_b = -1.5$. Then, for a resonance integral value of $\beta = 2.72$ eV (benzene), $\chi_b = -34.8$ CGS p.p.m mol^{-1} is obtained, a lower value than the one calculated only with the Langevin-Larmor term and in closer agreement with the experimental value of -34 ± 7 CGS p.p.m mol^{-1} [1, 7].

For C_{60}, a value of $\chi_{C_{60}}/|\chi_b| = -40.9$ is derived from Eq. (2.1), 41 times the ring current χ of benzene. This would imply a theoretical value of $\chi_{C_{60}} \sim -1500$ CGS p.p.m. mol^{-1}, a rather large diamagnetic response. However, if Eq. (2.11) is used instead, and the strength of all the bonds is considered equal, a value of $\chi_{C_{60}}/|\chi_b| = 0.21$ is obtained [6]; thus, the $\chi_{C_{60}}$ is smaller than that of benzene and has a different sign (paramagnetic). If a difference in strength between the bonds at the junction of two 6MR and those between a 5MR and a 6MR is considered for C_{60}, the value for the susceptibility changes to $\chi_{C_{60}}/|\chi_b| \sim -0$–3, a diamagnetic behavior, but still with a much lower value than the one predicted by the Larmor-Langevin expression (Eq. (2.1)). Experimental measurements confirmed that the ring current magnetic susceptibility of C_{60} is small. The measured value of -260 CGS p.p.m mol^{-1} for the total magnetic susceptibility of C_{60} can be entirely assigned to local contributions to the diamagnetism [7, 35]. At first glance, this result suggested that only small ring currents could be induced in the C_{60} cage. However, a more precise analysis of the ring current pattern generated in C_{60} showed that the $\boldsymbol{i}_{ij}$ currents are not small, but that a cancellation effect occurs between diamagnetic
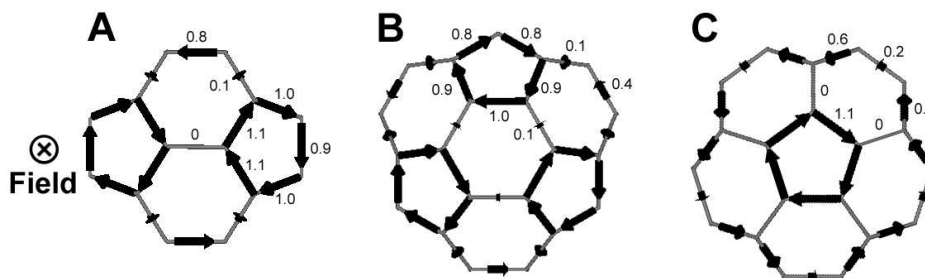
Figure 2.10: Induced ring current patterns in C_{60} for an applied magnetic field parallel to the (**A**) 2-fold, (**B**) 3-fold and (**C**) 5-fold axis of symmetry. For clarity only the top part of the molecule is shown. The magnetic field is pointing inwards to the page. The current strength is given with respect to that of benzene, and the size of the arrows is proportional to the current magnitude in each case.
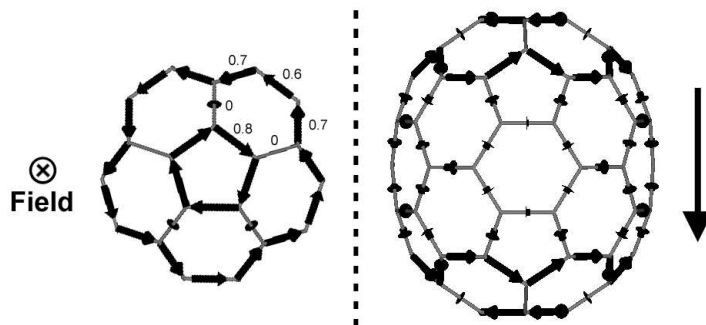
Figure 2.11: Induced ring current pattern in C_{70}. The top (left) and side (right) views are shown. The arrow shows the direction of the field for the side view. The current strength is given with respect to that of benzene, and the size of the arrows is proportional to the current magnitude in each case.

and paramagnetic currents [8]. Figure 2.10 shows the induced current patterns in C_{60} when the magnetic field (1 kGs) is applied along the three symmetry axes, as calculated from Eq. (2.10). The first difference with the ring current pattern of benzene (cf. Fig. 2.9) is that not all the $\boldsymbol{i}_{ij}$ currents are equal. In fact, for some bonds no current flows at all. Since the larger currents are on the order of $\boldsymbol{i}_b$ (for the same field), if all were diamagnetic (counterclockwise in our convention) a large diamagnetic $\chi_{C_{60}}$ should be expected. But it is clear from Fig. 2.10 that the currents in the pentagons are paramagnetic (clockwise). Thus, the small value for $\chi_{C_{60}}$ is produced by a cancellation effect between paramagnetic and diamagnetic ring currents.

By applying Eq. (2.11) to C_{70} a value of $\chi_{C_{70}}/|\chi_b| = -6.7$ is obtained, which predicts a stronger diamagnetic response when compared to C_{60}. The enhancement

Table 2.1: Ring current χ and maximum $\boldsymbol{i}_{ij}$ for C_{60} and C_{70}. The $\parallel$ ($\perp$) indicates that the magnetic field is taken parallel (perpendicular) to the principal axis. The χ are given in units for the value for benzene with a field perpendicular to the ring. Negative values indicate a diamagnetic response. The $\boldsymbol{i}_{ij}^{max}$ currents are in units of $\boldsymbol{i}_b$.

Molecule	$\chi_{\parallel}$	$\chi_{\perp}$	$\langle\chi\rangle$	(CGS p.p.m mol^{-1})	$\boldsymbol{i}_{ij}^{max}(\parallel)$	$\boldsymbol{i}_{ij}^{max}(\perp)$
C_{60}	0.24	0.22	0.23	8 ± 2	1.13	1.09
C_{70}	-5.15	-7.48	-6.70	-228 ± 47	0.77	1.10

in diamagnetism in C_{70} was confirmed experimentally [7] and can be explained from the ring current pattern shown in Fig. 2.11. Although the $\boldsymbol{i}_{ij}$ currents in the pentagon are paramagnetic, the diamagnetic $\boldsymbol{i}_{ij}$ currents are stronger than for C_{60} (cf. Fig. 2.10A). Besides, since the 5MR are responsible for quenching the diamagnetism, the larger fraction of 6MR to 5MR in C_{70} also accounts for the higher diamagnetism shown by C_{70} relative to C_{60}. These findings are summarized in Table 2.1.

2.6 Polymerized C_{60} and C_{70} molecules

As mentioned in section 2.3, C_{60} molecules contained inside SWNTs coalesce at high temperatures or by electron irradiation. In this section we investigate the magnetic response of such polymerized fullerenes.

In principle, the coalescence process of two C_{60} molecules will depend strongly on how the molecules merge. If sp^3 bonding is excluded in the merging process and the two adjacent molecules are oriented along the same axis of symmetry before coalescence, then three models for the polymerized molecules are obtained, each one along the 2-, 3- or 5-fold axis of symmetry, as shown in Fig. 2.12. All models only contain sp^2-like hybridized atoms, every carbon atom is connected to three neighbors, and carbon rings with more than six sides are needed. In other words, local negative Gaussian curvature is required to accomplish full coalescence. The 2-fold dimer model consists of 116 atoms and has 8MR in the junction (Fig. 2.12A). The 3-fold dimer model possesses 120 atoms, and for this case 7MR are needed to close the structure (Fig. 2.12B). Finally, for the 5-fold case, 110 atoms are necessary and 8MR form the neck of the junction (Fig. 2.12C). It is clear that only the 3-fold model does not need to lose any atoms from the original C_{60} molecules. However, in irradiation experiments (with electrons or ions), atoms are ejected from the cages via knock-on processes. In fact, it has been shown that carbon atoms belonging to the interior fullerenes could be displaced at higher rates than those belonging to the surrounding SWNT because of a difference in strain energy. For simplicity, a notation is introduced to name these structures. Considering the three axes of symmetry as C2, C3 and C5, we name a linear chain constructed by n C_{60} units
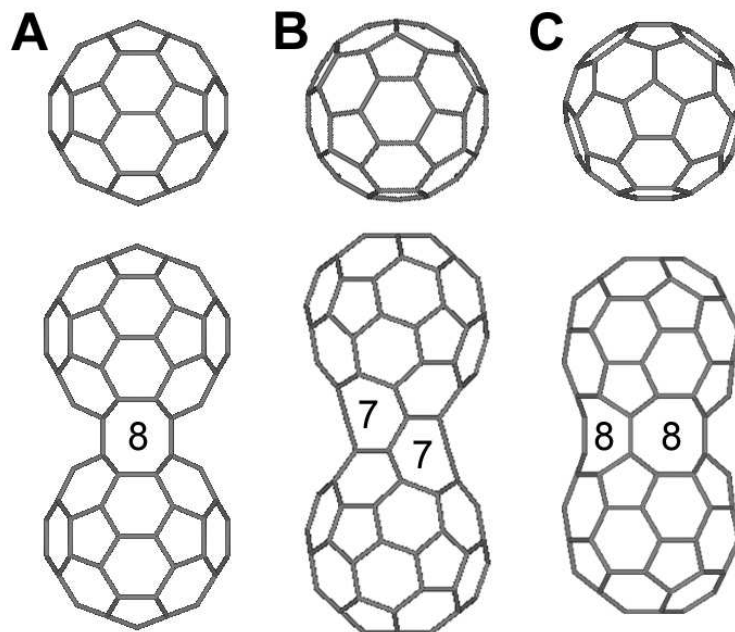
Figure 2.12: Molecular models for the dimers formed by joining C$_{60}$ molecules. The images in (**A**), (**B**) and (**C**) correspond to molecules connected along the 2-, 3-, and 5-fold axis of symmetry, respectively. The first row depicts the top view, whereas the second row shows the side view. The number of atoms is different in each case: in (**A**) 116, in (**B**) 120, and in (**C**) 110. The label numbers indicate the number of sides of the corresponding polygon.

along the C2 symmetry axis as nC$_{60}$-C2(8), where the number inside the parenthesis indicates the type of rings present in the necks. Similarly, for the other axes of symmetry polymerized chains are called nC$_{60}$-C3(7) and nC$_{60}$-C5(8).

Table 2.2 summarizes the results for the C$_{60}$ dimers, where the χ as well as

Table 2.2: Ring current χ and maximum $\boldsymbol{i}_{ij}$ for C$_{60}$ dimers. The $\parallel$ ($\perp$) indicates that the magnetic field is taken parallel (perpendicular) to the principal axis. The χ are given in units for the value for benzene with a field perpendicular to the ring. Negative values indicate a diamagnetic response. The $\boldsymbol{i}_{ij}^{max}$ currents are in units of $\boldsymbol{i}_b$.

Molecule	$\chi_\parallel$	$\chi_\perp$	$\langle\chi\rangle$	$\boldsymbol{i}_{ij}^{max}(\parallel)$	$\boldsymbol{i}_{ij}^{max}(\perp)$
2C$_{60}$-C2(8)	4.12	2.61	3.11	1.02	1.17
2C$_{60}$-C3(7)	1.01	−10.99	−7.00	0.96	0.96
2C$_{60}$-C5(8)	−6.14	−7.89	−7.30	0.97	1.11

the maximum ring currents are shown for each case. For the dimers, the currents $\boldsymbol{i}_{ij}$ are almost the same as for C_{60}, however, the susceptibility values are different. Of the three dimers, only the $2C_{60}$-C2(8) preserves the paramagnetic response of the C_{60} building unit. Although the dimer $2C_{60}$-C3(7) is also paramagnetic for a magnetic field parallel to the principal axis, the large diamagnetic response for a field perpendicular to the principal axis makes it diamagnetic on average. For the $2C_{60}$-C5(8) the change is complete. For both directions of the applied field the molecule is diamagnetic. For the three cases, there is an increment of one order of magnitude in the $|\chi|$ (per mol) when compared to the $\chi_{C_{60}}$.

In order to understand the χ values for the C_{60} dimers, the flow of inter-atomic currents was calculated. Figure 2.13 shows the induced current patterns for the C_{60} dimers for a magnetic field parallel to the the principal axis of the structures. These patterns correspond to the $\chi_{\parallel}$ values of Table 2.2. Since the current patterns at the caps are similar to those of the unmodified individual C_{60} molecules (cf. Fig. 2.10), the changes in susceptibility must come from somewhere else. For the $2C_{60}$-C2(8) and the $2C_{60}$-C3(7) dimers the $\boldsymbol{i}_{ij}$ currents concentrated at the 5MR and the necks
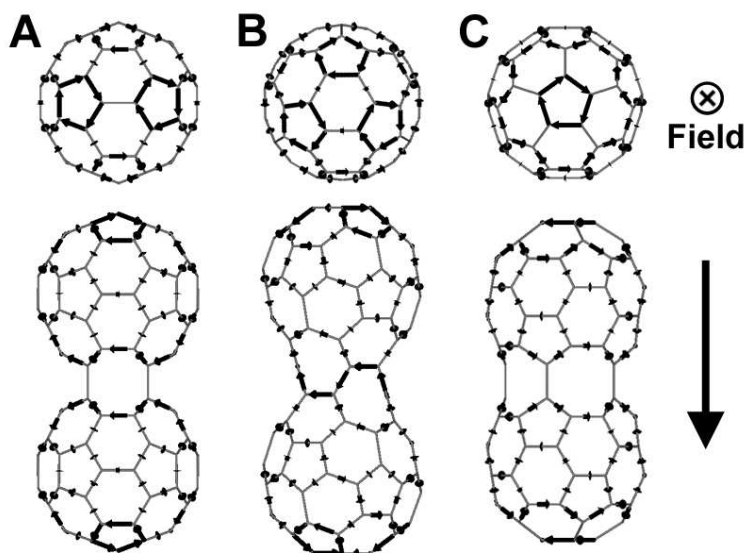
Figure 2.13: Induced ring current patterns in C_{60} dimers. The applied magnetic field is parallel to the principal axis of the structures (**A**) $2C_{60}$-2C(8), (**B**) $2C_{60}$-3C(7) and (**C**) $2C_{60}$-5C(8). The first row depicts the top view, whereas the second row shows the side view. The currents are normalized for each case and the size of the arrows is proportional to the current magnitude.

give a paramagnetic response (Figs. 2.13A and B). In contrast, for the 2C$_{60}$-C5(8) dimer only the 5MR gives a paramagnetic response, and all the other $\boldsymbol{i}_{ij}$ currents flow in the opposite direction, thus, the dimer is diamagnetic, in this particular direction (Fig. 2.13C).

Since the 2C$_{60}$-C5(8) dimer is the one that showed the largest increment in absolute value in the magnetic susceptibility (per carbon atom) with respect to the C$_{60}$ unit, we investigated the effect of adding more C$_{60}$ units to this complex in order to form larger linear chains (Fig. 2.14). The addition of a C$_{60}$ unit to the 2C$_{60}$-C5(8) dimer produces the linear chain 3C$_{60}$-C5(8). Surprisingly, for this complex, the induced ring currents are four orders of magnitude larger than the ones
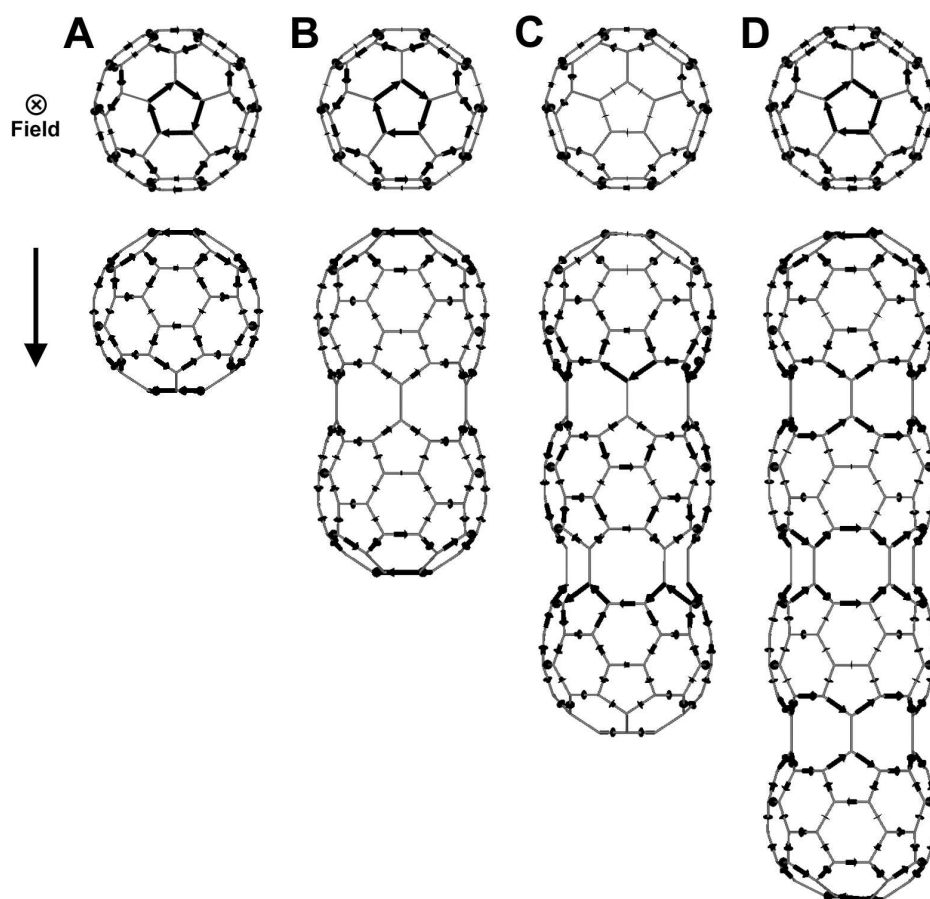
Figure 2.14: Induced ring current patterns for the linear chains nC$_{60}$-C5(8), for $n =$ (**A**) 1, (**B**) 2, (**C**) 3 and (**D**) 4. The applied magnetic field is parallel to the principal axis of the structures. The first row depicts the top view, whereas the second row shows the side view. The currents are normalized for each case and the size of the arrows is proportional to the current magnitude.

in benzene, and their combined flow produces a paramagnetic response (Fig. 2.14C). For $4C_{60}$-C5(8), the inter-atomic currents drop again to values $\sim i_b$, resulting in a diamagnetic response (Fig. 2.14D). As the polymerized chain is enlarged by the addition of extra C_{60} units, the oscillatory behavior between diamagnetism and paramagnetism continues, as can be seen in Table 2.3, where values of $\chi_\parallel$, calculated for a magnetic field parallel to the principal axis of the structures, are given for chains up to ten units ($10C_{60}$-C5(8)). The $\chi_\perp$ values (not shown) for these structures show the same oscillatory behavior. It is easy to recognize that paramagnetism is associated with large currents in these structures, with the sole exception of C_{60}, which is paramagnetic and exhibits induced inter-atomic currents of the order of i_b. For the diamagnetic chains, the calculated susceptibilities (considering $\chi_b^\perp \sim -5.6$ CGS p.p.m. per mol C [1]) are on the order of ~ -3 CGS p.p.m. per mol C [1], which are comparable to the response of diamond, $\chi_{\text{diamond}} = -5.5$ CGS p.p.m. per

Table 2.3: Ring current χ and maximum i_{ij} for nC_{60}-C5(8) and nC_{70}-C5(8) and linear chains The $\parallel$ indicates that the magnetic field is taken parallel to the principal axis. The values of χ are given in units for the value for benzene with a field perpendicular to the ring. Negative values indicate a diamagnetic response. The i_{ij}^{max} currents are in units of i_b.

n	nC_{60}-C5(8)		nC_{70}-C5(8)	
	$\chi_\parallel$	$i_{ij}^{max}(\parallel)$	$\chi_\parallel$	$i_{ij}^{max}(\parallel)$
1	0.24	1.13	-5.15	0.77
2	-6.14	0.97	3418.52	28915.52
3	1735.32	17756.04	-22.21	0.98
4	-19.80	1.05	3617.27	14543.04
5	-25.12	1.03	-40.55	1.00
6	1749.43	8861.40	3623.65	9713.73
7	913.68	6753.88	-59.23	1.00
8	-46.71	1.01	3616.94	7292.03
9	-51.70	1.01	-77.88	1.00
10	1097.16	4976.65	3605.60	5836.78
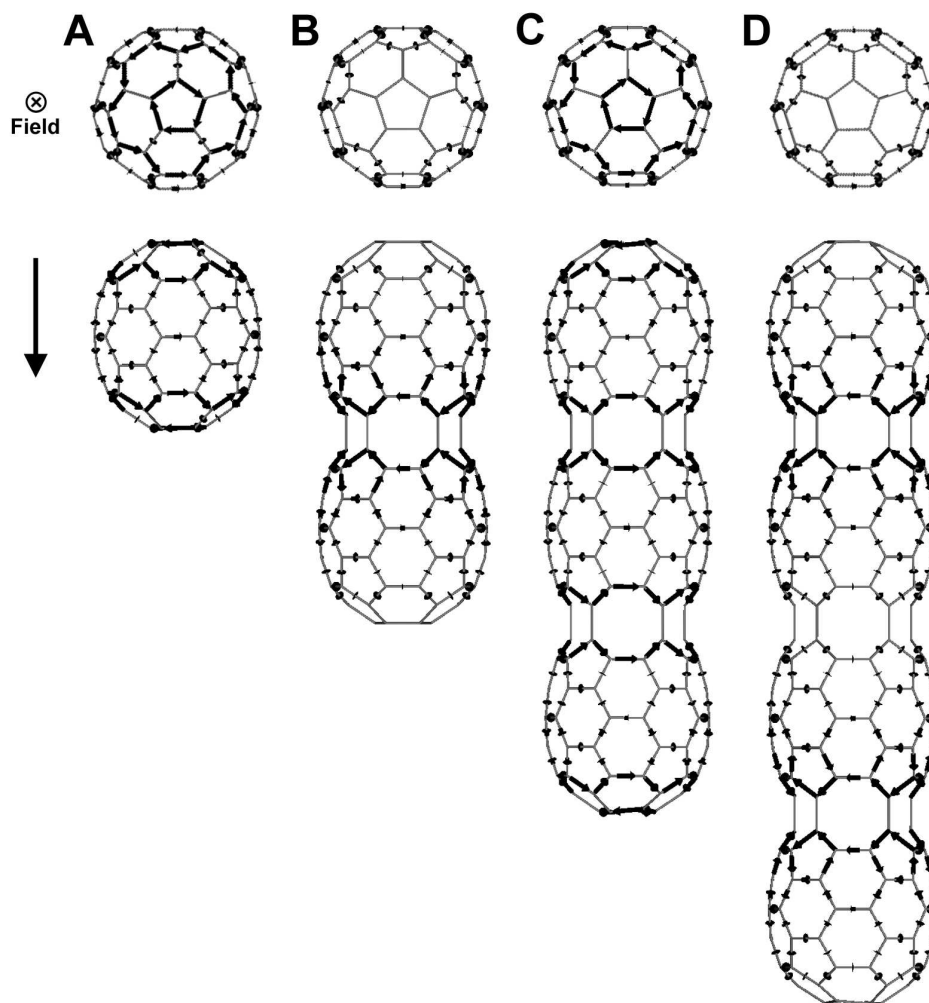
Figure 2.15: Induced ring current patterns for the linear chains nC$_{70}$-C5(8), for $n = $ (**A**) 1, (**B**) 2, (**C**) 3 and (**D**) 4. The applied magnetic field is parallel to the principal axis of the structures. The first row depicts the top view, whereas the second row shows the side view. The currents are normalized for each case and the size of the arrows is proportional to the current magnitude.

mol C [1]. For the paramagnetic complexes, the contribution from the ring current susceptibility is larger. For example, for 6C$_{60}$-C5(8) we obtained $\chi_{\parallel} = 192$ CGS p.p.m per mol C, which is more (in absolute value) than the total susceptibility of graphite, that is -97.2 CGS p.p.m per mol C [2]. From Table 2.3 it can be seen that as the size of the C$_{60}$ chains grow, the paramagnetic response starts to drop.

The same analysis was done for polymerized C$_{70}$ molecules along the 5-fold axis of symmetry, and the results are shown in Table 2.3. As for the polymerized C$_{60}$ molecules, for the C$_{70}$ chains there is an oscillatory behavior between paramagnetism

and diamagnetism as the chain length increases, and paramagnetism is associated
with large ring currents. Interestingly, for the nC$_{70}$-C5(8) polymerized chains, the
change in χ occurs for every extra unit. That is, a one to one correspondence exists
between the addition of a C$_{70}$ unit and the sign of χ, where for nC$_{70}$-C5(8) with
n odd the structures are diamagnetic and for n even are paramagnetic. Also, the
paramagnetic response is stronger by a factor of two compared to the C$_{60}$ chains
and drops slower for an increment in length. Figure 2.15 shows the induced ring
current patterns for four nC$_{70}$-C5(8) complexes. These results show that by clever
construction the magnetic properties of carbon nanostructures can be tuned.

2.7   Nanotori from SWNT (only hexagonal rings)

It has been predicted that carbon nanotubes bent into toroids (see Figs. 2.5A
and B) could show unusually large paramagnetic moments when subjected to an
external magnetic field [27]. These structures formed by only 6MR permit the flow
of induced currents along the donut-shape geometry, generating a magnetic moment
$\mu = \boldsymbol{i}_t \sigma$, where $\boldsymbol{i}_t$ is the total current along the torus and σ the enclosed area. Figure
2.16 depicts the schematic representation of the paramagnetic (Fig. 2.16A) and dia-
magnetic (Fig. 2.16B) response of carbon nanotori for a magnetic field perpendicular
to the plane of the tori. The magnitude of the induced magnetic moment depends
on the size of the torus (area) and on the magnitude of the current. Moreover, if
no current flows around the complete torus, the circuit is open and no magnetic
moment is induced ($\mu = 0$). Not all carbon nanotori are paramagnetic. Specifically,
those formed from metallic nanotubes with $\lambda_F = 3T$, where λ_F is the Fermi wave-

Figure 2.16: Schematic representation of the total induced current in a (**A**) paramagnetic and
a (**B**) diamagnetic carbon nanotorus. The direction of the magnetic field is given by the vertical
arrow.

length and T the translation vector of the nanotube, exhibit paramagnetic moments at selected radii, while the ones with $\lambda_F = T$ are paramagnetic at any radius. All nanotori formed from semiconducting tubes are diamagnetic [27]. For example, a (5,5) SWNT is metallic with $\lambda_F = 3T$, so tori formed from this tube will exhibit a paramagnetic moment at 0 K for selected radii. For the 1020 atom (5,5) nanotorus the calculated magnetic moment for a magnetic field of 1 kGs (0.1 T) is 68.55 μ_{B}. This magnetic moment corresponds to a value of ~ 31 emu/g, compared to a value of -30×10^{-3} emu/g for graphite under the same applied field along the c axis [36]. Thus, this carbon nanotorus possesses a paramagnetic moment having a strength three orders of magnitude stronger than the diamagnetic moment of graphite at 1 kGs. As stated earlier, the modification of the Hamiltonian, for an electron, to include the magnetic field is accomplished by the introduction of a phase term (see Eq. (2.5)). This implies that expressions that depend on the magnetic field (through the vector potential) will oscillate. Moreover, it has been proved both theoretically and experimentally that to observe these oscillations in carbon nanostructures magnetics fields as high as 450 kGs (45 T) are required [10, 37]. The study of carbon nanostructures in such large fields is out of the scope of this analysis. However, for the analyzed structures we observe no important change in the magnetic moment up to 10 kGs (1 T). The radius of the torus increases by adding SWNT unit cells and decreases by subtracting them. Since the unit cell of the (5,5) SWNT has 20 atoms, the nearest enlarged torus to the one containing 1020 atoms is the 1040 atom torus, which shows a diamagnetic moment of $\mu = -5 \times 10^{-2} \; \mu_{\mathrm{B}}$. For the next two enlarged tori, of 1060 and 1080 atoms, the magnetic moments are $\mu = -5 \times 10^{-2} \; \mu_{\mathrm{B}}$ and $\mu = 72.47 \; \mu_{\mathrm{B}}$, respectively. The appearance of large paramagnetic moments for selected radii in the tori constructed from a (5,5) SWNT becomes evident when the magnetic moment as a function of the size of the tori is plotted, as shown in Fig. 2.17 for a magnetic field of 1 kGs. If diamagnetic tori are not considered, there exists a linear relation between the size of the torus and the paramagnetic moment, as shown in Fig. 2.17 (gray line). From this linear relation, a paramagnetic moment per carbon atom can be estimated. All tori constructed from armchair (n,n) SWNTs behave similarly to the tori formed from a (5,5) SWNT described above.
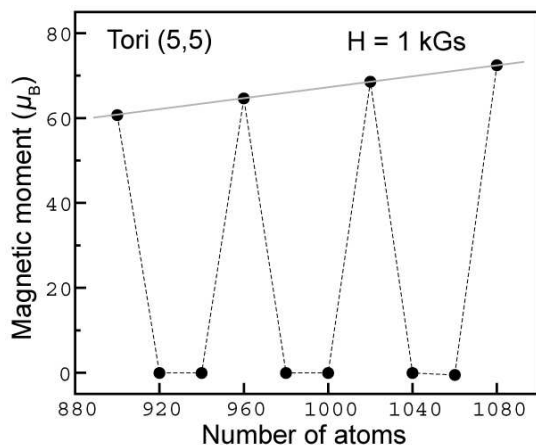
Figure 2.17: Magnetic moment as a function of size for tori formed from a (5,5) SWNT. The magnitude of the magnetic field is 1 kGs. The gray line shows the linear behavior of the magnetic moment as a function of tori size if diamagnetic tori are not considered.
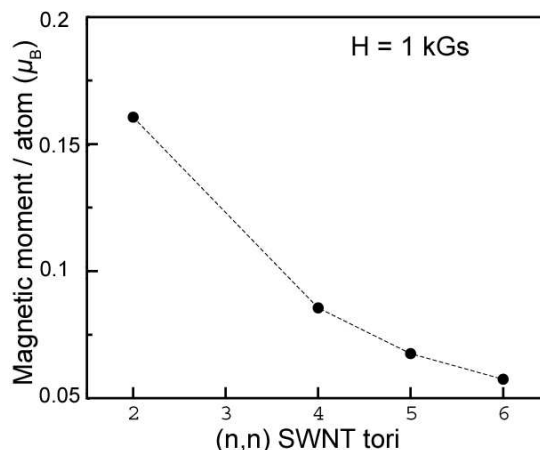
Figure 2.18: Magnetic moment per carbon atom for paramagnetic tori formed from (n,n) SWNTs, for a magnetic field H= 1 kGs. The magnetic moment drops as n increases. The line is to guide the eye.

That is, they all exhibit paramagnetic moments at selected radii. Figure 2.18 shows the estimated paramagnetic moment per carbon atom for an applied field of 1 kGs as a function of the building (n,n) nanotube. It is clear that as the diameter of the tori increases (increasing n), the magnetic moment drops. Thus, tori with small diameters should show the largest paramagnetic moments, for tori constructed from (n,n) SWNTs.

As for coalesced fullerenes (see section 2.6), large paramagnetic moments are associated with large currents, since $\mu = i_t \sigma$. Figure 2.19 shows the current patterns for a diamagnetic and a paramagnetic torus formed from a (5,5) SWNT, for a magnetic field parallel to the nanotori axis. In both cases a current circulates around the structure in the plane perpendicular to the magnetic field; however, the directions of the currents are different. For the diamagnetic 1400 atom torus (Fig. 2.19A) the inter-atomic currents have values of ~ 3 i_b and the direction of circulation is counterclockwise. In order to calculate the total current necessary to estimate the magnetic moment, the individual i_{ij}'s that pass through an imaginary plane parallel to the nanotorus internal diameter are added. For the paramagnetic 1500 atom
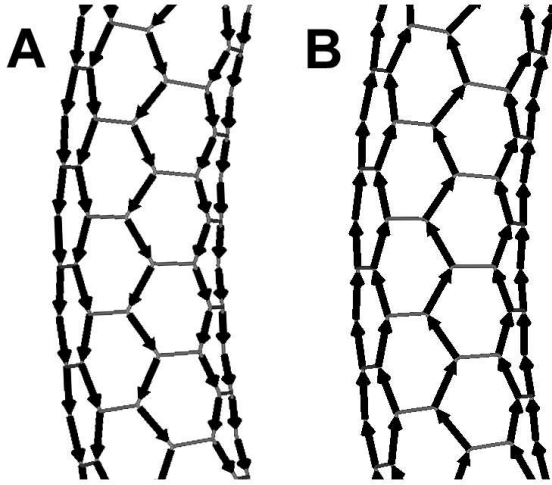
Figure 2.19: Induced ring current patterns for carbon nanotori formed by joining a (5,5) SWNT segment, for a magnetic field perpendicular to the plane of the tori. (**A**) Detail of a 1400 atom torus, which shows diamagnetic (counter-clockwise) currents. (**B**) Detail of a 1500 atom torus, which shows paramagnetic (clockwise) currents. The currents are normalized for each case and the size of the arrows is proportional to the current magnitude.

torus (Fig. 2.19B) the inter-atomic currents are three orders of magnitude larger, with values of $\sim 2500\ \boldsymbol{i}_b$, and circulate clockwise.

2.8 Corrugated nanotori (heptagonal and octagonal rings)

In this section, the magnetic response of corrugated nanotori (see section 2.3.3), subjected to a magnetic field perpendicular to the plane of the tori is analyzed. The tori are formed from coalesced C_{60} molecules along the 2-, 3-, and 5-fold axis of symmetry. As for carbon nanotori constructed from SWNTs, an induced magnetic moment $\mu = \boldsymbol{i}_t \sigma$ can be estimated for these structures. Throughout this section we used the notation introduced in section 2.6 to name polymerized fullerenes. Thus, a torus formed from polymerized C_{60} units along the 2-, 3- or 5-fold axis of symmetry will be named as torus C_{60}-C2(8), C_{60}-C3(7) or C_{60}-C5(8), respectively. We found that for the three types of corrugated tori the magnetic response is different.

The following calculations were performed for an applied magnetic field of 1 kGs (0.1 T); although a systematic study up to 10 kGs was realized, no important variation in the magnetic response was found. Table 2.4 shows the induced maximum inter-atomic currents ($\boldsymbol{i}_{ij}^{max}$) for different sizes of the three types of corrugated nanotori. From the data of Table 2.4 it is already clear that the magnetic response strongly depends on the symmetry of the tori, since $\boldsymbol{i}_{ij}^{max}$ current values show im-

Table 2.4: Maximum inter-atomic currents i_{ij}^{max} in units of benzene current i_b for corrugated nanotori constructed by coalescing C_{60} molecules along the 2-, 3-, and 5-fold axis of symmetry with different number of atoms. The external magnetic field (H= 1 kGs) is applied perpendicular to the tori plane.

tori C_{60}-C2(8)		tori C_{60}-C3(7)		tori C_{60}-C5(8)	
# atoms	i_{ij}^{max}	# atoms	i_{ij}^{max}	# atoms	i_{ij}^{max}
616	11.37	840	5530	700	4380
672	11.12	900	0.68	800	3485
728	10.98	960	4333	900	3586
784	10.94	1020	0.70	1000	3148
840	10.98	1080	4128	1100	2622
896	11.12	1140	0.73	1200	2660
952	11.32	1200	2510	1300	2565
1008	11.60	1260	0.73	1400	2194
1064	11.97	1320	1895	1500	2028
1120	12.43	1380	0.74	1600	2007
1176	13.01	1440	1469	1700	1921
1232	13.73	1500	0.74	1800	1770
1288	14.63	1560	1577	1900	1678
1344	15.74	1620	0.75	2000	1650
1400	17.11	1680	1377	2100	1541
1456	18.92			2200	1430
1512	21.39			2300	1390
1568	24.87				
1624	30.16				
1680	39.23				

portant differences in strength. Furthermore, the presence of 5MR, 7MR and 8MR besides 6MR in these tori causes the formation of unique ring current patterns. In the following sections, a detailed explanation of the induced magnetic moments and ring current patterns for each one of the corrugated carbon nanotori is presented.
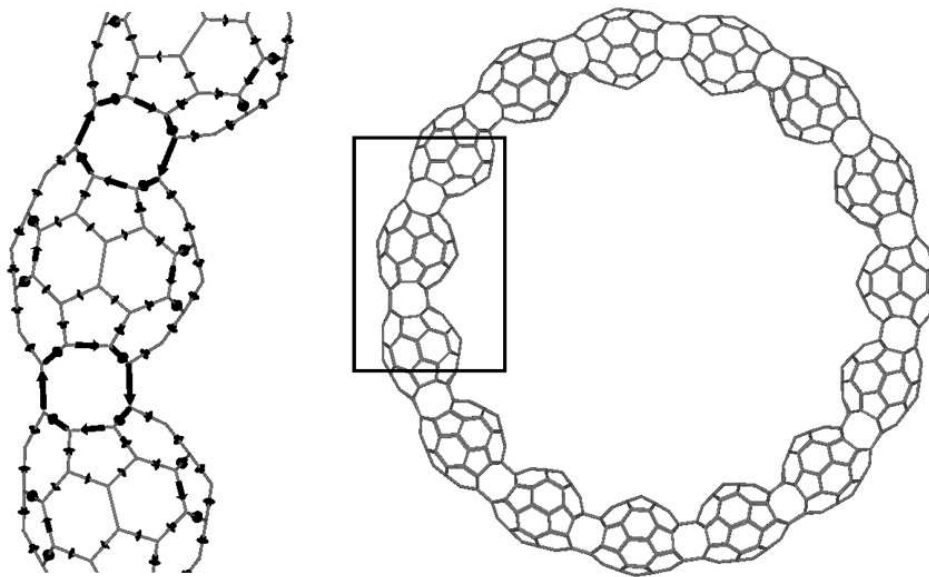
Figure 2.20: Ring current pattern detail in a 840 atom C_{60}-C2(8) torus. The pattern (left) corresponds to the marked area of the complete torus (right). Because of symmetry, this pattern repeats throughout the torus. Arrows represent $\boldsymbol{i}_{ij}$ currents and the length of the arrows is proportional to the normalized current intensity. The applied magnetic field points towards the page.

2.8.1   Tori C_{60}-C2(8)

Corrugated nanotori formed from coalesced C_{60} molecules along the 2-fold axis of symmetry exhibit ring currents ten times higher than that of benzene. For example, the 952 atom torus C_{60}-C2(8) has a value of 11.3 $\boldsymbol{i}_b$ for the maximum inter-atomic current. Even larger $\boldsymbol{i}_{ij}$ values are obtained for tori with more than ~ 1500 atoms (see Table 2.4). However, for all these tori, regardless of the size, the magnetic moment is zero. This occurs because a cancellation effect between the ring currents takes place, as can be seen in Fig. 2.20. The ring current pattern in the 840 atom torus shows that in the C_{60}'s unions of four bonds (only two shown), formed by four 8MR, the ring currents farthest away from the torus center are opposite in direction and have the same magnitude as the interior rim currents, adding to a total current $\boldsymbol{i}_t = 0$, and in consequence the torus has a magnetic moment $\mu = 0$. The cancellation mechanism resembles the one that occurs in C_{60} by which its low magnetic susceptibility is explained [8].

Figure 2.21: Ring current patterns for two distinct C_{60}-C3(7) tori. (**A**) A 840 atom torus, for which the i_{ij} create disconnected loops. (**B**) A 900 atom torus, with a more complex ring current pattern. Arrows represent i_{ij} currents and the length of the arrows is proportional to the normalized current intensity. The applied magnetic field points towards the page.
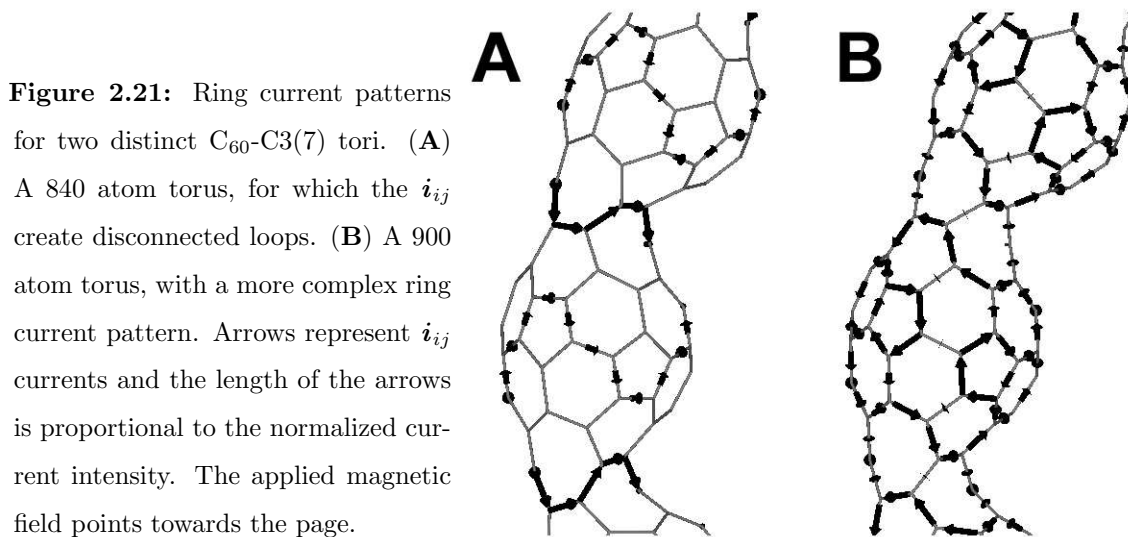
2.8.2   Tori C_{60}-C3(7)

A torus C_{60}-C3(7) is formed from C_{60} molecules covalently connected along the 3-fold axis of symmetry. For these structures two distinguishable responses to the applied magnetic field exist, depending on the size of the torus. If the torus is constructed with an even number of C_{60} units (e.g. 840 atom torus C_{60}-C3(7)), then it will possess large ring currents, three orders of magnitude larger than that of benzene. For tori constructed with an odd number of C_{60} units (e.g. 900 atom torus C_{60}-C3(7)) the ring currents are $\sim i_b$. It can be seen in Table 2.4 that for both behaviors there is a trend for enlarged tori: large currents (even units) start to drop and small currents (odd units) start to rise. The difference in current strength is reflected in the induced current patterns formed in these structures. Figure 2.21 shows the dual magnetic response observed for these tori, contrary to the C_{60}-C2(8) tori that have the same current pattern regardless of the size.

For the C_{60}-C3(7) tori that exhibit large inter-atomic currents, independent circuits are induced in planes parallel to the applied field exactly at bonds that act as 7MR junctions at the torus necks, and also in the middle section of the C_{60} units (Fig. 2.21A). Moreover, no current flows at all in the majority of the bonds. It is clear in this case that the circuit around the torus is open ($i_t = 0$), thus the magnetic moment is zero. In C_{60}-C3(7) tori that exhibit inter-atomic currents $\sim i_b$, a more complex current pattern is induced (Fig. 2.21B). However, a cancellation effect takes

place giving a net magnetic moment of zero.

In summary, for all C_{60}-C3(7) tori there is no magnetic moment induced, although the inter-atomic currents strength depends on the number of C_{60} units needed to form the tori.

2.8.3 Tori C_{60}-C5(8)

All corrugated nanotori formed from coalesced C_{60} molecules along the 5-fold axis of symmetry exhibit strong paramagnetic moments, in striking difference with C_{60}-C2(8) and C_{60}-C3(7) tori. Figure 2.22 shows the magnetic moment as a function of tori size. Although all tori possess paramagnetic moments, for some, the response is stronger on a per carbon atom basis (peaks in Fig. 2.22). For example, the magnetic moments for the 800 and 900 atom C_{60}-C5(8) tori are 10.8 μ_{B} and 25.8 μ_{B}, respectively, which gives a difference of $\sim 50\%$ for the magnitude of the paramagnetic moment per atom. Nevertheless, the induced paramagnetic moment for both cases is two orders of magnitude stronger than the diamagnetic moment of graphite (in absolute value) under the same conditions. Graphite has a value of -30×10^{-3} emu/g along the c axis for the magnetic moment [36]. In the same units, the moments for the 800 and 900 atom tori are 6 and 13 emu/g, respectively.

The large paramagnetic moments are a consequence of the induced currents, which are three orders of magnitude higher than that of benzene (see Table 2.4).
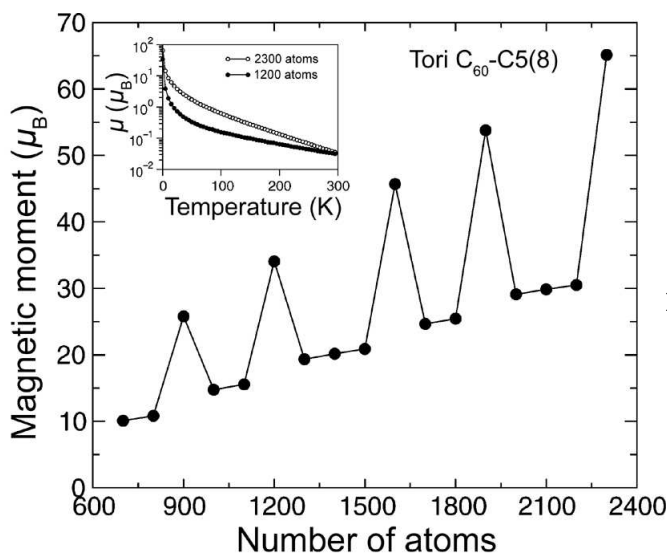
Figure 2.22: Magnetic moment of tori C_{60}-C5(8) as a function of torus size (number of atoms). Inset reveals the temperature dependence of the magnetic moment for tori containing 1000 and 2300 atoms.

Figure 2.23: Ring current patterns for two distinct C$_{60}$-C5(8) tori of (**A**) 800 and (**B**) 900 atoms. For both cases the i_{ij} have a general clockwise (paramagnetic) flow. The flow is stronger for the 900 atom torus since no currents are induced in bonds radial to the torus axis. The applied magnetic field points towards the page.
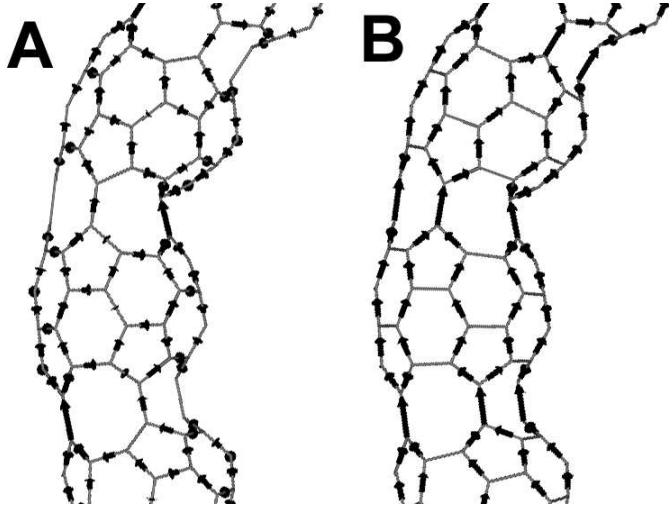
The appearance of peaks for the magnetic moment in Fig. 2.22 can be explained from the ring current patterns shown in Fig. 2.23. For the 800 atom C$_{60}$-C5(8) torus some of the i_{ij} currents flow radially to the toru axis, contributing nothing to the total current (Fig. 2.23A). In contrast, for the 900 atom C$_{60}$-C5(8) torus all of the i_{ij} currents flow tangentially to the radius of the torus (Fig. 2.23B), thus, all contribute to the total current i_t, which is used to calculate the magnetic moment.

The inset of Fig. 2.22 shows the temperature dependence of the magnetic moment. This estimation is possible by introducing a Fermi function term in the the inter-atomic currents expression (Eq. 2.10) [27]. For temperatures as low as 10 K, an important reduction of the magnetic moment is observed. For example, we find that the paramagnetic moment goes from 65.1 μ_B at zero temperature to 1.9 μ_B at 10 K for the 2300 atom C$_{60}$-C5(8) torus.

2.9   Doped carbon nanotori

The doping of carbon nanostructures could be used to modify, with precise control, their chemical and physical properties. For example, recently it has been demonstrated that nanosized diamond exposed to nitrogen (^{15}N) implantation exhibits ferromagnetism [38], an unexpected result for non-magnetic elements. The incorporation of non-metallic atoms, such as B or N, in carbon nanostructures should, to a first approximation, reduce or increase the electronic density. In this context, we study the magnetic properties of non-corrugated and corrugated nanotori doped
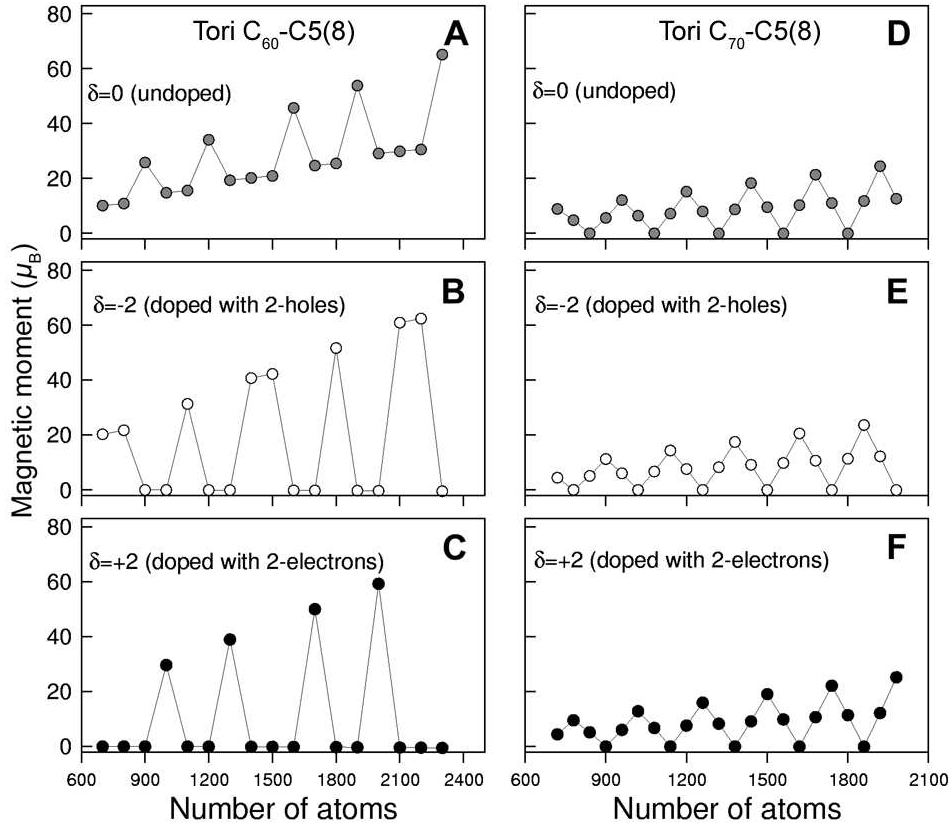
Figure 2.24: Magnetic moment for tori obtained by coalescing C_{60} and C_{70} molecules along the 5-fold axis of symmetry. Graphs (**A**), (**B**) and (**C**) correspond to C_{60}-C5(8) tori; graphs (**D**), (**E**) and (**F**) correspond to C_{70}-C5(8) tori. Results show the magnetic moment as a function of tori size, for the undoped case ($\delta = 0$), systems with two holes ($\delta = -2$) and systems with two additional electrons ($\delta = 2$). The smallest values for the magnetic moment are not zero, but negative (-1.0 to $-0.1\mu_B$).

with different ratios of extra electrons or holes in order to simulate the effects of π-electron charge transfer. In particular, we estimate the induced magnetic moment ($\mu = i_t\sigma$) in tori when a magnetic field of 1 kGs (0.1 T) is applied perpendicular to the plane of the tori. The carbon nanotori analyzed in this section include tori formed from SWNTs (see section 2.7), corrugated nanotori obtained by coalescing C_{60} molecules along the 5-fold axis of symmetry (torus C_{60}-C5(8), see section 2.8) and nanotori obtained by coalescing C_{70} molecules along their principal axis (torus C_{70}-C5(8)).

Figure 2.24 shows the induced magnetic moments in C_{60}-C5(8) and C_{70}-C5(8) tori for the undoped case ($\delta = 0$) and for structures doped with two holes ($\delta = -2$)

or two electrons ($\delta = 2$). The sole addition of two electrons or holes to the tori not only enhances or decreases the magnitude of the magnetic moment, but can make its direction change (Figs. 2.24B, C, E and F). For example, the 1200 atom C_{60}-C5(8) undoped torus has a magnetic moment $\mu = 34 \, \mu_B$, and after doping the torus with two electrons or holes, the magnetic moment drops to $\sim -10^{-2} \, \mu_B$. In contrast, the magnetic moment of the 1800 atom C_{60}-C5(8) torus increases from 26 to 52 μ_B, by doping the structure with two holes.

In order to understand the different doping effects presented in Fig. 2.24, we analyzed the electronic configuration of the π-electrons of the tori at the highest occupied molecular orbital (HOMO). Figure 2.25 shows a schematic representation of the electron occupation at the HOMO energy level for undoped C_{60}-C5(8) and C_{70}-C5(8) tori. Interestingly, the electron occupation of the HOMO for all the C_{60}-C5(8) tori fits one of three cases (Figs. 2.25A-C). In the same manner, the electron configuration of the HOMO of all the C_{70}-C5(8) tori can be divided into four cases (Figs. 2.25D-G). A correspondence between these different HOMO occupation schemes and the induced magnetic moments in the undoped tori (Figs. 2.24A and D) can be derived. The highest magnetic moments per carbon atom attainable in the undoped corrugated tori (peaks in Figs. 2.24A and D) correspond to half-filled occupations of the HOMO level (Figs. 2.25C and F). The systems with a closed electronic shell exhibit diamagnetic behavior. Such is the case of the C_{70}-C5(8) tori grouped in Fig. 2.25D. Since none of the undoped C_{60}-C5(8) tori has an electronic closed shell configuration, all of them have paramagnetic moments, with different
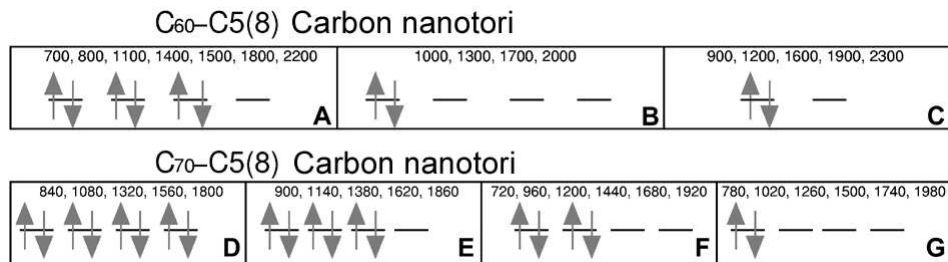
Figure 2.25: Schematic representation of the electron occupation of the HOMO energy level for undoped (**A**- **C**) C_{60}-C5(8) and (**D**- **G**) C_{70}-C5(8) tori. Each tori is assigned to its corresponding HOMO filling scheme by the number of atoms that it contains.

degrees of strength (see Fig. 2.24A). Tori that do not have half-filled HOMO or closed shell electronic configurations (Figs. 2.25A, B, E and G) show paramagnetic moments lower than those present in structures with half-filled HOMO. The effect of doping the systems with two electrons or holes can be deduced from these observations. Any doping that causes a closed shell configuration will diminish the magnetic moment. For example, by doping with two electrons any torus grouped in Figs. 2.25A, C and E will now have a closed shell configuration, and thereby a diminution of the magnetic moment. This effect is clearly observed in Figs. 2.24C and F for the corresponding tori (e.g. 800 atom C_{60}-C5(8) tori). Similarly, any doping that leads to a half-filled HOMO will increase the magnetic moment. One way to do this is to dope any torus grouped in Figs. 2.25B and G with two electrons. Again, the effect is corroborated in Figs. 2.24C and F (e.g. 1020 atom C_{70}-C5(8) tori). It is important to note that the amount of dopant when adding two holes or electrons to the tori is very low ($< 1\%$). This demonstrates that the magnetic properties of these kinds of carbon nanostructures are highly sensitive to doping effects.

Figure 2.26 shows the magnetic moment as a function of the π-electron concentration for four representative corrugated nanotori. When the value of π-electrons per atom is equal to one the system is undoped (circles on the vertical dashed line). The response of these tori is not symmetric with respect to hole or electron doping (left and right in Fig. 2.26, respectively). The 1120 atom C_{60}-C2(8) torus has a diamagnetic moment of -0.1 μ_B in the undoped state. Large paramagnetic moments could be induced for specific hole or electron concentrations. For example, four additional electrons (0.35% of electron concentration) or holes (0.35% of hole concentration) raise the magnetic moment up to ~ 10 μ_B. But by adding six extra electrons (0.54% of electron concentration) or holes (0.54% of hole concentration) the magnetic moment drops again to -0.1 μ_B. Similar results are found for the 840 atom C_{60}-C3(7) torus, which has an almost zero magnetic moment in the undoped state. The 1000 atom C_{60}-C3(7) torus has a large paramagnetic moment in the undoped state ($\mu = 15$ μ_B). The moment drops to almost zero if the structure is doped with two holes (0.20 % hole concentration). In contrast, the addition of two elec-
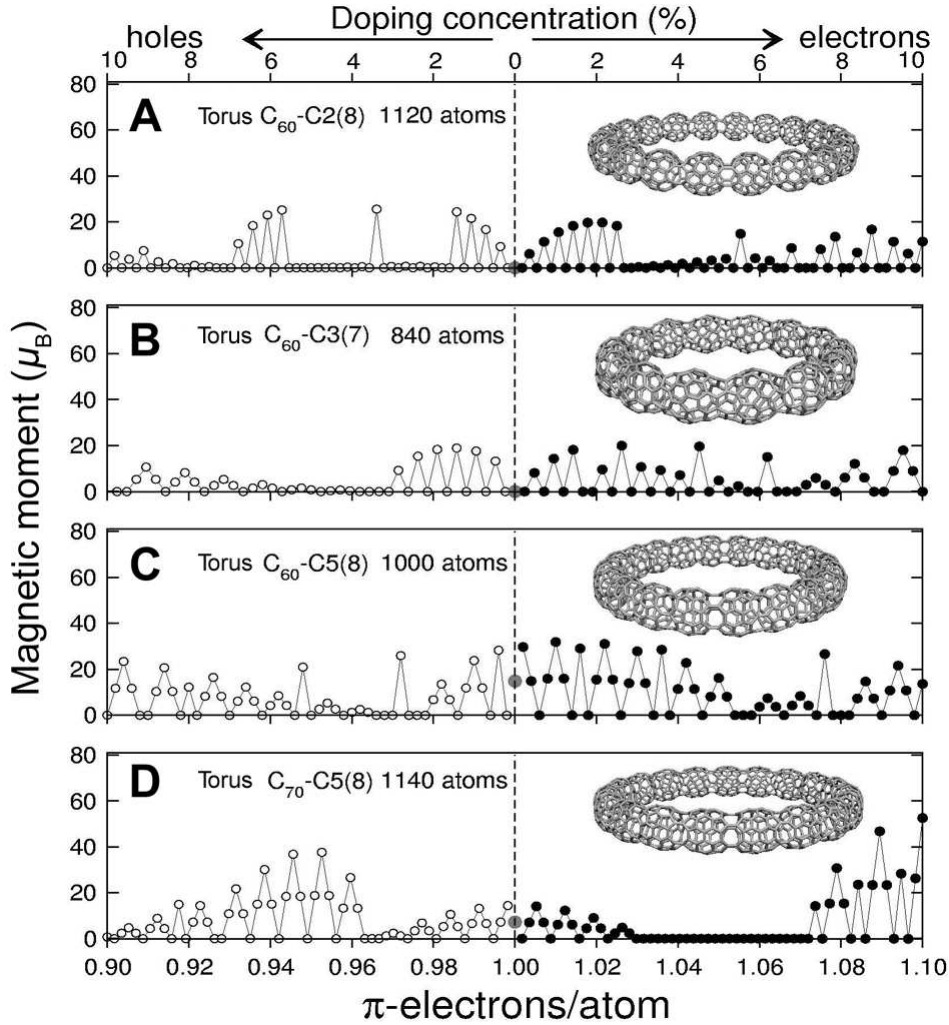
Figure 2.26: Magnetic moment as a function of the doping concentration (number of π-electrons per atom) in (**A**) C_{60}-C2(8), (**B**) C_{60}-C3(7), (**C**) C_{60}-C5(8) and (**D**) C_{70}-C5(8) corrugated nanotori. The undoped systems ($\delta = 0$) are those for which π-electron per atom is equal to one (circles on the vertical dashed line). The white (black) circles correspond to doping with holes (electrons). The holes or electrons are added progressively in pairs (2, 4, 6, etc.).

trons (0.20 % electron concentration) favors an increase in the magnetic moment to 30 μ_B. A magnetic moment enhancement in this torus is clearly favored by electron doping (Fig. 2.26C, right), where a lot of states give high magnetic moments, in contrast to hole doping (Fig. 2.26C, left), for which the majority of states give small magnetic moments values. A more symmetric response for doping is observed in the 1% doping concentration region for the 1140 atom C_{70}-C5(8) torus (Fig. 2.26D). This occurs because as the ratio of hexagons in the lattice is raised, the density
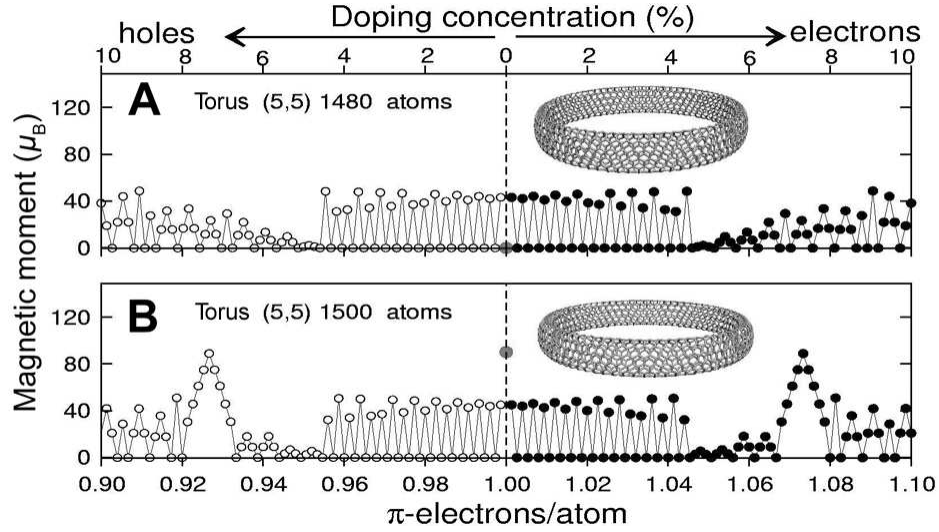
Figure 2.27: Magnetic moment as a function of the doping concentration (number of π-electrons per atom) in carbon nanori formed from a (5,5) SWNT. (**A**) 1480 and (**B**) 1500 atom nanotori. The undoped systems ($\delta = 0$) are those for which π-electron per atom is equal to one (circles on the vertical dashed line). The white (black) circles correspond to doping with holes (electrons). The holes or electrons are added progressively in pairs (2, 4, 6, etc.).

of states becomes more graphite-like, and π-electrons have a symmetric density of states. Figure 2.27 shows the magnetic moment as a function of the π-electron concentration per atom for (5,5) SWNT tori containing 1480 and 1500 atoms. This type of tori present a symmetric response to electron or hole doping. The undoped (vertical dashed line in Fig. 2.27) 1480 and 1500 atom tori show magnetic moments of -0.1 and $90\mu_B$, respectively, as reported by Liu *et al* [27]. Moreover, for definite concentrations of electrons or holes, magnetic moments as high as 40-90 μ_B could be induced.

These results revealed that a small fraction of additional electrons or holes (0.02-4%) is able to strongly alter the magnetic response of carbon nanotori. Charge transfers of this order could be experimentally possible since, for example, the addition of exohedral or endohedral alkali atoms to carbon nanostructures has been achieved.

2.10   Topologically complex carbon nanostructu-res

The discovery of fullerenes [5] and carbon nanotubes [39] proved that curved sp^2 bonded carbon nanostructures could escape from the planar geometry of graphite. In a sense, curvature increases the complexity of a system, and thereby its functionality. Carbon nanotubes contain only 6MR and have zero Gaussian curvature, and the C_{60}
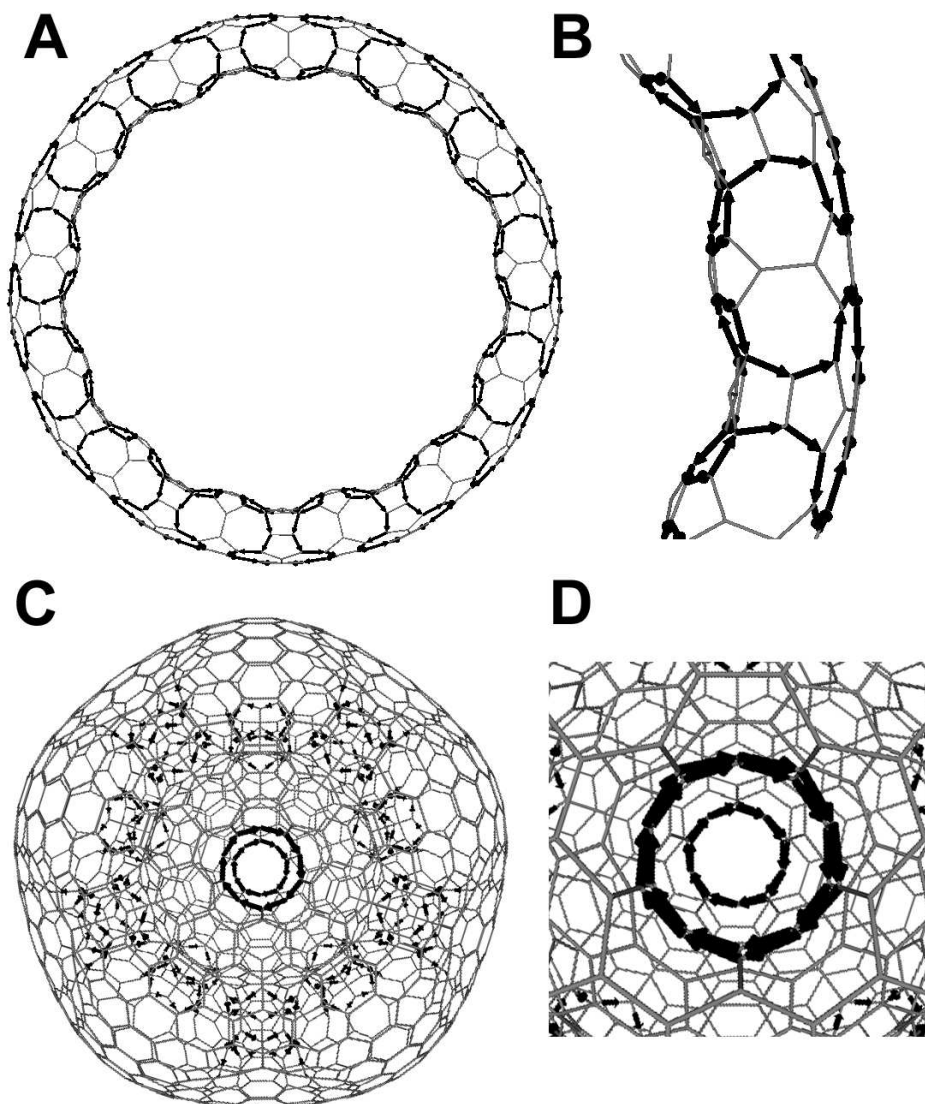
Figure 2.28: Ring current patterns in a (**A** and **B**) Haeckelite torus, which contains only 5MR and 7MR, and (**C** and **D**) a carbon holey-ball, which contains only 6MR and 7MR. Details of **A** and **C** are given in **B** and **D**, respectively.

molecule contains 5MR in addition to 6MR and has positive Gaussian curvature. Ever greater complexity can be introduced in carbon nanostructures if polygons with more than 6 sides are introduced (negative Gaussian curvature). In this context, Fig. 2.28 shows the ring current paths induced when a magnetic field is applied to a Haeckelite torus containing only 5MR and 7MR (Figs. 2.28A and B) [29], and a carbon "holey-ball", which contains only 6MR and 7MR (Figs. 2.28A and B) [40, 41]. For the torus, the induced currents flow in individual loops in planes parallel to the field (Fig. 2.28B) since the field is applied perpendicular to the plane of the torus. Moreover, the strength of the inter-atomic currents is of $\sim 10^3$ $\boldsymbol{i}_b$, three orders of magnitude larger than the induced currents in benzene. This behavior is never observed for carbon nanotori containing only 6MR (see section 2.7). Carbon holey-balls consist of interconnected fullerenes, through negative curvature. The depicted holey-ball has 1320 atoms and 12 holes. Interestingly, the induced currents are confined to these holes (Fig. 2.28D), which could serve as selectivity regions for foreign molecules. Furthermore, the currents' strength are $\sim 10^3$ $\boldsymbol{i}_b$ and generate a paramagnetic moment.

These two examples show that interesting properties could be found in complex carbon nanostructures. Experimentally, it has been shown that it is possible to induce curvature in carbon nanostructures by electron irradiation in non-equilibrium conditions [42], but more research is necessary in order to actually synthesize them.

2.11   Conclusions

The magnetic response of π-electrons in sp^2 bonded carbon nanostructures that, through the incorporation of polygons other than hexagons in the atomic lattice, present local positive or negative Gaussian curvature, was investigated.

In particular, it was demonstrated that polymerized fullerenes formed by coalescing C_{60} and C_{70} molecules along their axes of symmetry could exhibit either diamagnetism or paramagnetism depending on the specific symmetry of coalescence and the size of the structure. Paramagnetic polymerized fullerenes could reach values up to ~ 200 CGS p.p.m per mol C for the ring current magnetic susceptibility,

which is more than the total magnetic susceptibility of graphite (-97 CGS p.p.m per mol C) in absolute value.

In addition, it was found that corrugated nanotori formed from coalesced C_{60} molecules along the 2-, 3-, and 5-fold axis of symmetry, exhibit unique induced ring current patterns that depend on the existence of 8 and 7 membered rings in these structures. Large paramagnetic moments of ~ 10 emu/g could be induced in corrugated nanotori formed from coalesced C_{60} molecules along the 5-fold axis of symmetry, with an applied magnetic field perpendicular to the tori plane of 1 kGs at low temperatures. The paramagnetic response of these structures does not depend on the size of the tori, as opposed to carbon nanotori created from SWNT segments that contain only hexagonal rings.

The magnetic moments induced in carbon nanotori depend on the electron occupation of the HOMO level. Carbon nanotori with a half-filled HOMO display the largest paramagnetic moments, and systems with an electronic closed shell configuration show relatively small diamagnetic moments. Thus, by precise doping of electrons or holes, the electron occupation of the HOMO level in sp^2 carbon nanostructures could be modified to produce large paramagnetic moments (~ 10 emu/g).

In conclusion, it was found that sp^2 carbon nanostructures that contain polygons other than hexagons could show strong paramagnetic behavior, in contrast to graphite and aromatic molecules which are diamagnetic. Moreover, this effect is a consequence of the geometrical configurations of the non-magnetic carbon atoms.

References

[1] R. C. Haddon. Magnetism of the carbon allotropes. *Nature*, 378:249–255, 1995.

[2] P. Esquinazi and R. Höhne. Magnetism in carbon structures. *J. Magn. Magn. Mater.*, 290-291:20–27, 2005.

[3] L. Pauling. The diamagnetic anisotropy of aromatic molecules. *J. Chem. Phys.*, 4:673–677, 1936.

[4] K. Lonsdale. Magnetic anisotropy and electronic structure of aromatic molecules. *Proc. R. Soc. A*, 159:149–161, 1937.

[5] H. W. Kroto, J. R. Heath, S. C. O'Brien, R. F. Curl, and R. E. Smalley. C_{60}: Buckminsterfullerene. *Nature*, 318:162–163, 1985.

[6] V Elser and R. C. Haddon. Icosahedral C_{60}: an aromatic molecule with a vanishingly small ring current magnetic susceptibility. *Nature*, 325:792–794, 1987.

[7] R. C. Haddon, L. F. Schneemeyer, J. V. Waszczak, S. H. Glarum, R. Tycko, G. Dabbagh, A. R. Kortan, A. J. Muller, A. M. Mujsce, M. J. Rosseinsky, S. M. Zahurak, A. V. Makhija, F. A. Thiel, K. Raghavachari, E. Cockayne, and V. Elser. Experimental and theoretical determination of the magnetic susceptibility of C_{60} and C_{70}. *Nature*, 350:46–47, 1991.

[8] A. Pasquarello, M. Schlüter, and R. C. Haddon. Ring currents in icosahedral C_{60}. *Science*, 257:1660–1661, 1992.

[9] A. P. Ramirez, R. C. Haddon, O. Zhou, R. M. Fleming, J. Zhang, S. M. Mc-Clure, and R. E. Smalley. Magnetic susceptibility of molecular carbon: nanotubes and fullerite. *Science*, 265:84–86, 1994.

[10] J. P. Lu. Novel magnetic properties of carbon nanotubes. *Phys. Rev. Lett.*, 74:1123–1126, 1995.

[11] M. Núñez Regueiro, L. Marques, J-L. Hodeau, O. Béthoux, and M. Perroux. Polymerized fullerite structures. *Phys. Rev. Lett.*, 74:278–281, 1995.

[12] T. L. Makarova, B. Sundqvist, R. Höhne, P. Esquinazi, Y. Kopelevich, P. Scharff, V. A. Davydov, L. S. Kashevarova, and A. V. Rakhmanina. Magnetic carbon. *Nature*, 413:716–718, 2001.

[13] A. V. Rode, S. T. Hyde, E. G. Gamaly, R. G. Elliman, D. R. McKenzie, and S. Bulcock. Structural analysis of a carbon foam formed by high pulse-rate laser ablation. *Appl. Phys. A: Mater. Sci. Process.*, A69:S755, 1999.

[14] A. V. Rode, E. G. Gamaly, A. G. Christy, J. G. Fitz Gerald, S. T. Hyde, R. G. Elliman, B. Luther-Davies, A. I. Veinger, J. Androulakis, and J. Giapintzakis. Unconventional magnetism in all-carbon nanofoam. *Phys. Rev. B*, 70:54407, 2004.

[15] A. L. Mackay and H. Terrones. Diamond from graphite. *Nature*, 352:762, 1991.

[16] B. W. Smith, M. Monthioux, and D. E. Luzzi. Encapsulated C_{60} in carbon nanotubes. *Nature*, 396:323–324, 1998.

[17] B. W. Smith, R. M. Russo, S. B. Chikkannanavar, F. Stercel, and D. E. Luzzi. Reproducible synthesis of C_{60}@swnt in 90% yields. *Mat. Res. Soc. Symp. Proc.*, 706:Z3.13.1, 2002.

[18] S. Bandow, K. Hirahara, T. Hiraoka, G. Chen, P. C. Eklund, and S. Iijima. Turning peapods into double-walled carbon canotubes. *MRS Bulletin*, 29(4):260–264, 2004.

[19] E. Hernández, V. Meunier, B. W. Smith, R. Rurali, H. Terrones, M. Buongiorno Nardelli, M. Terrones, D. E. Luzzi, and J.-C. Charlier. Fullerene coalescence in nanopeapods: a path to novel tubular carbon. *Nano Lett.*, 3:1037–1042, 2003.

[20] B. I. Dunlap. Connecting carbon tubules. *Phys. Rev. B*, 46:1933–1936, 1992.

[21] S. Itoh, S. Ihara, and J. Kitakami. Toroidal form of carbon C_{360}. *Phys. Rev. B*, 47:1703–1704, 1993.

[22] J. Liu, H. Dai, J. H. Hafner, D. T. Colbert, R. E. Smalley, S. J. Tans, and C. Dekker. Fullerene 'crop circles'. *Nature*, 385:780–781, 1997.

[23] R. Martel, H. R. Shea, and P. Avouris. Rings of single-walled carbon nanotubes. *Nature*, 398:299, 1999.

[24] M. Sano, A. Kamino, J. Okamura, and S. Shinkai. Ring closure of carbon nanotubes. *Science*, 293:1299–1301, 2001.

[25] R. C. Haddon. Electronic properties of carbon toroids. *Nature*, 388:31–32, 1997.

[26] V. Meunier, Ph. Lambin, and A. A. Lucas. Atomic and electronic structures of large and small carbon tori. *Phys. Rev. B*, 57:14886–14890, 1998.

[27] L. Liu, G. Y. Guo, C. S. Jayanthi, and S. Y. Wu. Colossal paramagnetic moments in metallic carbon nanotori. *Phys. Rev. Lett.*, 88:217206, 2002.

[28] H. Terrones, M. Terrones, F. López-Urías, J. A. Rodríguez-Manzo, and A. L. Mackay. Shape and complexity at the atomic scale: the case of layered materials. *Philos. Trans. R. Soc. A*, 362:2039–2063, 2004.

[29] H. Terrones, M. Terrones, E. Hernández, N. Grobert, and J-C. & P. M. Ajayan. Charlier. New metallic allotropes of planar and tubular carbon. *Phys. Rev. Lett.*, 84:1716–1719, 2000.

[30] F. London. Théorie quantique des courants interatomiques dans les combinaisons aromatiques. *J. Phys. Rad.*, 8:397–409, 1937.

[31] A. Pasquarello, M. Schlüter, and R. C. Haddon. Ring currents in topologically complex molecules: application to C_{60}, C_{70}, and their hexa-anions. *Phys. Rev. A*, 47:1783–1789, 1993.

[32] V. Elser and R. C. Haddon. Magnetic behavior of icosahedral C_{60}. *Phys. Rev. A*, 36:4579–4584, 1987.

[33] R. C. Haddon and A. Pasquarello. Magnetism of carbon clusters. *Phys. Rev. B*, 50:16459–16463, 1994.

[34] P. W. Atkins and R. S. Friedman. *Molecular quantum mechanics*, chapter 13. Oxford university press, 2003.

[35] R. S. Ruoff, D. Beach, J. Cuomo, T. McGuire, R. L. Whetten, and F. Diedrich. Confirmation of a vanishingly small ring-current magnetic susceptibility of icosahedral C_{60}. *J. Phys. Chem.*, 95:3457–3459, 1991.

[36] J. Heremans, C. H. Olk, and D. T. Morelli. Magnetic susceptibility of carbon structures. *Phys. Rev. B*, 49:15122–15126, 1994.

[37] S. Zaric, G. N. Ostojic, J. Kono, J. Shaver, V. C. Moore, M. S. Strano, R. H. Hauge, R. E. Smalley, and X. Wei. Optical signatures of the aharonov-bohm phase in single-walled carbon nanotubes. *Science*, 304:1129 – 1131, 2004.

[38] S. Talapatra, P. G. Ganesan, T. Kim, R. Vajtai, M. Huang, M. Shima, G. Ramanath, D. Srivastava, S. C. Deevi, and P. M. Ajayan. Irradiation-induced magnetism in carbon nanostructures. *Phys. Rev. Lett.*, 95:97201, 2005.

[39] S. Iijima. Helical microtubules of graphitic carbon. *Nature*, 254:56–58, 1991.

[40] H. Terrones and M. Terrones. Curved nanostructured materials. *New J. Phys.*, 5:126, 2003.

[41] H. Terrones and M. Terrones. Quasiperiodic icosahedral graphite sheets and high-genus fullereneswith nonpositive gaussian curvature. *Phys. Rev. B*, 55(9969-9974), 1997.

[42] J. Li and F. Banhart. The engineering of hot carbon nanotubes with a focused electron beam. *Nano Lett.*, 4:1143–1146, 2004.

Chapter 3

Synthesis of different types of carbon nanotubes and analysis of metal inclusions

3.1 Introduction

In this chapter, it is shown that the pyrolysis of aerosolized solutions, where the solvent is the carbon source and the solute is the catalyst precursor, could be used as a method to synthesize different types of carbon nanotubes (CNTs). Single-walled carbon nanotubes (SWNTs), multi-walled carbon nanotubes (MWNTs) and nitrogen doped carbon nanotubes (CN_x) are obtained by using ethanol, toluene and benzylamine, respectively, as the carbon source agent. Approximately 3%, by weight, of the MWNTs grown by the pyrolysis of aerosols corresponds to encapsulated catalyst particles within the MWNTs' cores, trapped as a side effect in the reaction. Different metals can be encapsulated by varying the type of catalyst precursor used in the solution to be aerosolized. Specifically, we have used different metallocenes as catalyst precursors and characterized MWNTs encapsulating Fe, Co, Ni and a FeCo alloy.

In addition, a brief review on the different techniques used to produce CNTs is presented, emphasizing the chemical vapor deposition process since the pyrolysis of aerosols is a variation of this technique.

3.2   Carbon nanotube growth methods

Different experimental methods have proven useful to obtain CNTs. The schemes
for the three most commonly used nowadays: arc-discharge, laser ablation and chem-
ical vapor deposition (CVD) [1], are shown in Fig. 3.1. In the arc-discharge method,
a large current is passed through a small gap between two graphite electrodes, in
an inert gas atmosphere under controlled pressure (Fig. 3.1A). When direct cur-
rent is used, carbon evaporates from the anode and re-condenses at the cathode
rod creating a hard cylindrical deposit, which contains CNTs [2]. A breakthrough
in this technique occurred when Ebbesen and Ajayan produced gram quantities of
MWNTs. They found out that by applying 100 A between the electrodes in a helium
atmosphere at a pressure of 500 Torr, MWNTs deposited on the cathode in gram
quantities [3]. SWNTs are obtained in the arc-discharge chamber only if a catalyst
is implanted in the anode electrode [4]. In general, CNTs of high quality are pro-
duced with arc-discharge, and as a by-product multi-layered graphitic particles with
polyhedron shapes are obtained.

In the laser ablation method (Fig. 3.1B), a graphite target is held inside an oven
(1200°C) under a controlled inert gas atmosphere. The graphite target is vaporised
with a high energy laser, and a gas flow carries the expelled material out onto a
Cu water-cooled collector, where MWNTs are deposited [5]. As in the arc-discharge
method, a small amount of catalyst needs to be added to the graphite target to
obtain SWNTs [6]. In both of these methods, the growth of CNTs involves the
re-condensation of carbon atoms generated from evaporation of graphite at high
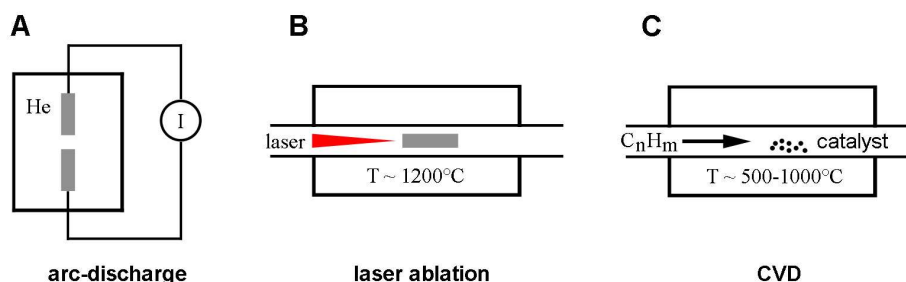
Figure 3.1: (Color) Experimental schemes for CNT growth. (**A**) Arc-discharge. (**B**) Laser
ablation. (**C**) Chemical vapor deposition (CVD).

temperatures.

Chemical vapor deposition (CVD) methods have been used for more than 30 years to produce carbon fiber, filament and nanotube materials [1]. In a CVD experiment a substrate is exposed to volatile precursors that undergo a chemical reaction or decomposition to obtain the desired deposit. The standard CVD experimental setup used to grow CNTs is shown in Fig. 3.1C. In this process, a catalyst is heated at high temperatures (500-1000°C) inside an oven where a hydrocarbon gas is allowed to flow. The reaction of the gas with the active catalyst produces the desired material, which is collected upon cooling the system to room temperature. A variation of the CVD method is powder pyrolysis, where a solid form of carbon is mixed with the catalyst instead of using a hydrocarbon gas as the carbon source. For example, by pyrolysing alternating layers of C_{60} crystals and Ni thin films, needle-like carbon nanotubes are obtained [7]. Moreover, some chemical compounds (e.g. metallocenes) contain both the metal catalyst and the carbon source in a single complex. Thus, by pyrolysing such compounds CNTs could be obtained. By applying this principle, Rao and Sen grew aligned CNT-bundles with ferrocene $(Fe(C_5H_5)_2)$ as the carbon source and catalyst mixed agent [8].

Another alternative of the CVD method consists of the pyrolysis of aerosolized solutions. In this process, the catalyst is dissolved in a solvent which is the carbon source. The solution is then aerosolized and carried with an inert gas flow to a reaction oven where CNT growth takes place [9, 10]. A more detailed explanation of the technique of aerosolized solution pyrolysis is presented in the next section.

3.3   Pyrolysis of aerosolized solutions

The basic parameters involved in the CVD-based pyrolysis of aerosolized solutions include the carbon source solvent, the catalyst-containing solute, and the aerosol generation method. By varying the carbon source solvent, different types of CNTs could be grown. In this process, as a side effect, catalyst wire-shaped particles are encapsulated by the CNTs. Thus, by using different compounds as the solute, different materials could be encapsulated. Clearly, only materials that serve as a

catalyst for CNT growth can be encapsulated with this process.

In this section, we describe the two experimental setups that were used to synthesize different types of CNTs. In essence, the two setups differ in the way that the aerosol is generated prior to pyrolysis. In one process the aerosol is obtained by injecting with pressure the solution through a capillary tube, and we call it: *injection aerosol generator*. In the second approach the aerosol is generated by a vibrating piezoelectric, and it is known as *ultrasonic aerosol generator* [11]. Schematic representations of both methods are given below.

3.3.1   Injection aerosol generator

Figure 3.2 shows the schematic representation of the injection aerosol generator experimental setup. The solution to be pyrolyzed is contained in a round flask that has a gas inlet at the top and a valve at the bottom. This setup permits control of the amount of solution that goes into the capillary tube (diameter 0.5 mm). The bottom part of the flask is fixed to a L-type tube that ends in a nozzle (capillary tube). The nozzle is contained in a pyrex tube which directs the carrier gas flow, producing the aerosol at the tip of the nozzle (Fig. 3.2, inset). The nozzle is adapted to a quart tube (diameter 2 cm) that goes inside a furnace, where the reaction takes place when the solution is aerosolized and the temperature of the furnace is raised.
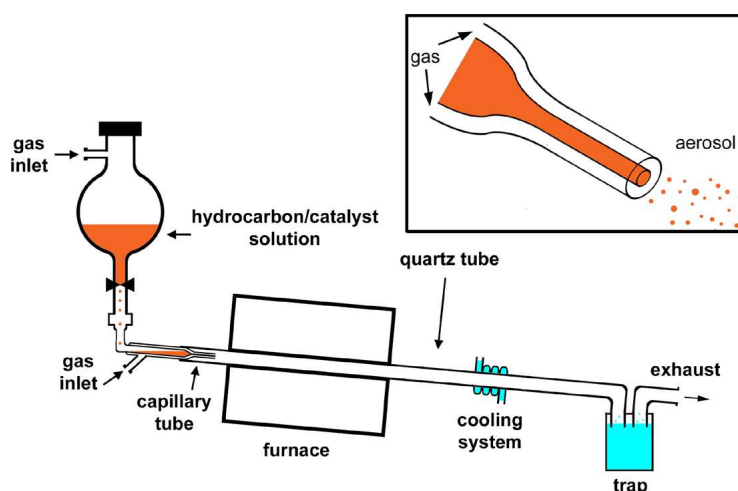
Figure 3.2: (Color) Injection aerosol generator experimental setup. The inset shows the generation of the aerosol at the tip of the capillary tube.

With this method, volumes of solution as low as 5 ml can be used for CNT growth.

3.3.2 Ultrasonic aerosol generator

Figure 3.3 shows a schematic diagram of the ultrasonic aerosol generator experimental setup used for CNT growth [11, 12]. The vase contains the solution to be aerosolized. At the bottom of the vase a piezoelectric ceramic driven by AC current produces the aerosol. The aerosol is then carried by a flow of Ar to the reaction zone inside the furnace. The quartz tube serves as a substrate for CNT growth. This technique offers better control on the production of the aerosol, but the minimum volume required for the solution is ~ 100 ml.
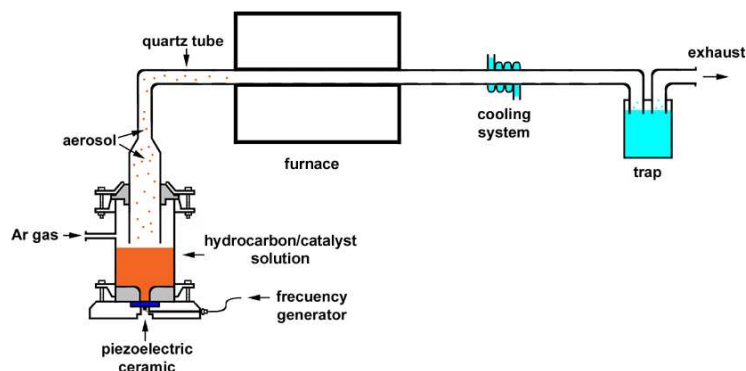
Figure 3.3: (Color) Ultrasonic aerosol generator experimental setup. The piezoelectric piece at the bottom of the vase produced the aerosol.

3.4 Characterization techniques

The synthesized samples were characterized to ascertain structural properties of the CNTs as well as chemical composition in the case of encapsulated materials. Several techniques were used for this purpose. These include: powder X-ray diffraction (XRD), scanning electron microscopy (SEM), transmission electron microscopy (TEM), energy dispersive X-ray spectroscopy (EDX) and thermogravimetric analysis (TGA). For SWNTs, Raman spectroscopy was used in order to estimate the diameters of the tubes.

3.5   Single-walled carbon nanotubes (SWNTs)

SWNTs have been produced with the arc-discharge [13] and laser ablation [14] methods, which require high temperature ($> 3000°C$) to evaporate carbon atoms from solid carbon sources. This limits the scale-up of the process for SWNT growth. To address this problem SWNTs have been grown by the CVD method, that in principle could allow for larger scale synthesis. Various carbon containing molecules such as CO, methane, acetylene, ethylene and benzene in combination with supported catalysts were used for growth [15]. In addition, Maruyama and coworkers synthesized high purity SWNTs by using alcohol as the carbon source [16]. The supporting catalyst approach for CNT growth is a two-step process. In addition, in the majority of these reported works, H_2 is used as a carrier gas, which implies a risk when handling it in the laboratory.

In this section, the production and characterization of cm-long strands consisting of SWNTs ropes produced with the ultrasonic spray generator (see section 3.3.2) is described. Following Maruyama's work [16], we used ethanol as the carbon source. This method is a easy one-step process and does not require relatively high temperatures ($\sim 1200°C$) or H_2.

3.5.1   Experimental conditions

The experiments were carried out with the ultrasonic spray generator (see section 3.3.2). For the solution, ferrocene ($Fe(C_5H_5)_2$ or $FeCp_2$) or a mixture of ferrocene-manganocene ($MnCp_2$) was dissolved in ethanol (250 mL) at concentrations of 0.2, 0.4, 0.6, 0.8, 1.0 and 1.2% weight of metallocene to weight of ethanol (w/w). The solution was aerosolized and transferred to the furnace with a high purity Ar flow ranging from 0.1 to 0.8 L/min. Reaction temperatures were varied from 700 to 950°C, and the reaction time was 30 min, after which the aerosol flow was stopped and the furnace was allowed to cool down to room temperature. After ~ 5 minutes of reaction, black threads could be observed in the quartz tube just outside the furnace. This process continued, and after ~ 20 minutes of reaction, a dark film coating covered completely the quartz tube. Figure 3.4A shows how the black film
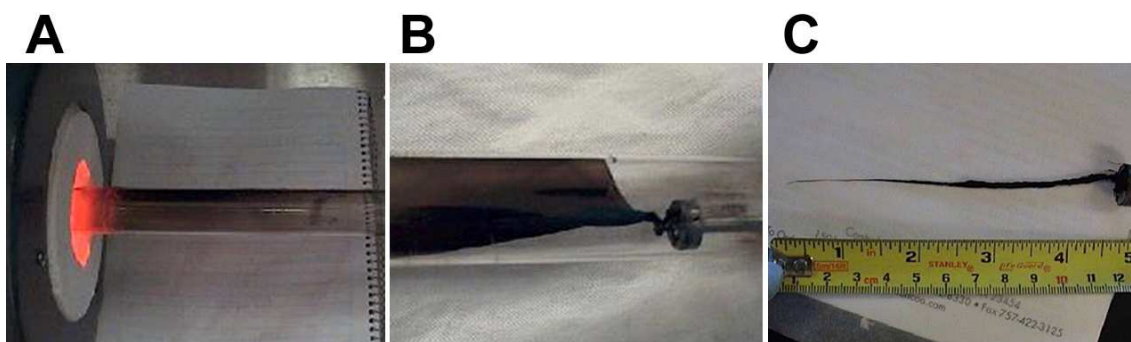
Figure 3.4: (Color) Photographs showing the formation and collection of the SWNT film. (**A**) The SWNTs are deposited outside of the furnace. (**B**) Collection of the SWNT film with a piece of wire. (**C**) Twisted thread of SWNTs after collection. The length of thread is 12 cm [17].

deposited outside of the furnace during the experiment. After the quartz tube reached room temperature the mat-like film was extracted in one single thread with a piece of wire (Fig. 3.4B). Figure 3.4C shows a typical length for the extracted sample ($\sim$ 12 cm). In addition, a hard deposit material was recovered from the hot zone of the oven, which consisted of MWNTs and amorphous carbon material.

3.5.2 SEM and TEM analysis

Figure 3.5 shows the micro-structure of the extracted film at different magnifications. The film consists of SWNT bundles mixed with small diameter catalyst particles (2–20 nm). The entanglement between the bundles makes a coherent sheet that can stand by itself on the TEM grid (Fig. 3.5B). It is hard to find ending sites
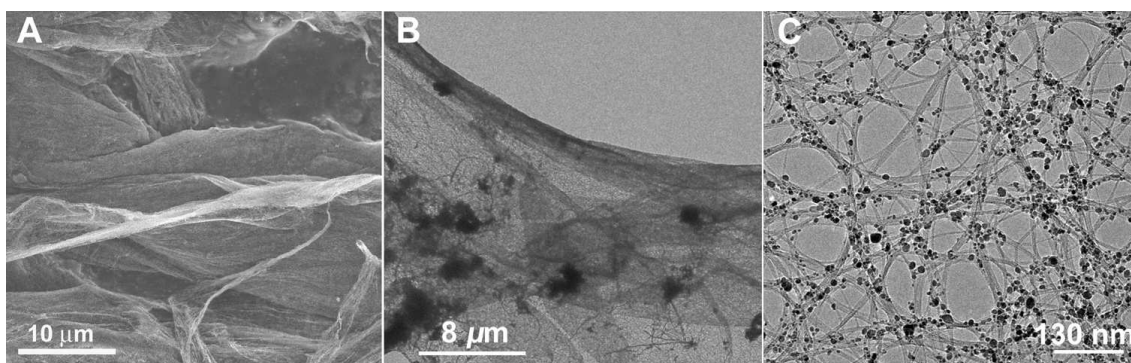
Figure 3.5: (**A**) SEM and (**B** and **C**) low magnification TEM images of the SWNT thread produced with an FeCp$_2$-ethanol solution at 900°C.
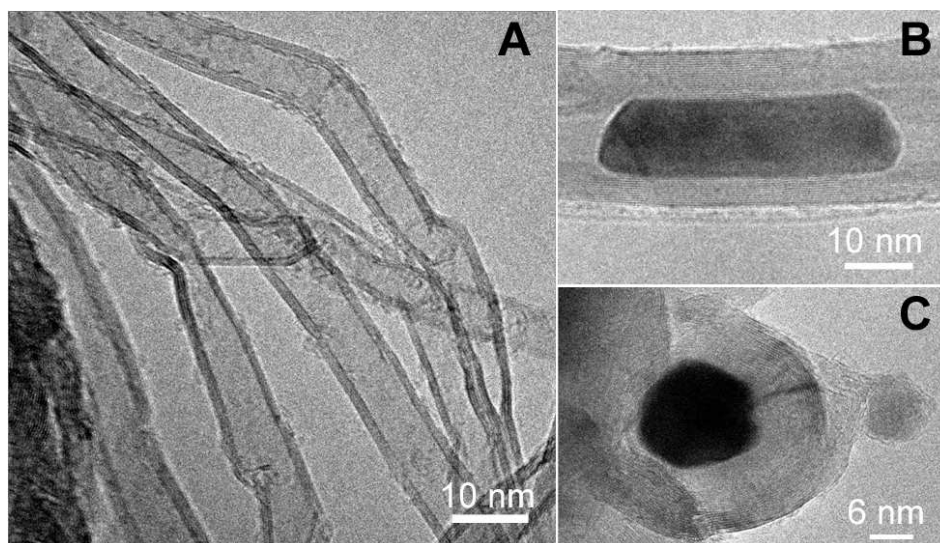
Figure 3.6: TEM images of the material collected in the reaction zone for an experiment with a $FeCp_2$-$MnCp_2$ mixture dissolved in ethanol at 900°C. (**A**) Thin MWNTs; (**B**) particle inside a MWNT core and (**C**) polyhedral particle encapsulating a particle.

for the SWNTs during electron microscopy observations to estimate their lengths. However, the long macroscopic thread is probably formed by smaller entangled pieces of SWNT bundles. In the region inside the oven MWNTs and amorphous material were found. Figure 3.6 shows an example of the type of MWNTs obtained with the $FeCp_2$-$MnCp_2$ mixture at 900°C. The MWNTs outer diameters range from 10 to 35 nm and are thinner than MWNTs produced using different solvents (see section 3.6). Some of the MWNTs present encapsulated material in their cores (Fig. 3.6B). Also, carbon polyhedral particles are observed, and like the MWNTs some present encapsulated material (Fig. 3.6C).

Figure 3.7 shows TEM images of SWNTs collected outside the furnace. For TEM observation, the mat of SWNTs was dispersed in ethanol in a sonication bath for 5 minutes, and a drop of the dispersion was placed onto the TEM grid. The SWNTs are usually in bundles, and some are covered with amorphous carbon. Figure 3.7D shows a clear image of an isolated SWNT with a 2 nm diameter. Contrary to MWNTs found inside the reaction zone, SWNTs never present encapsulated material. All the catalyst particles are found outside the SWNTs.

The highest yield of SWNTs occurred at 950°C when pyrolyzing $FeCp_2$ at a
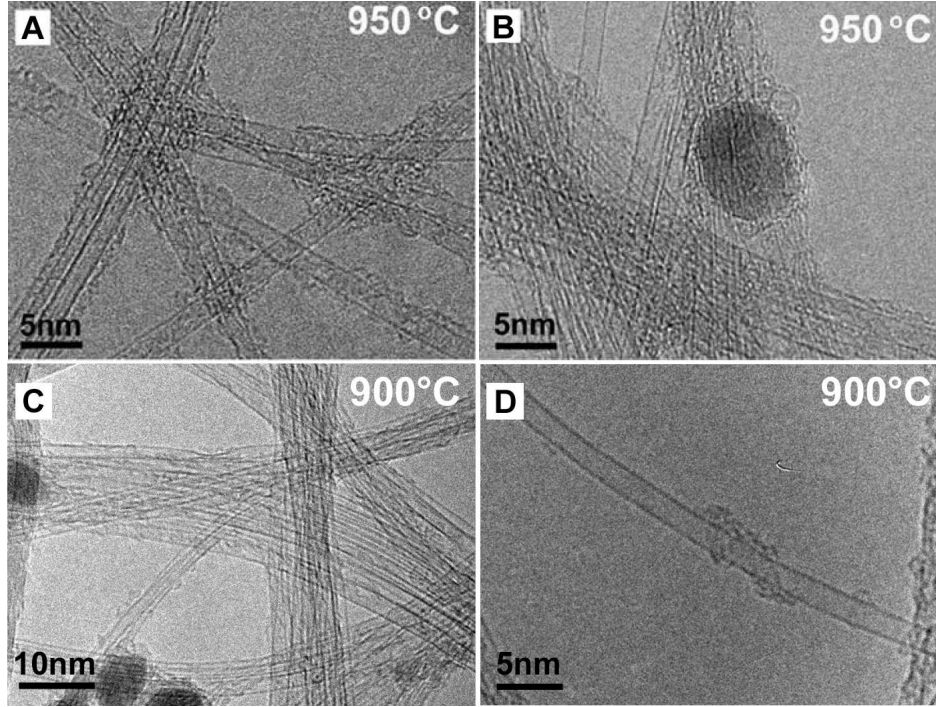
Figure 3.7: TEM images of SWNTs. (**A** and **B**) SWNTs grown at 950°C using a FeCp$_2$ 1.2% (w/w) solution. (**C** and **D**) SWNTs grown at 900°C using a FeCp$_2$-MnCp$_2$ mixture 1.2% (w/w) solution. Some of the SWNTs are covered by amorphous carbon material.

concentration of 1.2% (w/w) in ethanol. In addition, for temperatures lower than 800°C or metallocene concentration below 0.6% (w/w), SWNTs could hardly be obtained.

3.5.3 Raman spectroscopy of SWNTs

For SWNT characterization, the important features in the Raman spectra are the tangential G-band (1550–1605 cm^{-1}), which is derived from the graphite-like in-plane mode; the disorder-induced D-band (~ 1350 cm^{-1}), which helps in estimating the quality of a sample; and the radial breathing mode (RMB) [18]. This last feature is associated with in-phase radial displacements of the SWNTs and is related to each SWNT diameter through

$$d[nm] = 248/\omega_{\mathrm{RMB}}[cm^{-1}] \tag{3.1}$$

where d is the diameter of the SWNT and ω_{RMB} the frequency of the RBM mode. In addition, only a specific group of SWNTs will give a Raman signal for a given exci-

Semiconductor SWNTs (black points)
Metal SWNTs (gray points)
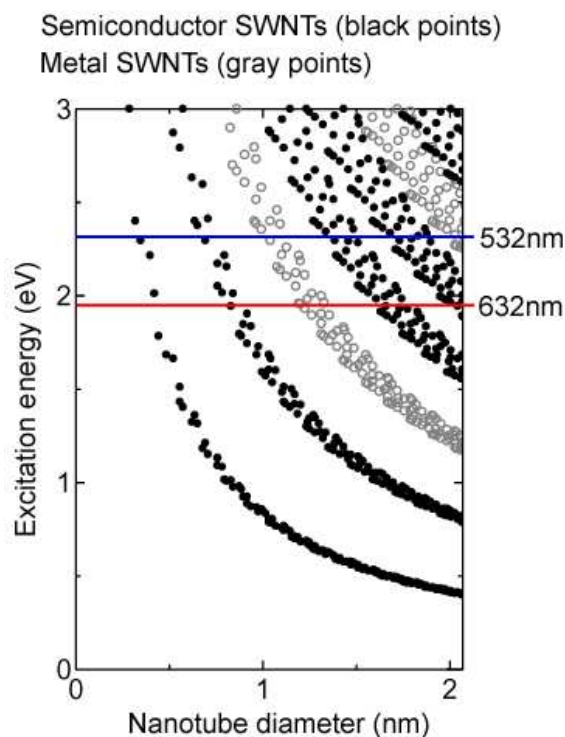
Figure 3.8: (Color) Kataura plot that shows the relationship between the excitation energy and the SWNTs diameters, as well as the distinction between metal and semiconductor SWNTs. Excitations lines for 632 and 532 nm are shown. Only the SWNTs that are under the line will give a Raman signal for the specific excitation energy. Adapted from [20]

tation energy, as predicted by Kataura and coworkers [19]. Figure 3.8 shows a region of the Kataura plot, which gives the relationship between the excitation energy and the SWNTs diameters, as well as the division between metal and semiconductor tubes.

In order to estimate the effect of catalyst concentration in the solution, Raman spectra of SWNTs grown at 950°C with $FeCp_2$ (w/w) concentrations of 0.6, 0.8, 1.0 and 1.2% were obtained. Figure 3.9 shows the Raman spectra of the SWNTs for the four concentrations of $FeCp_2$ in ethanol. The expected features for SWNTs, that is, the G and D bands and a RBM region are clearly observed. The excitation wavelength is 632 nm (He laser). Thus, only the SWNTs that respond to this specific excitation are to be considered in the analysis (see Fig. 3.8). Moreover, although we observed large diameter SWNTs during TEM observations, the Raman spectra information in this case is limited to SWNTs with diameters < 2 nm. However, useful information can be extracted from these spectra. The ratio between the intensity of the D band and the intensity of the G band (I_D/I_G) gives an estimate about the quality of the sample. A larger ratio means a sample with more structural defects. As the concentration of $FeCp_2$ increases, I_D/I_G increases, with the exception
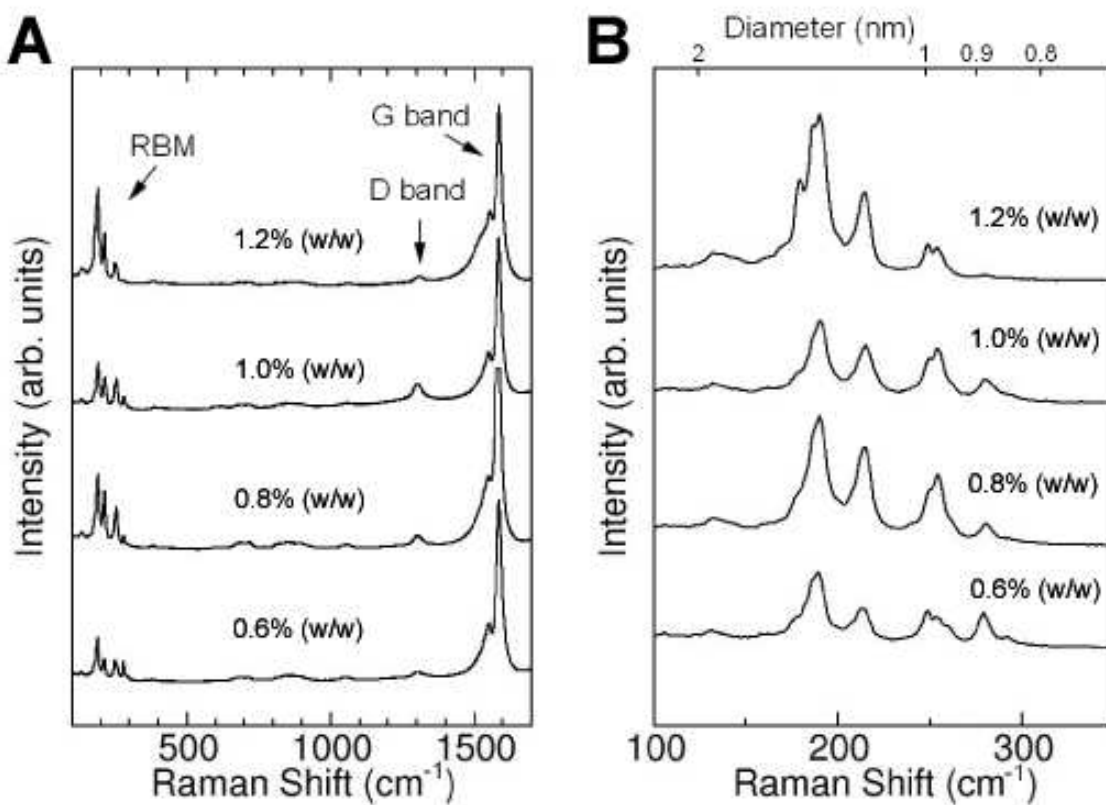
Figure 3.9: Raman spectra of SWNTs grown at 950°C with different concentrations of FeCp$_2$ in ethanol (excitation line at 632 nm). (**A**) Raman spectra that show the G-band, the D-band and the RBM frequency range for the different FeCp$_2$ concentrations. (**B**) Expanded view of RBM frequency range of panel (**A**) [17].

of the highest concentration (Fig. 3.9A). We believe that the trend is correct, and that more analysis needs to be done on the 1.2% (w/w) sample. The expanded view of the RBM frequency range is shown in Fig. 3.9B, where frequency peak signals are assigned to SWNT diameters of approximately 0.9, 1.0, 1.1, 1.3 and 1.8 nm, by applying Eq. (3.1). Thus, the samples contain both metallic and semiconductor SWNTs (see Fig. 3.8). A diminishing of the 0.9 nm diameter signal is observed as the FeCp$_2$ concentration increases, so an increase in catalyst concentration seems to restrain the growth of small diameter SWNTs.

Figure 3.10 shows the Raman spectra of SWNTs grown with a FeCp$_2$ 1.2% (w/w) concentration at different temperatures (excitation line at 532 nm). From Fig. 3.10A it is clear that as the temperature increases, the ratio I_D/I_G decreases, thus less defective SWNTs are obtained at higher temperatures. This effect has also
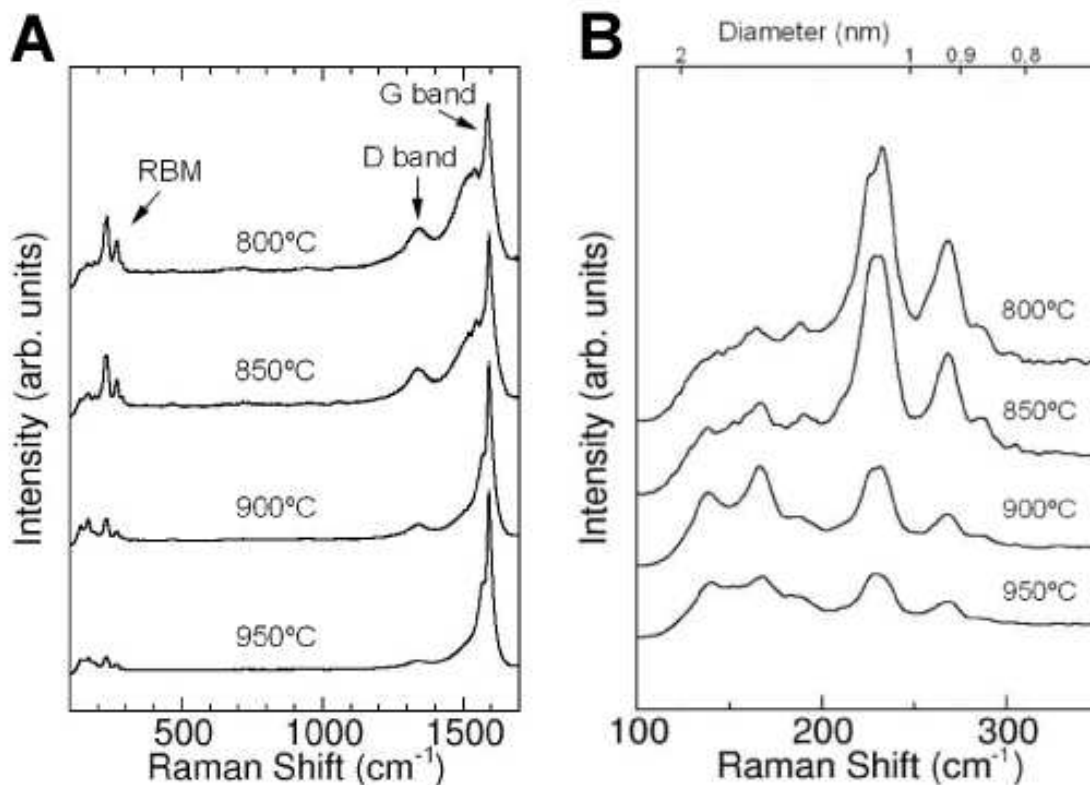
Figure 3.10: Raman spectra of SWNTs grown with a FeCp$_2$ 1.2% (w/w concetration) at various temperatures of reaction (excitation line at 532 nm). (**A**) Raman spectra that shows the G-band, the D-band and the RBM frequency range. (**B**) Expanded view of RBM frequency range of panel (**A**) for the different samples [17].

been reported by other authors [16, 21]. Moreover, as the temperature increases, Raman peaks start to appear at larger diameters, and the smaller diameter peaks ($\sim$ 1 nm) diminish. Thus, higher temperatures promote the growth of more crystalline, larger diameter SWNTs.

3.5.4   SWNT growth model

The process for SWNT growth with the pyrolysis of aerosolized solutions is described as follows: 1) The aerosol containing droplets of the metallocene-ethanol solution is carried to the reaction zone by an inert gas flow. 2) In the high temperature region the liquid droplets are vaporized and the catalyst particles are formed *in situ* via thermal decomposition of the metallocene precursor. Since the melting temperature is reduced from the bulk value for particles with diameters below 50
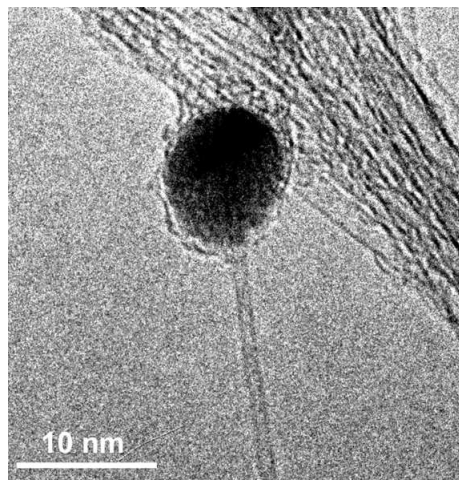
Figure 3.11: SWNT protruding from a catalyst particle. The diameter of the particle is larger than the diameter of the SWNT.

nm [22, 15], during this period the catalyst particles are in the liquid state. 3) The catalyst particles crack the gaseous ethanol molecules and carbon species diffuse into the particles, saturating them. 4) Finally, SWNTs are precipitated and the OH radicals from the ethanol molecules prevent the formation of more layers. This is a crucial step, since the pyrolysis of hydrocarbons only produces MWNTs.

It is estimated that the residence time in the reactor of the catalyst particles is in the range of seconds [15], and consequently the entire process occurs during this period of time. From these observations it is clear that SWNTs are formed in the gas phase and not on the walls of the quartz tube, contrary to MWNTs that use the quartz tube as a substrate for growth. Figure 3.11 shows a SWNT that seems to protrude from a catalyst particle. Clearly the particle's diameter is greater than the SWNT diameter. Thus, in this process the SWNT size appears not to be correlated to the catalyst particle size.

3.6   Multi-walled carbon nanotubes

In this section, we describe the synthesis of MWNTs with the ultrasonic aerosol generator by using toluene as the carbon source solvent in the aerosol. In this case, no SWNTs are produced and all of the sample is recovered from the region inside of the furnace. Quantities of ~ 1 g of MWNTs per experiment could be produced with this approach.

3.6.1   Experimental conditions

The experiments were carried out with the ultrasonic spray generator (see section 3.3.2). For the solution, $Fe(C_5H_5)_2$ was dissolved in toluene (300 mL) at a concentration of 2.5% weight of metallocene to weight of toluene (w/w). The solution was aerosolized and transferred to the furnace with a high purity Ar flow of 2.5 L/min. Reaction temperatures were varied from 700 to 950°C, and the highest yield (~ 1 g) was obtained for 800°C. The time of reaction was fixed to 15 min, after which the quartz tube was allowed to cool down to room temperature. The sample was scratched from the quartz tube and analyzed. Figure 3.12 shows a photograph of the black powder that is extracted from the quartz tube. The powder consists of MWNTs.

Figure 3.12: (Color) Photograph of the black powder scratched from the quartz tube. The powder consists of MWNTs.

3.6.2   Characterization of MWNTs

Figure 3.13 shows the X-ray diffraction pattern obtained from the black powder shown in Fig. 3.12. The walls of the MWNTs give an intense signal at a distance of 3.37 Å, the same that is obtained by graphite for the (002) planes. This proves that MWNTs are formed in average by concentric cylinders separated by 3.37 Å. The peaks are broad because the size of the particles is in the range of nanometers. Deconvolution of the broad peak at the middle of the diffractogram (Fig. 3.13, bottom) shows the existence of three peaks, which correspond to distances present in Fe_3C, α-Fe and graphite. Thus, both iron and iron carbide particles are produced during the reaction. However, the presence of iron carbides with small content of carbon ($\sim 0.1\%$ per mol) should not be discarded, since much of these phases signals in X-ray diffraction occur in the region where the broad peak is found. The peaks
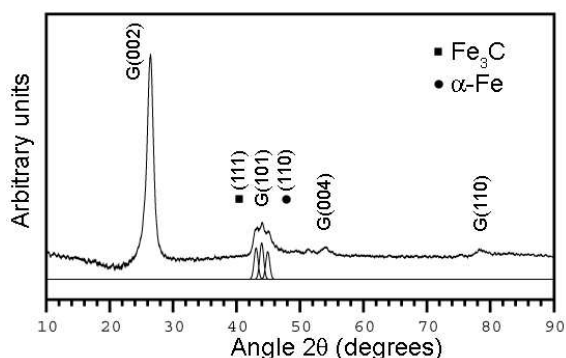
Figure 3.13: MWNTs X-ray diffraction pattern. Signals mark with G correspond to the MWNTs layers, with a distance between layers of 3.3622 Å. Signals for α-Fe (Im$\bar{3}$m, $a = 2.8662$ Å) and Fe$_3$C (P6$_3$22, $a = 4.767$ Å, $c = 4.354$ Å) are also detected. The deconvolution of the broad peak is shown at the bottom part of the image.

in the X-ray diffraction pattern that come from the MWNTs layers are similar to the (00l) reflections of graphite. Thus, we marked them as "G" peaks.

Figure 3.14 shows the structure of the black powder at different magnifications. Clearly, the sample consists of aligned MWNTs joined in stacks. These micro arrangements are known as MWNT forests. MWNTs have lengths of $\sim 350\ \mu$m and diameters of 20–80 nm (Figs. 3.14B, C and D). Thus, the aspect ratios (length/width) are of the order of 10^4, a huge number for any fiber material. Figure 3.14E shows
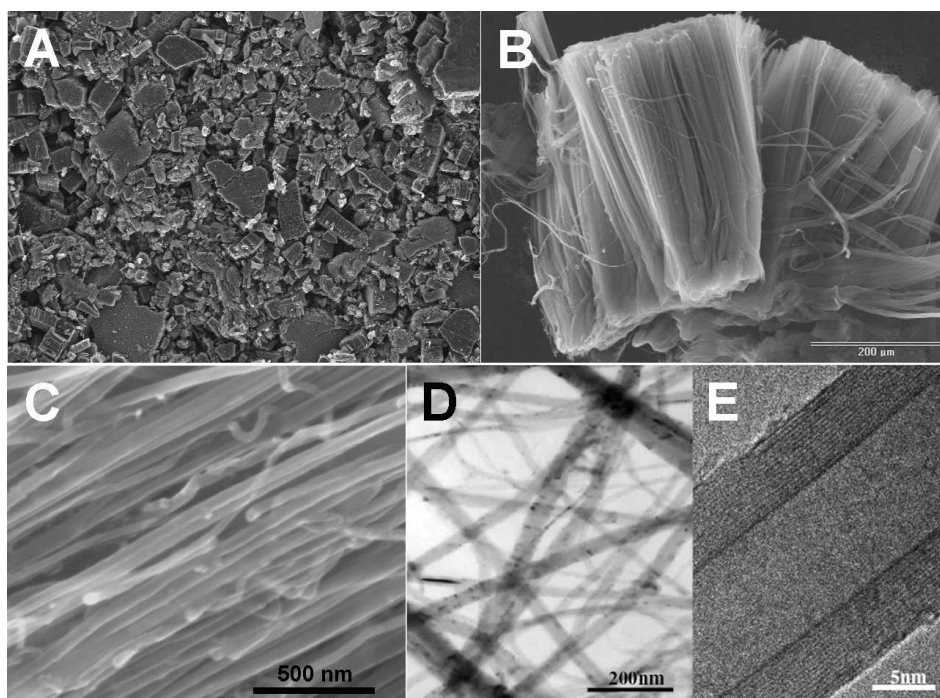
Figure 3.14: MWNTs images at different magnifications. ((**A**), (**B**) and (**C**)) SEM images. ((**D**) and (**E**)) TEM and HRTEM images. The aligned MWNTs form a micro structure that resembles a forest.

a high resolution TEM image (HRTEM) of a single MWNT, where the concentric carbon layers (0.34 nm) are depicted. In general, these MWNTs are not perfect. It is common to find defective walls or kinks. Also, catalyst particles either inside or outside the tubes are found in the as-grown samples (Fig. 3.14D).

3.6.3 MWNT growth model

Contrary to SWNTs, that are formed completely in the gas phase, MWNTs grow inside the furnace from the quartz tube substrate. In fact, it has been demonstrated that only on certain substrates will MWNT growth occur. For example, MWNTs will not grow on pure Si substrates [23]. Figure 3.15 shows a MWNT forest attached to a SiO_2 thin layer. EDX elemental mapping shows the chemical composition of the regions, where it is clear that on top of the thin layer substrate only MWNTs are found. Although catalyst particles are found in all regions of the sample, from the above observations it seems that, for this particular experimental setup, a based-growth instead of tip-growth mechanism takes place during the reaction.
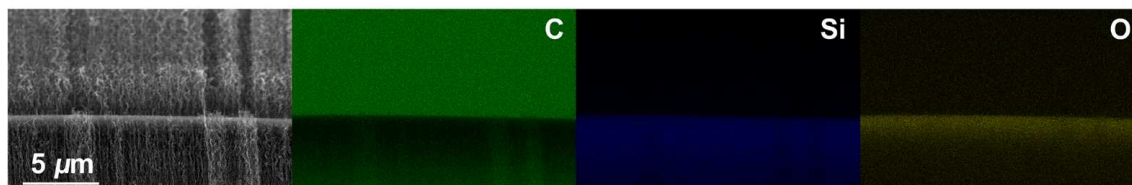
Figure 3.15: (Color) EDX elemental mapping of the base of a MWNT forest. Elements mapped are C, Si and O. The MWNT forest grows from the SiO_2 substrate.

3.7 Growth of nitrogen-doped MWNTs

It has been shown that nitrogen-doped MWNTs (CN_x) can be synthesized by introducing a solvent that contains nitrogen in the solution to be pyrolized [11, 24, 25]. This effect has opened new avenues for CNT-based chemistry, where common reactions involving nitrogen atoms could be realized without the need of applying prior chemical treatments on non-doped CNTs. For example, the attachment of gold

[26] and silver [27] nanoparticles to CN_x has been achieved, as well as the covalent attachment of polymers [28].

In this section we analyze the growth rates and diameter distributions of CN_x, in order to assess their micro-structural properties. In this way, specific lengths and diameters could be prepared for further chemical modifications to be used in technological applications.

3.7.1 Experimental conditions

For CN_x growth we used the same experimental parameters used in MWNT synthesis (see section 3.6), with the exception of the solvent, which in this case is benzylamine (C_7H_8N), a compound that contains one nitrogen atom. The doping is induced by this compound. Also, it was found that the reaction temperature for highest yield was 850°C.

3.7.2 Characterization of CN_x

Figure 3.16 shows the diffraction pattern for the CN_x sample grown at 15 min. The pattern is similar to the one obtained for MWNTs (cf. Fig. 3.13), and by doing the same deconvolution analysis it is found that signals for α-Fe and Fe_3C could be present. That is, nanoparticles mixed with the CNTs are present in the sample.
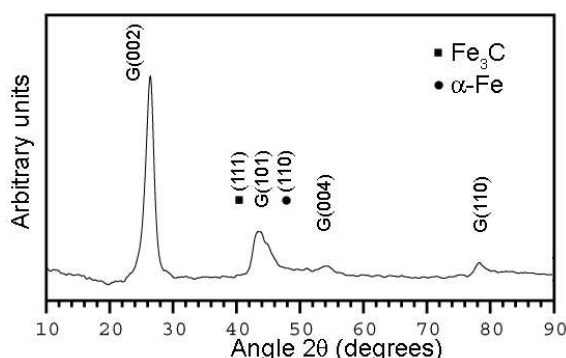
Figure 3.16: CN_x X-ray diffraction pattern. Signals mark with G correspond to the MWNTs layers, with a distance between layers of 3.3622 Å. Signals for α-Fe (Im$\bar{3}$m, $a = 2.8662$ Å) and Fe_3C (P$6_3$22, $a = 4.767$ Å, $c = 4.354$ Å) are also detected.

Figure 3.17 shows the TGA of CN_x and MWNTs in a dry air atmosphere. The CN_x are clearly less resistant to oxidation treatments. Since it has been estimated that the concentration of N is ~ 3 % weight of N atoms to weight of CN_x [25], the tendency to oxidize faster could be a consequence of reactive sites generated by the

Figure 3.17: TGA in dry air of MWNTs (black line) and CN_x (gray line). The CNTs present a different response to oxidation. The residual weight % is of ~ 3 %, for both cases.
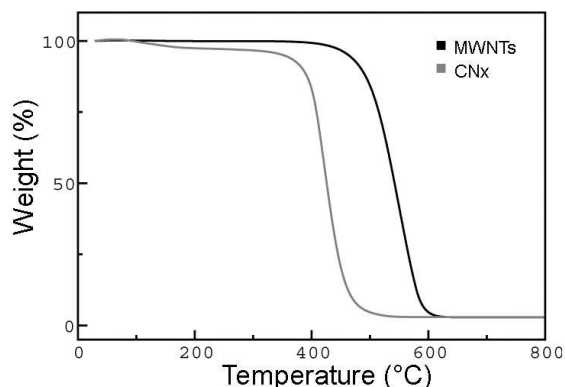
presence of N atoms. However, structural defects could also be responsible for this behavior. In both cases, the residual material obtained after complete oxidation consists of iron oxide (hematite), and has a weight of approximately 3 % of the initial sample.

By inserting a SiO_2 substrate into the furnace it is possible to obtain CN_x forests, which can be easily removed from the furnace area without having to scratch the sample. Figure 3.18 shows the length of CN_x forests as a function of time, which gives an estimated growth rate of ~ 10 μm/min. However, the growth rate is not linear, and it is influenced by the particular experimental conditions like gas flow, area of the quartz tube, temperature, etc.

Figure 3.19 shows the diameter distributions of the CN_x forests of Fig. 3.18. An increase of diameter as a function of time was expected. However, this did not
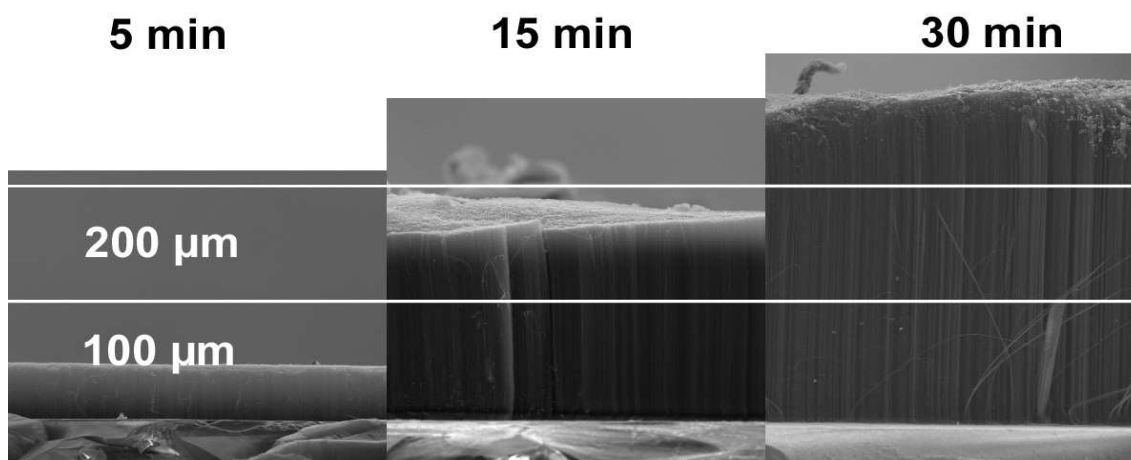
Figure 3.18: CN_x forests as a function of time, for 5, 15 and 30 minutes. The CN_x were grown on a $Si_2 0$ substrate (1 cm^2) previously placed inside the reaction zone.
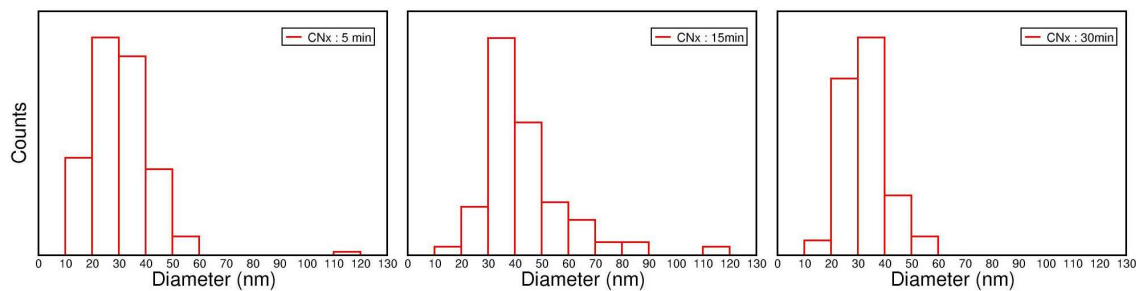
Figure 3.19: Diameter distributions of CN_x for 5, 15 and 30 minutes of reaction time.
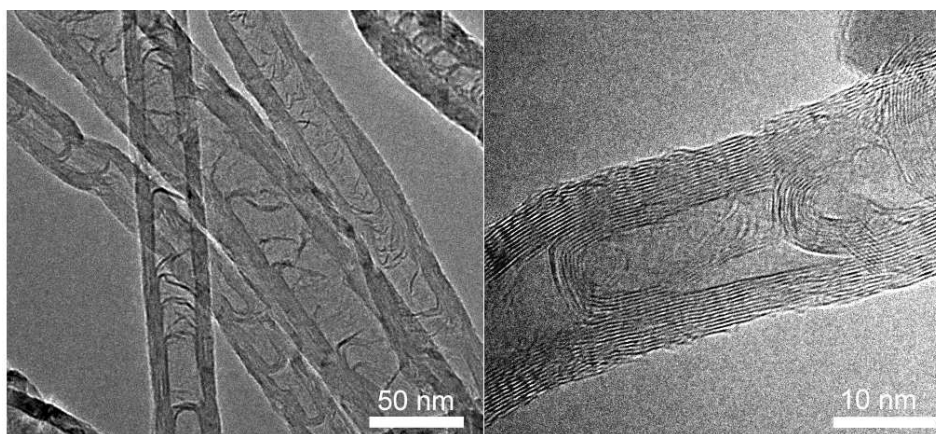
Figure 3.20: TEM images of CN_x, where the bamboo structure can be seen.

occur. CN_x have an estimated diameter range of 20–50 nm and diameters of more than 60 nm are rarely observed with this process. This shows that the diameter of CN_x is defined at the initial stages of growth. Thus, although not to the desired level of specific chiralities, some rough control of the micro-structure of the CN_x is achievable.

Finally, in Fig. 3.20 we show TEM images of the atomic arrangement of CN_x. These tubes have a bamboo-type structure, where internal caps create compartments of around 20–40 nm. It has been suggested that these compartments match exactly with the catalyst precursor morphology during CN_x growth.

3.8   Metal inclusions inside MWNTs

Soon after the structure of CNTs was clarified [29], it was realized that the hollow core of CNTs could serve as a container for foreign materials. Ajayan and Iijima demonstrated that MWNTs produced with the arc-discharge method could be filled with molten lead, through capillarity action [30]. Since then, not only a wide range of metals (e.g., Ti, Cr, Fe, Co, Ni, Cu, Zn, Mo, Pd, Sn, Ta, W, Gd, Dy and Yb [31]) have been introduced in the core of tubes, but also carbides [32], oxides [33], molecules [34], liquids [35] and gases [36]. Besides capillarity-induced filling [30], other techniques have been employed to fill tubes. When metals are implanted in the C anode used in the arc-discharge chamber, some of the grown CNTs present encapsulated metal particles [32, 31]. In addition, with wet chemical techniques, where the CNTs are opened with an acid treatment before filling, metal oxides were successfully encapsulated [37]. As a side effect, in the pyrolysis of aerosolized solutions, catalyst particles are found encapsulated in some of the produced CNTs [7, 8, 11]. This effect can become cumbersome for some applications, and methods to extract encapsulated particles have been proposed [38]. However, encapsulated ferromagnetic materials could be of use in technological applications, since, when encapsulated, these nano size particles are protected from the surrounding environment and inherit the cylindrical shape of the host MWNTs. In this section, we analyze the encapsulation of Fe, Ni, Co and a FeCo alloy within MWNTs. These materials were produced by using different metallocenes as the catalyst precursor in the solution to be pyrolized. The following notation is used: a M@MWNT represents a MWNT that contains metals inclusions (e.g. M = Fe, Co, etc.).

3.8.1   Fe@MWNTs

From our analysis of MWNTs and CN_x grown by using $FeCp_2$ as the catalyst precursor (see sections 3.6 and 3.7) it can be guessed that some of the catalyst particles are encapsulated by the CNTs' walls. Figure 3.21 shows various examples of commonly observed encapsulated Fe particles. Usually, they have a wire shape,
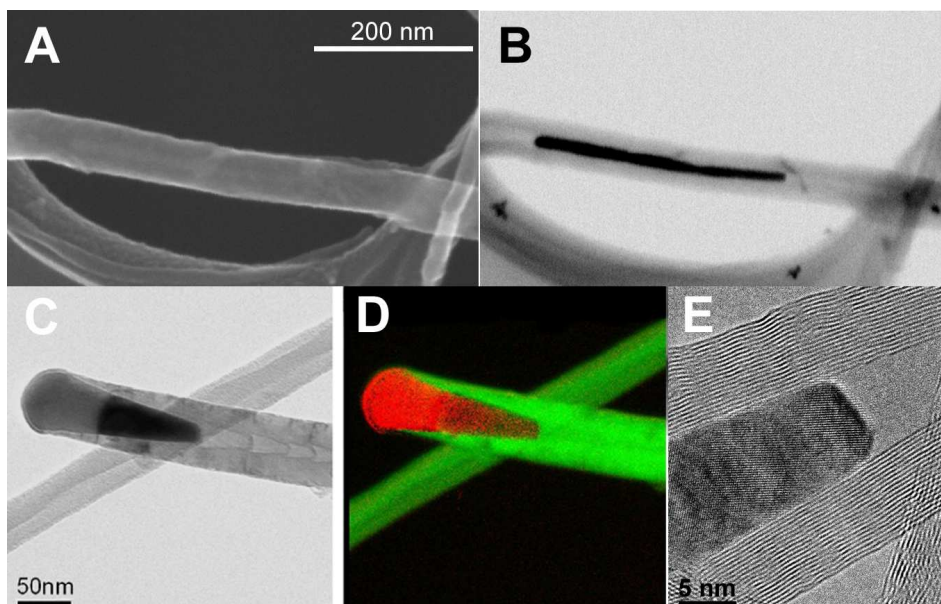
Figure 3.21: (**A** and **B**) (Color) SEM image and bright field image of an Fe nanowire. (**C** and **D**) TEM image and EELS map of a Fe particle at the tip of a CN_x. (**E**) HRTEM image of an Fe particle that shows the crystalline state.

with lengths larger than 200 nm in some cases. Interestingly, from our observations, it appears that all are in the form of single crystals.

From the X-ray diffraction patterns of MWNTs and CN_x (Figs. 3.16 and 3.13), it should be remembered that when using an Fe-containing catalyst precursor, besides pure metal particles, iron carbide particles also form.

3.8.2 Co@MWNTs

Sample preparation and experimental conditions

MWNTs containing nanowires of Co were produced with the injection aerosol generator (section 3.3.1). A solution containing cobalt (II) acetylacetonate ($Co(C_5H_7O_2)_2$) at a concentration of 2.5% weight of solute to weight of toluene (5 ml) was prepared. The solution was sonicated for 15 minutes and transfered to the aerosol container. The temperature of reaction was 850°C during the experiment, and the gas (Ar) flow was kept at 3.5 L/min. After all the solution was sprayed out, the furnace was turned off. When the quartz tube reached room temperature the sample was scratched out from the quartz tube to be analyzed. Results are shown

below.

X-ray diffraction

The X-ray diffraction pattern, after background subtraction, of the as grown sample is shown in Fig. 3.22. The (002) graphite peak comes from the MWNTs layers. The pattern reveals an *fcc* structure for Co. Although the stable phase of Co is *hcp* under normal conditions, it has been reported by other authors that Co contained inside MWNTs has the *fcc* structure [39].
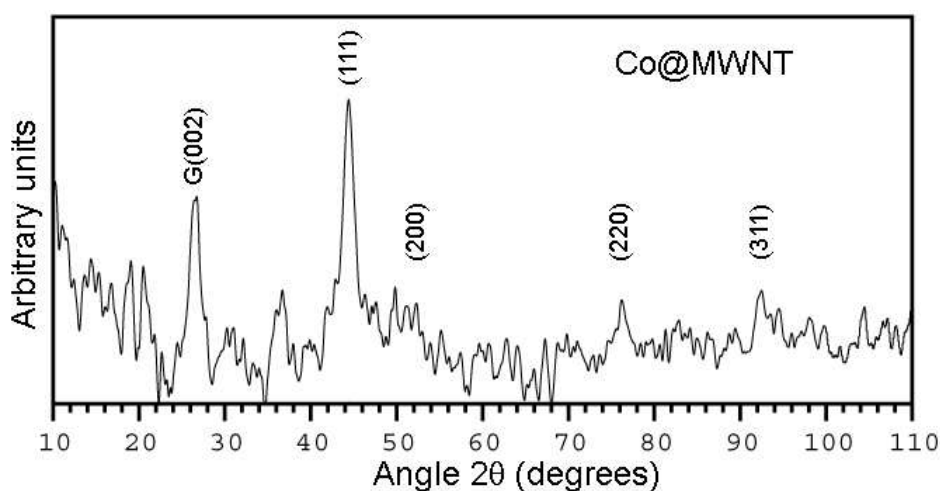
Figure 3.22: X-ray diffraction pattern of Co@MWNTs after background subtraction. The signal marked with G corresponds to graphite. The rest of the peaks correspond to the *fcc* Co phase (Fm3m, $a = 3.5447$).

SEM and TEM analysis

The sample consists of a mixture of amorphous material and MWNTs, as shown in Fig. 3.23A. MWNTs are found in bundles with lengths < 10 μm and are usually covered at the top with a thick amorphous layer (Fig. 3.23B). On average, the diameter of the tubes is $\sim$ 25nm (Fig. 3.23C). Figures 3.23D and E show two examples of commonly observed encapsulated wire-shaped Co particles inside the MWTNs' core. The nanowires have lengths of $\sim$ 40 nm and diameters of $\sim$ 5 nm, thus, the aspect ratio (length/width) of these structures is close to 8. Fig. 3.23F shows the crystalline state of the Co nanowires. No twin boundaries were observed,
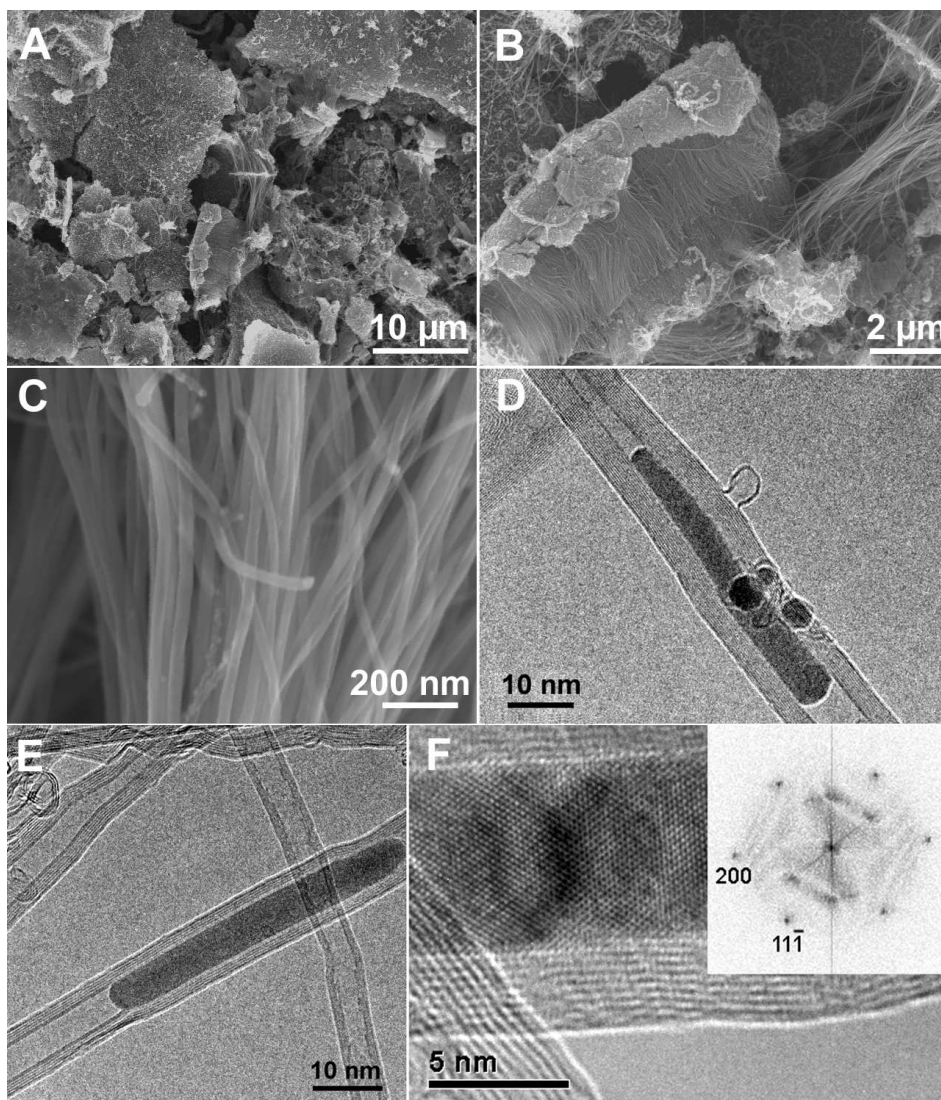
Figure 3.23: (**A**, **B**, and **C**) SEM images of the Co@MWNTs sample at different magnifications. (**D** and **E**) Two examples of commonly observed wire-shaped Co particles. (**F**) Crystalline state of a Co nanowire. In the inset, the FFT pattern agrees with the [011] zone axis of the *fcc* Co structure.

which indicates that a large fraction of the nanowires are in fact a single crystal. In the inset of figure Fig. 3.23F the fast Fourier transform (FFT) of the image is shown. The reciprocal space pattern agrees with the [011] zone axis of the *fcc* Co structure.
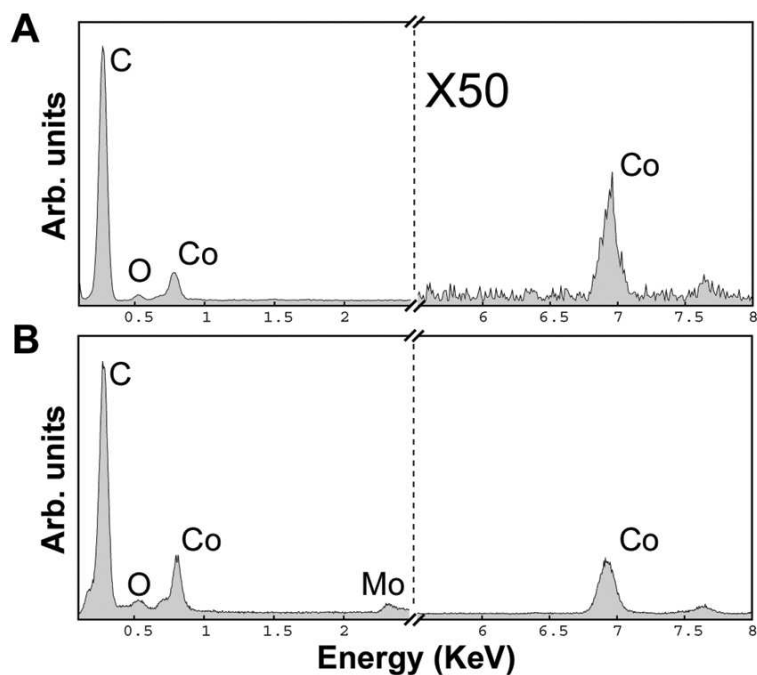
Figure 3.24: EDX spectra of Co@MWNTs. (**A**) EDX spectrum of a wide region of the sample taken inside an SEM. (**B**) EDX spectrum of a single Co@MWNT taken inside a TEM. In the spectra signals from C, Co and O are recognized. The Mo signal in (**B**) comes from the TEM grid.

EDX spectra

Figure 3.24 shows the EDX spectra of the Co@MWNT sample (after background subtraction). From a wide scan inside the SEM, signals from C (0.282 KeV), and Co (6.929 and 0.776 KeV for the K and L peaks) are clearly seen (Fig. 3.24A). Also, oxygen is present in the sample (0.523 KeV). The spectrum, coming from a general area, gives a qualitative idea of the Co content in the sample. But some of the signal may come from the amorphous area and particles outside the tubes. An EDX spectrum from a single Co@MWNT is shown in Fig. 3.24B. Equally, C and Co signals were obtained, as well as oxygen (in small amounts).

From a standardless EDX quantification of the spectra, the calculated weight percentages of C and Co are 85.6 and 13.2%, respectively. The rest comes from O (less than 2%), which probably is attached to particles outside the tubes.

3.8.3 Ni@MWNTs

Sample preparation and experimental conditions

Two approaches were used to produce MWNTs containing inclusions of Ni. In the first case, nickel (II) acetylacetonate ($Ni(C_5H_7O_2)_2$) was dissolved in toluene (5 mL) at a concentration of 2.5% weight of compund to weight of toluene (w/w). For the second case, the same proportions were used, but with $NiCp_2$ as the compound catalyst and ethanol as the solvent. In both methods, the synthesis was carried out with the injection aerosol generator (see section 3.3.1). For each case, the solution was sonicated for 15 minutes and transferred to the aerosol container. The temperature of reaction was 850°C during the experiments, and the gas (Ar) flow was kept at 3.5 L/min. The samples were extracted from the quartz tube once the furnace reached room temperature. Results are shown below.

X-ray diffraction

Figure 3.25 shows the X-ray diffraction patterns, after background subtraction, of both synthesized Ni@MWNT samples, where peaks for Ni can be assigned to the *fcc* structure in both cases. It is important to notice that amorphous silicon oxide
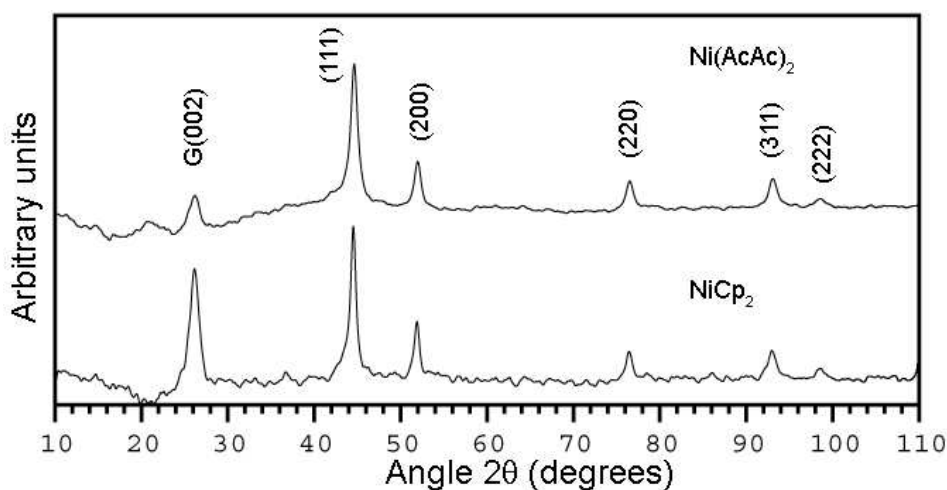
Figure 3.25: X-ray diffraction patterns of Ni@MWNTs after background subtraction. The top part: Ni@MWNTs produced with $Ni(AcAc)_2$ dissolved in toluene. Bottom part: Ni@MWNTs produced with $NiCp_2$ dissolved in ethanol.
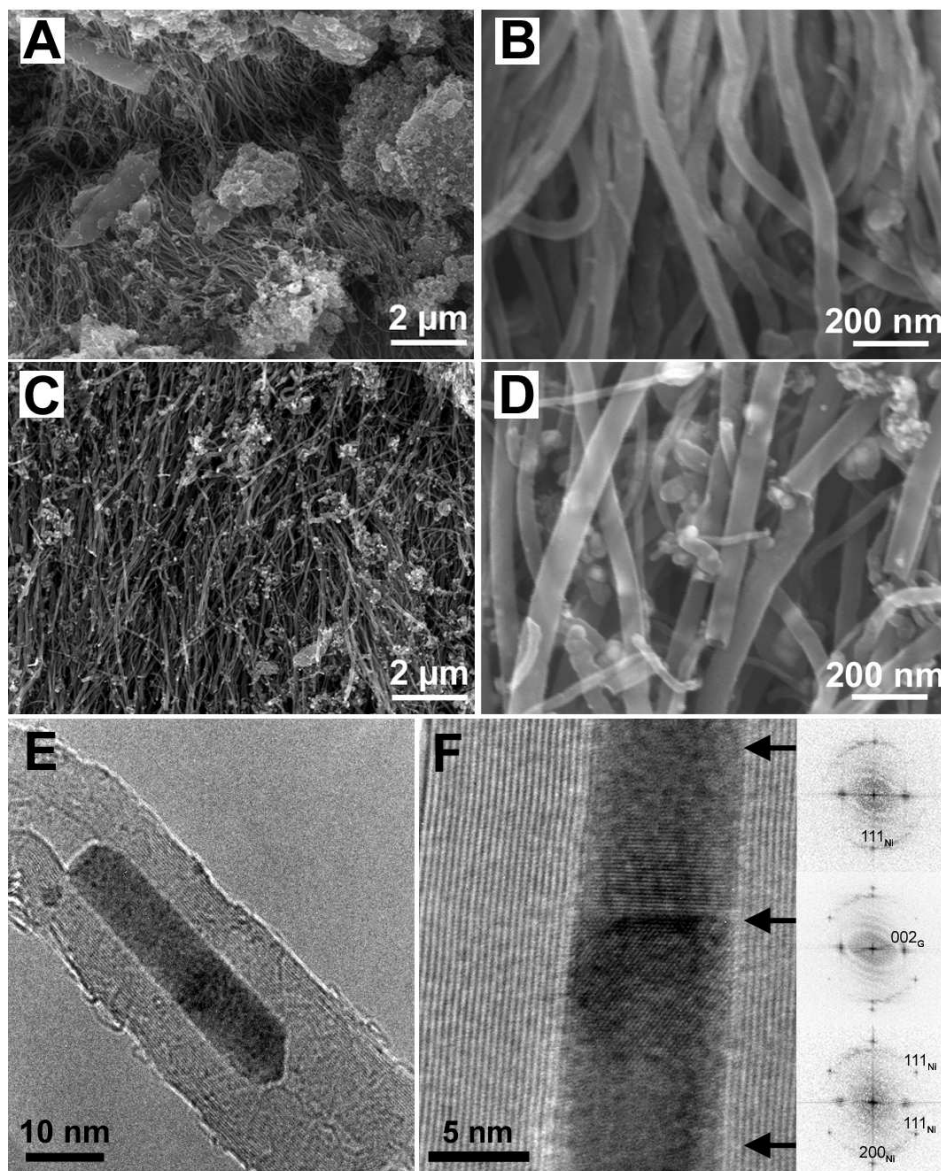
Figure 3.26: (**A** and **B**) SEM images at different magnifications of the sample produced with Ni(AcAc)$_2$. (**C** and **D**) SEM images at different magnifications of the sample produced with NiCp$_2$. (**E**) TEM image of a wire-shaped Ni particle inside the core of a MWNT. (**F**) HRTEM image that shows the crystalline state of a Ni nanowire. The crystal clearly has a boundary region that separates two crystallographic directions. The FFT patterns from the top, middle and bottom region of the image are shown in the inset.

was used as a substrate for data acquisition. Since the substrate produces a broad peak in the region of the graphitic (002) signal, the intensity of this particular peak is artificially diminished during background subtraction.

SEM and TEM analysis

SEM images at different magnifications for the Ni@MWNT samples produced with $Ni(AcAc)_2$ and $NiCp_2$ are shown in Figs. 3.26A and B and Figs. 3.26C and D, respectively By comparing Figs. 3.26B and D it is possible to observe that the thickest tubes are produced when $NiCp_2$ was dissolved in ethanol, with diameters up to 80 nm. Figure 3.26E shows an example of a Ni nanowire encapsulated in a MWNT. As in the Fe and Co cases, Ni inclusions are single crystals in the majority
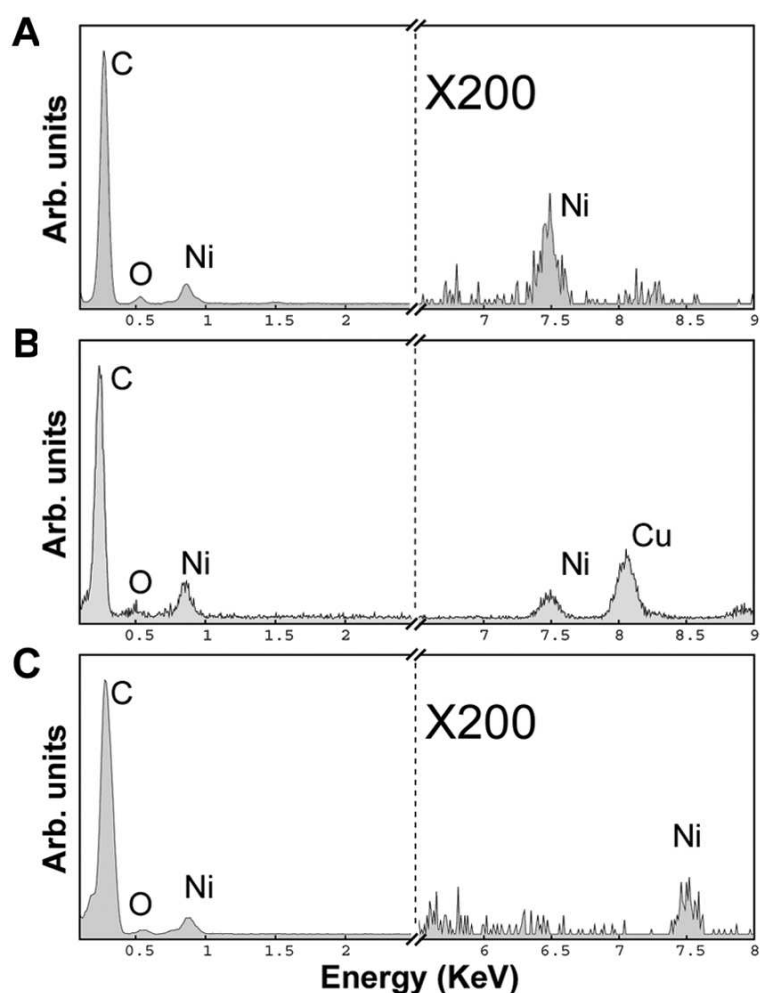
Figure 3.27: EDX spectra of Ni@MWNTs. (**A** and **B**) EDX spectrum of a wide region of the sample taken inside and SEM and EDX spectrum of a single Ni@MWNT acquired in a TEM, of the sample produced with $Ni(AcAc)_2$. (**C**) EDX spectrum of a wide region of the sample produced with $NiCp_2$ taken inside an SEM. In the spectra, signals from C, Ni and O are recognized. The Cu signal in (**B**) comes from the TEM grid.

of the cases, hovever, Fig.3.26F shows an example of a grain boundary in a Ni nanowire. From the FFT patterns, Ni has the *fcc* structure.

EDX spectra

Figures 3.27A and B show EDX spectra (after background subtraction) from the Ni(AcAc)$_2$ sample. Signals from C (0.282 keV), and Ni (7.477 and 0.851 keV for the K and L peaks) are clearly seen. Also, oxygen is present in the sample (0.523 keV). An EDX spectrum from the sample produced with NiCp$_2$ is shown in Fig.3.27C, where the presence of Ni is also demonstrated.

3.8.4   FeCo@MWNTs

Sample preaparation and experimental conditions

To produce MWNTs containing metal inclusions of a FeCo alloy, the ultrasonic spray generator (see section 3.3.2) was used. For the solution, a mixture of FeCp$_2$ and CoCp$_2$ in a 1:1 proportion was dissolved in toluene (300 mL) at a concentration of 2.5% weight of the metallocene mixture to weight of toluene (w/w). The solution was aerosolized and transferred to the furnace with a high purity Ar flow of 2.5 L/min. Reaction temperatures were varied from 600 to 800°C. The time of reaction was fixed to 15 min, after which the quartz tube was allowed to cool down to room temperature. The sample was scratched from the quartz tube and analyzed.

X-ray diffraction

Figure 3.28 shows the X-ray diffraction pattern of FeCo@MWNTs produced at different temperatures. An FeCo alloy is observed for samples prepared between 650 and 750°C . The presence of Fe$_3$C (cementite) and the interlayer graphite reflections (000l) are present as well as signals for *fcc* cobalt. For preparation temperatures higher than 800°C, the FeCo alloy disappeared almost completely X-ray diffraction simulations clearly confirmed that an *bcc* FeCo alloy (Im3m, $a = 2.85$ Å) was obtained at pyrolytic temperatures between 650 and 750°C.
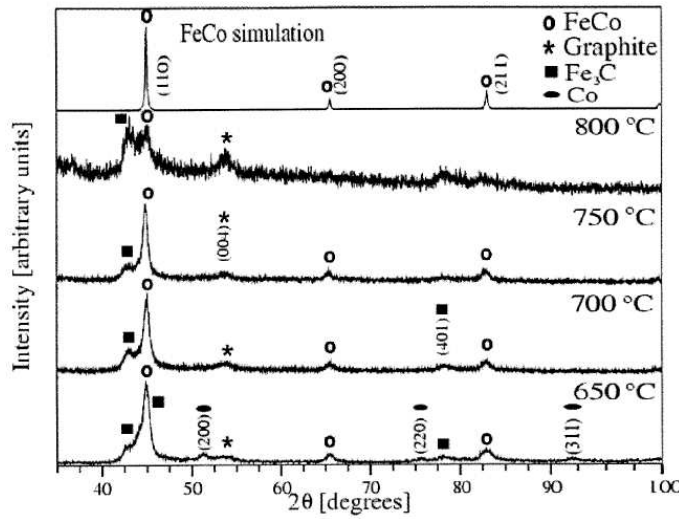
Figure 3.28: X-ray diffraction of FeCo@MWNTs at different temperatures of growth. An X-ray simulate diffraction pattern of the FeCo alloy is shown for comparison [40].
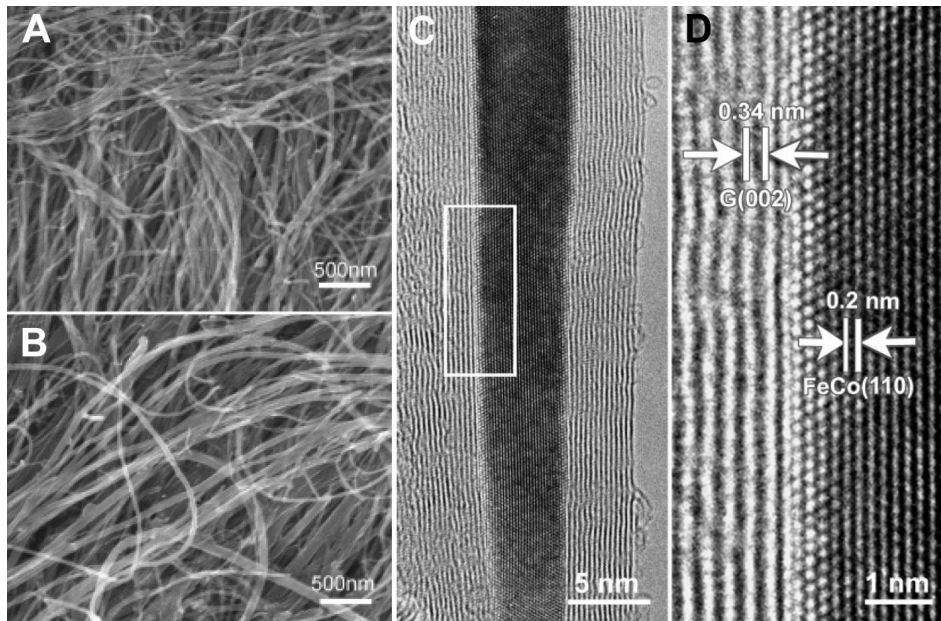
Figure 3.29: (**A** and **B**) SEM images of FeCo@MWNTs produced at 700 and 750°C, respectively. (**C**) TEM image of a FeCo nanowire, from a sample produced at 700°C. (**D**) Detail of the region marked in (**C**), where distances in the crystal and the MWNT layers are indicated [40].

SEM and SEM analysis

Figure 3.29 shows SEM and TEM images of FeCo@MWNTs. It is noteworthy that the amount of material produced at 650°C was less relative to that obtained at temperatures higher than 750 C (e.g., 1:15). The encapsulated metal particles are single crystals, that in some cases show an epitaxial relationship with the MWNTs

Figure 3.30: (Color) TGA in dry air of FeCo@MWNTs grown at different temperatures. As the temperature of synthesis decreases, the resistance to oxidation decreases and the residual weight increases.
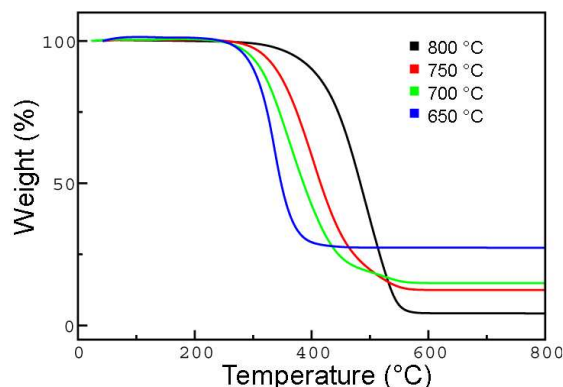
layers.

TGA analysis

Figure 3.30 shows the TGA analysis for FeCo@MWNTs grown at different temperatures. As the temperature of synthesis decreases, the resistance to oxidation decreases, but the residual weight increases. In order of decreasing temperature the residual weights are 4.22, 12.43, 14.84, and 27.27. Thus, it appears that lower temperatures of growth promotes more filling. However, this hypothesis requires more analysis.

3.9 Conclusions

The pyrolysis of aerosolized solutions could be used as a technique to synthesize different types of CNTs. In particular, the aerosol can be produced with at least two techniques, the injection of a solution through a capillary tube or by ultrasonic vibration of the solution.

SWNTs could be grown with the ultrasonic aerosol generator by using a $FeCp_2$-ethanol solution as the carbon source and catalyst precursor. Large threads ($\sim$ 10 cm) of SWNT bundles mixed with catalyst particles are obtained by extracting a film that is deposited on the quartz tube outside of the reaction zone. The highest yield was obtained for a $FeCp_2$ 1.2% (w/w) concentration in ethanol at a reaction temperature of 950°C. With this process metal and semiconductor SWNTs are obtained. An increment in the catalyst concentration promotes the appearance

of larger diameter SWNTs. Equally, high temperatures (950°C) promote larger diameter SWNTs and increase the quality of the sample.

MWNTs and CN_x are obtained by using toluene and benzylamine, respectively, as the solvent in the solution. Forests of more than 100 μm in length of MWNTs and N-doped MWNTs could be produced by inserting SiO_2 substrates in the reaction zone. The increase in time of reaction does not seem to influence the final diameter of the CN_x.

Moreover, different metals can be encapsulated by varying the type of catalyst precursor used in the solution to be aerosolized. Specifically, we have used different metallocenes as catalyst precursors and characterized MWNTs encapsulating Fe, Co, Ni and a FeCo alloy.

References

[1] Hongjie Dai. Nanotube growth and characterization. In M.S. Dresselhaus, G. Dresselhaus, and P. Avouris, editors, *Carbon nanotubes: synthesis, structure, properties and applications*, volume 80 of *Topics Appl. Phys.*, pages 29–53. Springer-Verlag, 2001.

[2] P. J. F. Harris. *Carbon nanotubes and related structures*. Cambridge university press, 1999.

[3] T. W. Ebbesen and P. M. Ajayan. Large-scale synthesis of carbon nanotubes. *Nature*, 358:220–221, 1992.

[4] D. S. Bethune, C. H. Kiang, M. S. de Vries, G. Gorman, R. Savoy, J. Vazquez, and R. Beyers. Cobalt-catalyzed growth of carbon nanotubes with single-atomic-layer walls. *Nature*, 363:605–607, 1993.

[5] T. Guo, P. Nikolaev, A. G. Rinzler, D. Tománek, Colbert. D. T., and R. E. Smalley. Self-assembly of tubular fullerenes. *J. Phys. Chem.*, 99:10694–10697, 1995.

[6] T. Guo, P. Nikolaev, A. Thess, D. T. Colbert, and R. E. Smalley. Catalytic growth of single-walled nanotubes by laser vaporization. *Chem. Phys. Lett.*, 243:49, 1995.

[7] N. Grobert, M Terrones, A. J. Osborne, H. Terrones, W. K. Hsu, S. Trasobares, Y. Q. Zhu, J. P. Hare, H. W. Kroto, and D. R. M. Walton. Thermolysis of C_{60} thin films yields ni-filled tapered nanotubes. *Appl. Phys. A*, 67:595–598, 1998.

[8] C. N. R. Rao and S. Rahul. Large aligned-nanotube bundles from ferrocene pyrolysis. *Chem. Commun.*, 15:1525–1526, 1998.

[9] R. Kamalakaran, M. Terrones, T. Seeger, Ph. Kohler-Redlich, M. Rühle, Y. A. Kim, T. Hayashi, and M. Endo. Synthesis of thick and crystalline nanotube arrays by spray pyrolysis. *Appl. Phys. Lett.*, 77:3385–3387, 2000.

[10] M. Mayne, N. Grobert, M. Terrones, R. Kamalakaran, M. Rühle, H. W. Kroto, and D. R. M. Walton. Pyrolytic production of aligned carbon nanotubes from homogeneously dispersed benzene-based aerosols. *Chem. Phys. Lett.*, 338:101–107, 2001.

[11] M. Reyes-Reyes. *Producción controlada y caracterización de nanotubos alineados parcialmente llenos de materiales ferromagnéticos sintetizados por métodos pirolíticos.* PhD thesis, UNAM, 2003.

[12] M. Pinault, M. Mayne-L'Hermite, C. Reynaud, V. Pichot, P. Launois, and D. Ballutaud. Growth of multiwalled carbon nanotubes during the initial stages of aerosol-assisted ccvd. *Carbon*, 43:2968–2976, 2005.

[13] C. Journet, W. K. Maser, P. Bernier, A. Loiseau, M. Lamy De La Chapelle, S. Lefrant, P. Deniard, R. Lee, and J. E. Fischer. Large-scale production of single-walled carbon nanotubes by the electric-arc technique. *Nature*, 388:756–758, 1997.

[14] A. Thess, R. Lee, P. Nikolaev, H. Dai, P. Petit, J. Robert, C. Xu, Y. H. Lee, S. G. Kim, A. G. Rinzler, D. T. Colbert, G. E. Scuseria, D. Tománek, J. E. Fischer, and R. E. Smalley. Crystalline ropes of metallic carbon nanotubes. *Science*, 273:483–487, 1996.

[15] A. Moisala, A. G. Nasibulin, and E. I. Kauppinen. The role of metal nanoparticles in the catalytic production of single-walled carbon nanotubes–a review. *J. Phys.: Condens. Matter*, 15:S3011–S3055, 2003.

[16] S. Maruyama, K. Ryosuke, Y. Miyauchi, S. Chiashi, and M. Kohno. Low-temperature synthesis of high-purity single-walled carbon nanotubes from alcohol. *Chem. Phys. Lett.*, 360:229–234, 2002.

[17] F. Lupo, J. A. Rodríguez-Manzo, A. Zamudio, A. L. Elías, Y. A. Kim, T. Hayashi, M. Muramatsu, R. Kamalakaran, H. Terrones, M. Endo, M. Rühle, and M. Terrones. Pyrolytic synthesis of long strands of large diameter single-walled carbon nanotubes at atmospheric pressure in the absence of sulphur and hydrogen. *Chem. Phys. Lett.*, 410:384–390, 2005.

[18] M. S. Dresselhaus, G. Dresselhaus, A. Jorio, A. G. Souza Filho, and R. Saito. Raman spectroscopy on isolated single wall carbon nanotubes. *Carbon*, 40:2043–2061, 2002.

[19] H. Kataura, Y. Kumazawa, Y. Maniwa, I. Umezu, S. Sussuki, Y. Ohtsuka, and Y. Achiba. Optical properties of single-wall carbon nanotubes. *Synthetic Metals*, 103:2555–2558, 1999.

[20] S. Maruyama. http://www.photon.t.u-tokyo.ac.jp/ maruyama/index.html.

[21] J. E. Herrera, L. Balzano, F. Pompeo, and D. E. Resasco. Raman characterization of SWNT of various diameters obtained by catalytic disproportation of CO. *J. Nanosci. Nanotech.*, 3:133–138, 2003.

[22] Ph. Buffat and J-P. Borel. Size effect on the melting temperature of gold particles. *Phys. Rev. A*, 13:2287–2299, 1976.

[23] Y. J. Jung, B. Wei, R. Vajtai, and P. M. Ajayan. Mechanism of selective growth of carbon nanotubes on SiO_2/Si patterns. *Nano Lett.*, 3:561–564, 2003.

[24] M. Reyes-Reyes, N. Grobert, R. Kamalakaran, T. Seeger, D. Golberg, M. Rühle, Y. Bando, H. Terrones, and M. Terrones. Efficient encapsulation of gaseous nitrogen inside carbon nanotubes with bamboo-like structure using aerosol thermolysis. *Chem. Phys. Lett.*, 396:167–173, 2004.

[25] A. L. Elías Arriaga. *A multidisciplinary study of carbon nanotube structures: from inorganic to biological systems.* PhD thesis, IPICYT, 2006.

[26] K. Jiang, A. Eitan, L. S. Schadler, P. M. Ajayan, R. W. Siegel, N. Grobert, M. Mayne, M. Reyes-Reyes, H. Terrones, and M. Terrones. Selective attachment of gold nanoparticles to nitrogen-doped carbon nanotubes. *Nano Lett.*, 3:275–277, 2003.

[27] A. Zamudio, A. L. Elías, J. A. Rodríguez-Manzo, F. López-Urías, G. Rodríguez-Gattorno, F. Lupo, M. Rühle, D. J. Smith, H. Terrones, D. Díaz, and M. Terrones. Efficient anchoring of silver nanoparticles on N-doped carbon nanotubes. *Small*, 2:346–350, 2005.

[28] M. Dehonor, K. Masenelli-Varlot, A. González-Montiel, C. Gauthier, J. Y. Cavaillé, H. Terrones, and M. Terrones. Nanotube brushes: polystyrene grafted covalently on CNx nanotubes by nitroxide-mediated radical polymerization. *Chem. Commun.*, 42:5349–5351, 2005.

[29] S. Iijima. Helical microtubules of graphitic carbon. *Nature*, 254:56–58, 1991.

[30] P. M. Ajayan and S. Iijima. Capillarity-induced filling of carbon nanotubes. *Nature*, 361:333–334, 1993.

[31] C. Guerret-Piécourt, Y. Le Bouar, A. Lolseau, and H. Pascard. Relation between metal electronic structure and morphology of metal compounds inside carbon nanotubes. *Nature*, 372:761–765, 1994.

[32] R. S. Ruoff, D. C. Lorents, B. Chan, R. Malhotra, and S. Subramoney. Single crystal metals encapsulated in carbon nanoparticles. *Science*, 259:346–348, 1993.

[33] P. M. Ajayan, T. W. Ebbesen, T. Ichihashi, S. Iijima, K. Tanigaki, and H. Hiura. Opening carbon nanotubes with oxygen and implications for filling. *Nature*, 362:522–525, 1993.

[34] B. W. Smith and D. E. Luzzi. Formation mechanism of fullerene peapods and coaxial tubes: a path to large scale synthesis. *Chem. Phys. Lett.*, 321:169–174, 2000.

[35] Y. Gogotsi, N. Naguib, and J. A. Libera. In situ chemical experiments in carbon nanotubes. *Chem. Phsy. Lett.*, 365:354–360, 2002.

[36] A. C. Dillon, K. M. Jones, T. A. Bekkedahl, C. H. Kiang, D. S. Bethune, and M. J. Heben. Storage of hydrogen in single-walled carbon nanotubes. *Nature*, 386:377–379, 1997.

[37] S. C. Tsang, Y. K. Chen, P. J. F. Harris, and M. L. H. Green. A simple chemical method of opening and filling carbon nanotubes. *Nature*, 372:159–162, 1994.

[38] M. Pinault, M. Mayne-L'Hermite, C. Reynaud, O. Beyssac, J. N. Rouzaud, and C. Clinard. Carbon nanotubes produced by aerosol pyrolysis: growth mechanisms and post-annealing effects. *Diamond and Related Materials*, 13:1266–1269, 2004.

[39] R Kozhuharova, M. Ritschel, I. Mönch, T. Mülh, A. Leonhardt, A. Graff, and C. M. Schneider. Selective growth of aligned Co-filled carbon nanotubes on silicon substrates. *Fullerenes, Nanotubes and Carbon Nanostructures*, 13:347–353, 2005.

[40] A. L. Elías, J. A. Rodríguez-Manzo, M. R. McCartney, D. Golberg, A. Zamudio, S. E. Baltazar, F. López-Urías, E. Muñoz Sandoval, L. Gu, C. C. Tang, D. J. Smith, Y. Bando, H. Terrones, and M. Terrones. Production and characterization of single-crystal FeCo nanowires inside carbon nanotubes. *Nano Lett.*, pages 467–472, 2005.

Chapter 4

In situ TEM modifications of MWNT-based nanostructures

4.1   Introduction

The Transmission Electron Microscope (TEM), a long-standing tool within the materials research community, is nowadays one of the most powerful instruments for the investigation of nanostructures. As with every experimental technique, there are some drawbacks for TEM. In particular, structural alterations of the sample by the electron beam irradiation can occur depending on the TEM acceleration voltage, irradiation intensity, exposure time and type of sample. The *in situ* modification of samples inside a TEM provides an excellent opportunity to observe transformations of materials at the nano-scale, and carbon-based nanostructures have been widely investigated using this technique. In the next sections, we describe the effects caused by electron irradiation in solids, concentrating mainly on carbon nanostructures. By heating carbon nanostructures under electron irradiation annealing of defects can occur, and this phenomenon is also analyzed. In this context, we will show experimental results, demonstrating various *in situ* TEM modifications of multi-walled carbon nanotubes (MWNTs) containing metal nanowires in their cores.

4.2   Electron irradiation effects in solids

When an electron, ion or neutron interacts with atoms, the incident particle is scattered either elastically (no loss of energy) or inelastically (measurable loss of energy). As a result of this interaction, the sample can be damaged either by energy or momentum transfer from the particle. When electrons are used as irradiation particles, the energy or momentum transfer between the electrons and the sample occurs through different mechanisms, which are summarized in the following list [1, 2]:

- electron-electron interactions,

- plasmons (collective electronic excitations),

- breakage of bonds or cross-linking,

- phonons (leading to heating of the target),

- displacement of atoms in the bulk of the target,

- sputtering of atoms from the surface,

- emission of photons (x-rays or visible light),

- emission of secondary or Auger electrons.

In a given irradiation experiment, the probability of occurrence of each type of interaction is dictated by the respective *cross section* σ, expressed in units of area (usually in barns, i.e., $10^{-28}m^2$). In order to estimate the contribution of each of these interactions to the overall damage produced on a sample under electron irradiation, besides cross sections, two things must be considered: *a*) the type of sample under irradiation and *b*) the energy of the electron beam. Insulators, semiconductors and metals react differently to distinct interactions, and cross sections show an electron-energy dependence. It is useful to separate the types of damage that these interactions can cause into two main groups: those that cause displacement of atoms in the target, known as *knock-on* effects, and those that do not cause displacement, known as *excitations* [1].

The excitation of phonons (oscillations where all the atoms in a crystal lattice vibrate collectively) leads to heating of the sample. Phonons generated by direct

collision with the nuclei of atoms at energy transfers in the meV range are less damaging than phonons generated by dissipation of plasmons or inelastic transitions such as Auger or X-rays with energy losses of < 0.1 eV. Good heat conductors are not damaged by phonons, but heat insulators (thermal conductivity $k < 0.1$ Wm^{-1}K^{-1}) can be severely damaged. For metals (or materials with $k > 100$ Wm^{-1}K^{-1}) beam heating is negligible under standard TEM conditions (acceleration voltages of 100–300 kV, and beam current densities of 10–20 A/cm^2). Core shell electrons in the target atoms can be displaced if more than a critical energy is transfered from the beam in an inelastic collision. The ejected electron leaves behind a hole in the inner shell of the atom, and the atom is left in an excited state (ionized). The atom returns to its ground state by filling the hole with an electron from an outer shell. This transition is accompanied by the emission of an X-ray or an Auger electron. Electronic excitations such as electron-hole pair generation or ionization can cause local rearrangement of atomic bonds, leading to bond breakage. This process in known as *radiolysis* and affects insulators and semiconductors [2]. Metals are immune to this effect because the instabilities are rapidly quenched by electrons from the conduction band.

Cross sections that measure inelastic interactions increase with the atomic number and decrease slowly with electron beam energy. In general, metals are not damaged by excitation processes under standard TEM conditions.

Displacement of atoms in solids occurs by knock-on collisions of electrons with the nuclei of atoms in the sample. A displaced atom leaves behind a vacancy and an interstitial, producing damage to the sample if recombination does not happen. Knock-on damage is directly related to the beam energy. The transfered energy T between an electron and an atom in a collision is given by

$$T = T_{\max} \cos^2 \theta,$$

where θ is the angle between the initial direction of the electron and the direction of the displaced atom, and T_{max} is the maximum energy transfer that occurs for a head-on collision ($\theta = 0$). By momentum conservation (relativistic regime), the

maximum energy transfer is given by

$$T_{\text{max}} = \frac{2ME(E + 2m_{\text{e}}c^2)}{(m_{\text{e}} + M)^2c^2 + 2ME}, \tag{4.1}$$

where m_{e} is the electron mass, M the mass of the atom nucleus, c the speed of light and E the energy of the electron. Considering that $m_{\text{e}} << M$ and that for the energy range available in TEM, $E << Mc^2$, Eq. (4.1) is reduced to

$$T_{\text{max}} = \frac{2E(E + 2m_{\text{e}}c^2)}{Mc^2}. \tag{4.2}$$

The minimum energy required to irreversibly displace a lattice atom is known as the threshold energy T_{thr}. In general, T_{thr} depends on the direction of the knock-on displacement with respect to the crystal lattice, having a lower value for directions where the atoms are displaced into open space areas like the region between graphene layers in graphite. By substituting T_{thr} in Eq. (4.2), the minimum electron energy E_{d} required to displace an atom is obtained. Knock-on displacements are not expected when electrons possess energies below E_{d}.

In an experiment, the quantity that is measured is the displacement rate p of each atom, expressed as

$$p = \sigma_{\text{d}}j \tag{4.3}$$

where σ_{d} is the *displacement cross section* and j the beam current density. If an isotropic T_{thr} is assumed, the total displacement cross section σ_{d} is given by [1]

$$\sigma_{\text{d}} = \frac{4Z^2E_{\text{R}}}{m^2c^4}\left(\frac{T_{\text{max}}}{T_{\text{thr}}}\right)\pi a_0^2\left(\frac{1-\beta^2}{\beta^4}\right)\left\{1 + 2\pi\alpha\beta\left(\frac{T_{\text{thr}}}{T_{\text{max}}}\right)^{1/2}\right.$$
$$\left. - \frac{T_{\text{thr}}}{T_{\text{max}}}\left[1 + 2\pi\alpha\beta + (\beta^2 + \pi\alpha\beta)\ln\left(\frac{T_{\text{max}}}{T_{\text{thr}}}\right)\right]\right\}, \tag{4.4}$$

where Z is the atomic number, E_{R} the Rydberg energy (13.6 eV), a_0 the Bohr radius (5.3×10^{-11} m), $\beta = v/c$, and $\alpha = Z/137$. From Eq. (4.4) it is clear that σ_{d} increases with increasing Z, but the energy transfer (Eq. (4.2)) behaves inversely with respect to the mass of the nucleus. Thus, the total σ_{d} depends heavily on the beam energy. For electron energies $E >> E_{\text{d}}$, a higher displacement rate p is expected for heavier atoms. Analysis of electron radiation damage should also consider the displacement of surface atoms (*sputtering*), which requires 50% of the E_{d} necessary for knock-on of an atom from the bulk [2], and *displacement cascades*, which occur when a displaced atom has sufficient energy to cause knock-on of neighboring atoms [1].

Knock-on is the primary mechanism by which metals are damaged under electron irradiation, since excitations are rapidly quenched.

4.2.1 Electron irradiation effects in carbon nanostructures

In order to understand the response of graphitic-type carbon nanostructures under electron irradiation, graphite could be used as a good starting model. The two-dimensional metallic character of graphite along its basal plane accounts for the metal-type response under electron irradiation. Like metals, graphite is primarily damaged by knock-on effects. Thus, excitations are not considered in the following discussion. Values of T_{thr} for graphite depend on the direction of the incoming electron with respect to the crystal lattice, being lower for displacements parallel to the c-axis than for in-plane displacements. Early experimental studies differ significantly in the T_{thr} for graphite, and Table 4.1 summarizes some of these values. For graphitic carbon nanostructures electron microscopy studies indicate that T_{thr} values of $\sim$ 15–20 eV parallel to the c-axis and $>$ 30 eV for in-plane displacements should be considered [1]. These values agree with that of the lowest reported graphite T_{thr}. In curved carbon nanostructures, where the angle between the incoming beam

Table 4.1: T_{thr} for graphite. Some authors give values for T_{thr} parallel and perpendicular to the c-axis of graphite and others only an average value. [a] *Carbon* 9, 179 (1971), [b] *J. Phys. Soc. Jap.* 31, 1761 (1971), [c] *Radiation Damage in Graphite* (Pergamon, Oxford, 1965), [e] *Physics of Graphite* (Applied Science Publications, London, 1981), [f] *Ultramicroscopy* 39, 361 (1991).

	Graphite T_{thr} (eV)		
	$\parallel$ c-axis	$\perp$ c-axis	Average
Montet *et al.*[a]	31-33	60	41
Iwata *et al.*[b]	28	42	33
Simmons [c]	-	-	25
Kelly *et al.*[e]	-	-	33
Nakai *et al.*[f]	-	-	12
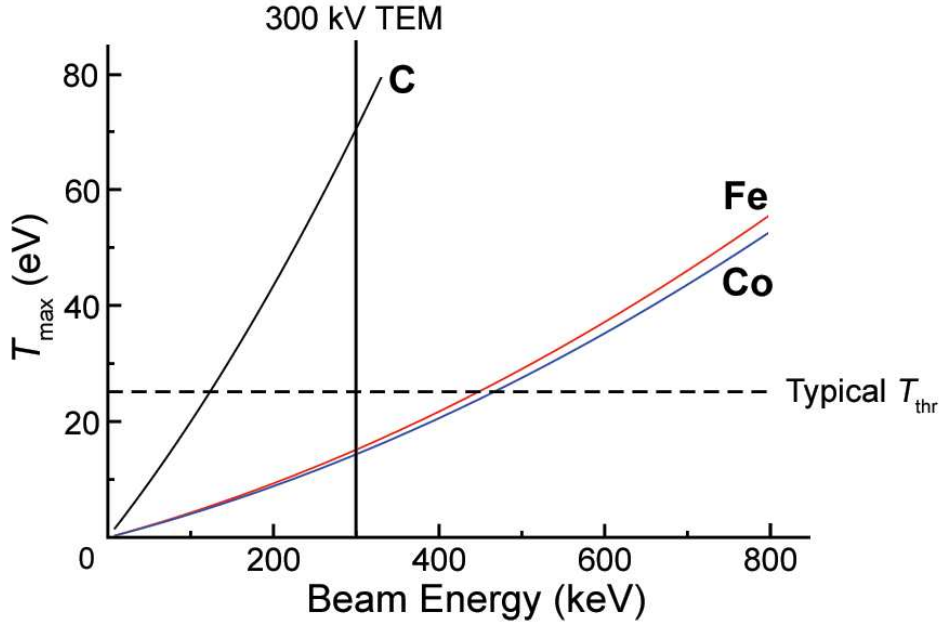
Figure 4.1: (Color) T_{max} as a function of beam energy. Plots for C, Fe and Co are shown. The dotted line (T_{max}= 25 eV) is a typical threshold energy for metals. The vertical line gives the maximum electron energy attainable in 300 a kV TEM.

and the c-axis of graphitic planes varies, it is a good approximation to take the T_{thr} of the direction of easiest displacement as a measure to estimate the behavior of the complete particle [1]. From Eq. (4.1), the E_d required to displace an atom of carbon, considering T_{thr} of 15–20 eV, is in the range $E_d = 76$–100 keV. These values are overestimated because no sputtering events or displacement cascades are considered. Experimental observation shows that for electron energies below 50–60 keV, no structural changes in graphite are observed [3].

From Eq. (4.2) T_{max} can be calculated as a function of electron energy E for different elements, and Fig. 4.1 shows the results for C, Fe and Co. Clearly, for a given beam energy, the T_{max} is lower for heavier atoms. Considering T_{thr} energies of 15, 24 [4] and 23 [2] eV for C, Fe and Co, respectively, from Fig. 4.1 it can be concluded that in a 300 kV TEM, atom displacements will occur for carbon nanostructures, but not for Fe or Co. Thus, in an irradiation experiment with electron energies < 600 keV involving a M@MWNT (where M = Fe, Co or Ni), the potential to damage the MWNT is greater than for the metal.

The σ_d for carbon atoms as a function of T_{thr} energy can be calculated from
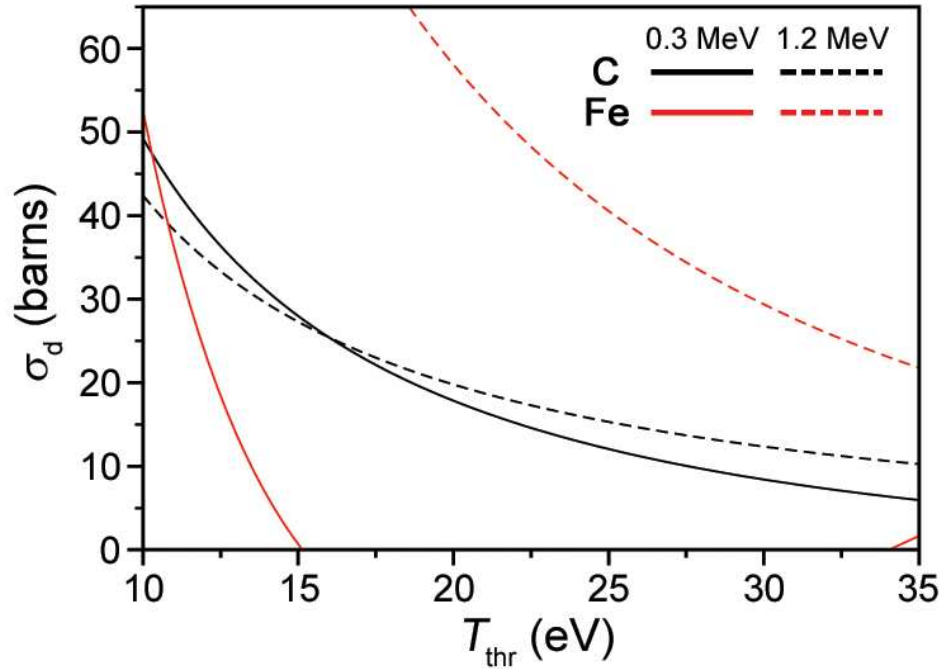
Figure 4.2: (Color) Displacement cross section σ_d as a function of T_{thr}. Plots for the σ_d of C and Fe at two distinct electron energies (300 and 1250 keV) are shown.

Eq. (4.4). Figure 4.2 shows the dependence of σ_d on T_{thr} for C and Fe at two different electron energies (300 and 1250 keV). Again, it can be seen that for values of T_{thr} of 15(C) and 23(Fe) eV, displacements of atoms is expected to happen for C and not for Fe in a 300 kV TEM. However, at higher voltages an increase in the σ_d of Fe with respect to C is expected. In a typical irradiation experiment, the beam current density is $j = 100$ A/cm². From Fig. 4.2, a value of $\sigma_d = 27.7$ barns is obtained for C ($T_{\text{thr}} = 15$ eV), considering a 300 keV electron energy. Therefore, from Eq. (4.3) a displacement rate of $p = 0.017$ displacements of each atom per second (dpa/s) is expected.

Electron irradiation induced displacement of atoms produces vacancies and interstitials point defects in the irradiated sample. Point defects can vanish by annihilation, when a vacancy and an interstitial recombine, or by aggregation of defects of the same kind (clustering). In addition, point defects can disappear through a sink such as a surface area or a preexisting structural defect, such as dislocations. The damage evolution caused by point defects depends on their formation and mi-

gration energies. The temperature has also a great influence on the migration rate of defects. The diffusion coefficient D of a vacancy or an interstitial is given by [5]

$$D = D_0 \exp(-E_\mathrm{m}/kT) \tag{4.5}$$

where D_0 is a temperature-independent coefficient, E_m the migration energy, k Boltzmann's constant and T is the temperature. Interstitials and vacancies have distinct associated E_m, generally with higher values for vacancies. Thus, vacancies are less mobile than interstitials at low temperatures.

Table 4.2 summarizes the formation and migration energies for graphite as taken from ref. [6], based on early experiments. The E_m of graphite for vacancies is high enough to prevent their movement at room temperature. Theoretical calculations predict an energy of 1.6 eV [7] for the ab-plane migration of vacancies, which is half the experimental value. The low value of E_m for graphite interstitials along the ab-plane, makes them mobile at room temperature. This value (< 0.1 eV) is assumed for free interstitials that form no bonds with atoms in the lattice. However, theoretical studies have predicted configurations where the interstitial forms covalent bonds with the lattice planes, raising the E_m up to 0.47 eV [8]. For di-interstitials, a $E_\mathrm{m} = 0.86$ eV has been estimated [9], still, an order of magnitude less than the E_m for vacancies. Thus, the evolution of defects is mostly dictated by interstitial migration. Irradiation of graphite at room temperature produces partial disordering of the atomic layers. Loss of structural coherence by fracture and tilting of the layers is accompanied by a large increase in the specimen length and the lattice parameter along the c-axis direction [10]. Such effects are explained by the agglomeration of

Table 4.2: Formation and migration energies for interstitials and vacancies in graphite. Migration energies are given parallel and perpendicular to the c-axis of graphite [6].

	Vacancy (eV)	Interstitial (eV)
Formation energy	7.0 ± 0.5	7.0 ± 1.5
Migration energy in ab-plane	3.1 ± 0.2	< 0.1
Migration energy $\parallel$ to c-axis	> 5.5	> 5
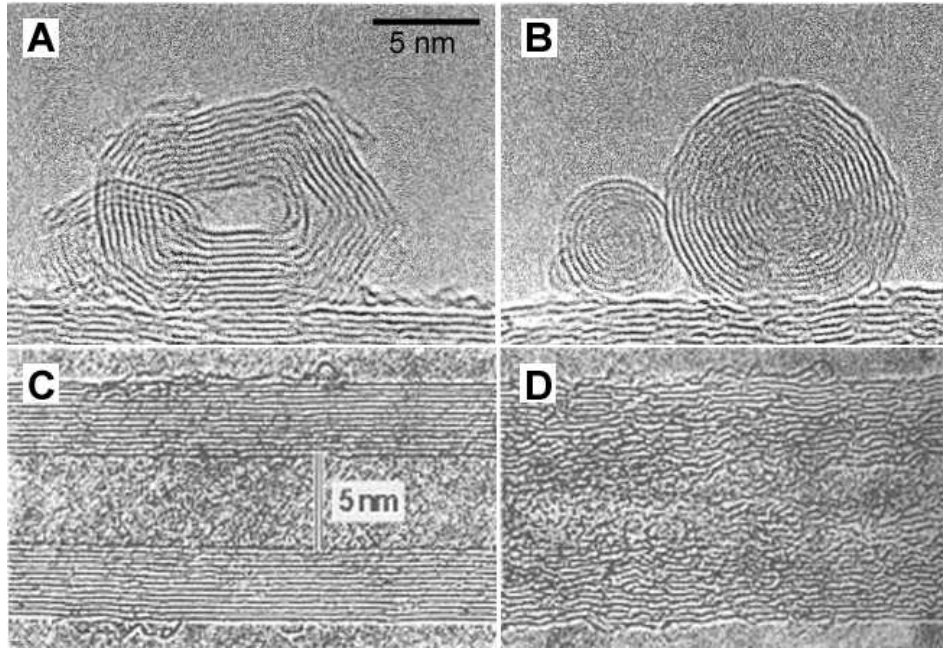
Figure 4.3: Polyhedral carbon particle before (**A**) and after (**B**) electron irradiation at room temperature [12]. MWNT before (**C**) and after (**D**) irradiation at room temperature, where disordering of the layers is observed. [3].

interstitials, which lead to dislocation loops [1].

One of the first carbon nanostructures produced with the TEM-induced modification method were carbon *onions*. The usual beam current density at a sample in a TEM is about 10–20 A/cm^2. Ugarte demonstrated that by irradiating polyhedral particles and tubular graphitic structures present in carbon soot, with high beam current densities (100–400 A/cm^2) in a 300 kV TEM at room temperature, severe structural transformations occur, thus transforming the particles into concentric spheres, resembling onions (Figs. 4.3A and 4.3B), exhibiting interlayer spacings of 3.34 Å [11, 12]. Carbon nanostructures under intense irradiation show the tendency of smoothening sharp edges and kinks [12, 3]. When irradiation is stopped, these structures decay into disordered graphitic material [1].

Single-walled carbon nanotubes (SWNTs) exposed to electron irradiation develop local deformations that lead to the shrinkage and complete fracture if the irradiation prevails [13]. However, if the electron dose is mild (0.1–1 A/cm^2), the SWNT response is atom loss (knock-on process) via surface reconstruction and diameter reduction, as shown by Ajayan *et al.*; they irradiated a 1.4 nm diameter

SWNT in a 200 kV TEM and observed a diameter reduction down to 0.4 nm, before complete rupture of the tube [14]. For SWNTs, T_{thr} decreases with diameter, and for diameters < 1 nm, T_{thr} drops quickly down to ~ 7 eV [15]. MWNTs under electron irradiation at room temperature develop structural changes similar to those observed in graphite (Fig. 4.3C and 4.3D). The tube walls, parallel planes (002) observed normally in High Resolution Transmission Electron Microscopy (HRTEM), become disordered and the hollow part is reduced with time, until it finally collapses [16, 17].

4.2.2 Thermal annealing of defects induced by electron irradiation

The damage induced in carbon nanostructures by electron irradiation at room temperature is inhibited if the sample is heated above 300–400°C during irradiation [3, 18]. This effect becomes more prominent at temperatures > 500°C. For example, the disordering of the basal planes observed at room temperature irradiation (Fig. 4.3D) is absent, and coherent, undistorted layers of high tensile stability are observed instead. Defects are annealed out due to thermally activated diffusion of interstitials, which enables the recombination of interstitials and vacancies, thus resulting in annihilation of defects. This process is accompanied by loss of mass, via sputtering of carbon atoms. Carbon tubes and onions experience diameter reduction and continuous shrinkage [3]. From Eq. (4.5), diffusion rates of defects can be estimated. Table 4.3 shows the diffusion rates D of free, bound and di-interstitials with respect to diffusion at room temperature D_{RT}, for temperatures of 300 and 600°C. Interestingly, a small change in diffusivity is observed for free interstitials even at 600°C, thus these atoms cannot account for the annealing effects observed. In fact, the existence of significant quantities of these species should be discarded. For bound and di-interstitials, a significant increase of D is seen in the region of interest. A change of six-orders of magnitude for D is obtained for di-interstitials already at 300°C. Therefore, the annealing kinetics is dictated by thermal diffusion of bound and di-interstitials parallel to the basal planes that recombine with less mobile vacancies [3].

Table 4.3: Diffusion rates D of interstitials with respect to D_{RT} for 300 and 600°C. The migration energies are for free (0.1 eV), bound (0.47 eV) and di-(0.86 eV) interstitials.

E_m (eV)	D_{300}/D_{RT}	D_{600}/D_{RT}
0.1	6.3	12.7
0.47	5.8×10^3	1.5×10^5
0.86	7.6×10^6	3.0×10^9

Carbon onions formed at room temperature irradiation show structural defects such as rupture of planes and dislocations loops (Fig. 4.3B). When carbon onions are irradiated and heated simultaneously, they show almost perfect spherical symmetry (Fig. 4.5A), because of defect annealing. These tensile coherent shells slowly lose atoms from sputtering and knock-on displacements and reconstruct around single or multiple vacancies by the incorporation of polygons other than hexagons, as shown in Fig. 4.4, where only the outermost shell is depicted for clarity [19]. The shells shrink, exerting pressure on the interlayer spacings. Shrinkage is observed as a decrease of the distance between shells from 0.31 nm close to the surface down to 0.22 nm at the center of the onion [20]. This self-compression effect is dramatic in onions, observed in the nucleation of cubic diamond crystals in their cores. In a 1250 kV TEM, Banhart and Ajayan [20] irradiated carbon onions placed on a heating stage (650–750°C) with a beam current density of 200 A/cm^2 and observed, after approximately one hour of irradiation, the nucleation and growth of diamond crystals in the core of the carbon onions (Fig. 4.5A). These observations lead to a value of 50–100 GPa for tensile stress within the layers. Thus, under certain
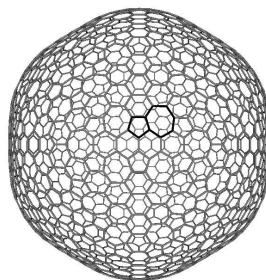
Figure 4.4: Outermost shell of a carbon onion. The sphericity is provided by the incorporation of additional 5MR and 7MR into the atomic lattice, like the ones highlighted in black [19].
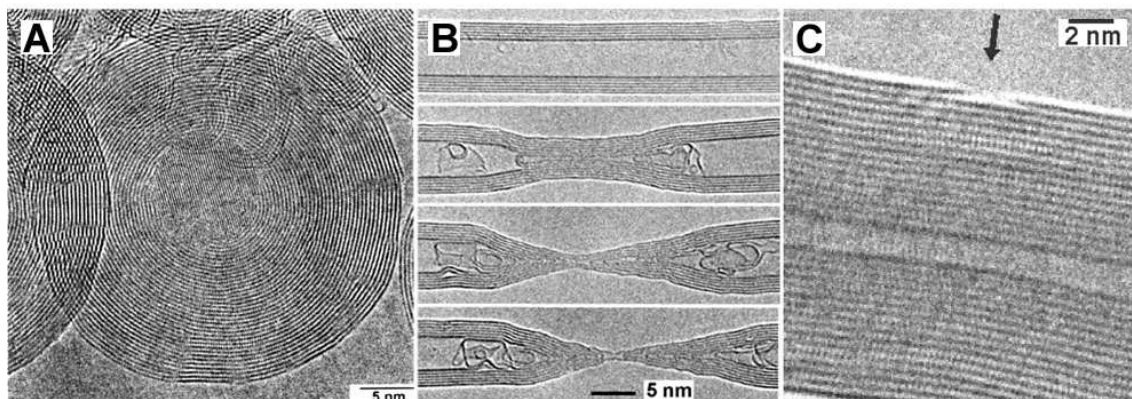
Figure 4.5: TEM *in situ* experiments on carbon nanostructures. (**A**) Carbon onion under electron irradiation at 730°C; a diamond crystal is formed at the core of the onion [20]; (**B**) morphological evolution of a MWNT under electron irradiation at 600°C [15], and (**C**) removal of material from the outermost layer of a MWNT, to create a hole (arrowed), with a focused electron beam [21].

experimental conditions, carbon onions act as pressure cells. The compression of carbon onions is driven by irradiation and defect kinetics at high temperatures, since no external forces are present. At room temperature irradiation neither a decrease in the distance between layers nor the formation of diamond in the core of carbon onions is observed [3].

At high temperatures, SWNTs remain stable under irradiation even at energies of 1.25 MeV and beam current densities of 200 A/cm^2 [3]. The stability is driven by interstitials that are able to migrate along the single layer and quickly anneal defects. Migration energies for single vacancies drop with diameter size for SWNTs, and vacancies can migrate toward sinks or form vacancy clusters, already, at temperatures of 100–200°C [22]. Surprisingly, the formation energy of a di-vacancy in SWNTs is lower than that of a single vacancy; thus di-vacancy formations are favored. Di-vacancies are reflected in SWNTs as local buckling, diameter reduction and local re-arrangement of the atomic network [23]. MWNTs irradiated and heated at the same time also collapse, as at room temperature irradiation, but during shrinkage there is no breakage or severe amorphization of the shells. The innermost layer of the MWNT is the first to break, and the disruption continues from inner to outer layers, until the outermost layer ultimately breaks (Fig. 4.5B). The complete transforma-

tion shows that it is more likely that the generated carbon interstitial atoms leave the irradiated zone by diffusion through the hollow core of the MWNT, because the diffusion barrier is higher for atoms outside the layers [15].

With a focused electron beam, modifications on carbon nanotubes (CNTs) can be tailored with high precision. The transformation from a SWNT-bundle into a MWNT [21], the formation of small holes (< 2 nm) on the outermost layer of a MWNT (Fig. 4.5C) and the cutting of a bundle of SWNTs [24] are some examples of the precise manipulation that can be achieved with an electron beam at high temperatures.

4.3 Experimental conditions

Electron irradiation experiments were carried out in a FEI Tecnai F-30 with a field emission gun TEM operating at 300 kV. For the study of MMWTs containing metal nanowires (see section 3.8) a suspension of MWNTs in ethanol was dispersed ultrasonically in a sonication bath. A drop of the suspension was deposited onto a TEM grid (Cu, Mo or holey carbon). Copper grids are preferred for heating experiments to avoid vibrations, since heat is conducted better from the hot-bath to the sample under observation. The samples were mounted in a special-equipped TEM heating holder (Philips or Gatan), that allows temperatures up to 800°C. Irradiation experiments were carried out at 600°C, unless stated otherwise. The samples were irradiated with electron doses of 40–10^4 A/cm^2, depending on the beam diameter. The beam current density scales as the inverse square of the beam diameter when controlled by the second condenser lens in the TEM [21].

4.4 MWNTs as high pressure cells and nanoextruders

MWNTs shrink in an ordered manner when irradiated at high temperatures (Fig. 4.5B). Though, one may ask the following question: what happens if instead of empty volume there is material contained inside the MWNT? In order to address

this question, electron irradiation experiments were carried out on thin MWNTs containing encapsulated metal (Co, Ni, Fe, FeCo) or carbide (Fe_3C) nanowires (see section 3.8). The mechanical properties of CNTs have been studied both theoretically [25] and experimentally [26] for tensile and bending forces, but their strength against internal pressure remains unexplored. In this section, it is shown that controlled irradiation of MWNTs causes pressure buildup within the nanotube cores, which can plastically deform, extrude and even break solid materials that are encapsulated inside their cores. Theoretical studies estimate that the internal pressure of MWNTs could reach values higher than 40 GPa. This effect is similar to the one observed in closed-shell carbon onions that can act as self-contracting high-pressure cells under electron irradiation [20]

4.4.1   Experimental observations

Electron irradiation of MWNTs at room temperature causes disordering and breakage of the layers (Fig. 4.3D). Figure 4.6 shows this effect, differing only in the presence of a metal nanowire contained in the area of interest. For this experiment a FeCo@MWNT was irradiated at room temperature with a beam current density of 200 A/cm^2. Figure 4.6A shows the MWNT at the beginning of the irradiation experiment as well as its Fast Fourier Transform (FFT), where the order of the carbon layers is observed as two well defined spots. The 16 layer MWNT, the empty hollow core (diam.= 8.4 nm) and a segment of the nanowire are clearly resolved. After 147 seconds of irradiation, the diameter of the hollow core has decreased (diam. = 4.7 nm), and the inner most layer shows disorder (Fig. 4.6B). After 269 seconds, the tube has collapsed, and a clear amorphization is observed in the outer most layers (Fig. 4.6C). The amorphization process continues with further irradiation, and this can be monitored with the FFT that shows two smear regions instead of well defined spots (inset Fig. 4.6D). It is important to note that no important structural changes in the metal nanowire are observed.

MWNTs simultaneously irradiated and heated not only self-anneal structural defects of tube walls, but as the diameter shrinks (because of loss of mass) a buildup of pressure within the cores occurs that can deform encapsulated materials. This
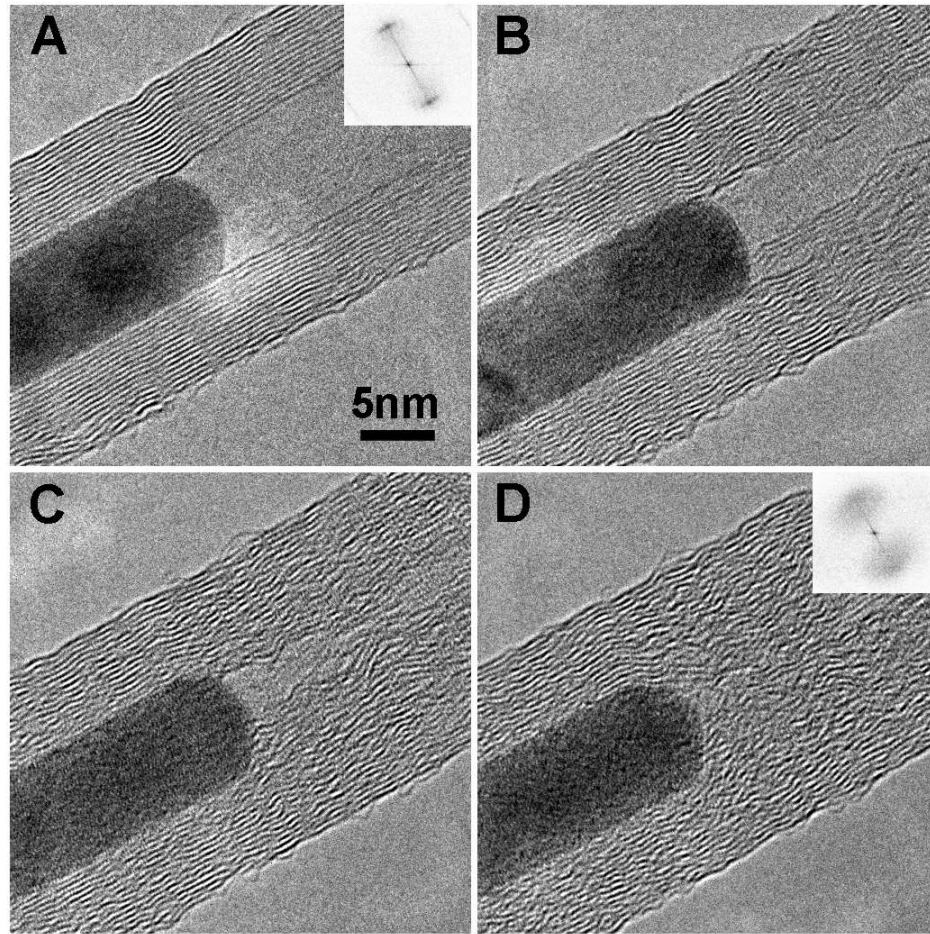
Figure 4.6: Electron irradiation of a FeCo@MWNT at room temperature. (**A**) The FeCo@MWNT at the beginning of the experiment. Graphitic lattice planes (002), a hollow core portion and the metal nanowire are clearly resolved. The inset shows the FFT of the image. The collapsing tube for irradiation times of (**B**) 147, (**C**) 269 and (**D**) 421 seconds (FFT of the image in the inset). Image courtesy of Dr. Litao Sun.

striking difference with respect to room temperature irradiation is shown in Fig. 4.7. A Co@MWNT was irradiated at 600°C with a beam current density of 260 A/cm^2. The MWNT has 19 layers, and the Co nanowire (*fcc* structure) has a diameter of 3.7 nm at the initial stage of the experiment (Fig. 4.7A). Deformation of the Co nanowire can be monitored inside the collapsing MWNT after 120 seconds of irradiation (Fig. 4.7B). While the tube collapses, the Co crystal slides in the axial direction which can be seen by taking the small particle on the surface of the tube (left hand side Figs.4.7A and B) as a reference point. The Co nanowire gets thinner and experiences deformation, but no apparent crystallographic defects appear. After
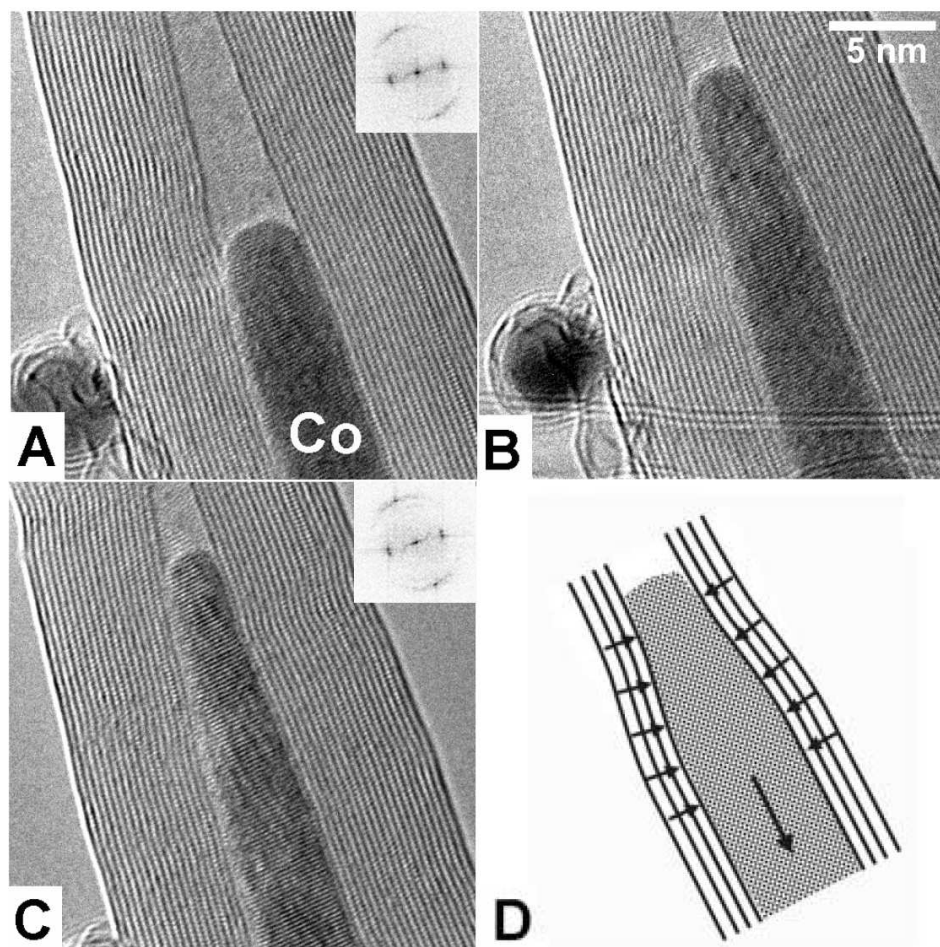
Figure 4.7: Electron irradiation of a Co@MWNT at 600°C. Deformation of a Co nanowire inside a collapsing MWNT for irradiation times of (**A**) 120, (**B**) 240 and (**C**) 360 seconds. (**D**) Simplified geometry of the system. Compressive forces (small arrows) from the MWNT shells lead to a thinning of the crystal and its sliding along the tube axis (large arrow) [27].

240 seconds of irradiation, the diameter of the Co nanowire has reduced down to 2.2 nm at its topmost part. The FFT stills shows bright spots for the MWNT as well as for the nanowire, demonstrating that no disorder is present in the tube structure (Fig. 4.7C). Figure 4.7D shows a simplified diagram of the system. Compressive forces from the tube shells lead to a thinning of the crystal and its sliding along the tube axis.

The extent to which a material contained inside a MWNT can be deformed is illustrated in Fig. 4.8, in which a Fe_3C@MWNT is irradiated with a beam current of 200–400 A/cm^2 (beam diameter $\sim$ 60 nm). Irradiation of the section at the end of the nanowire leads to a non-uniform collapse of the tube, and the hollow part
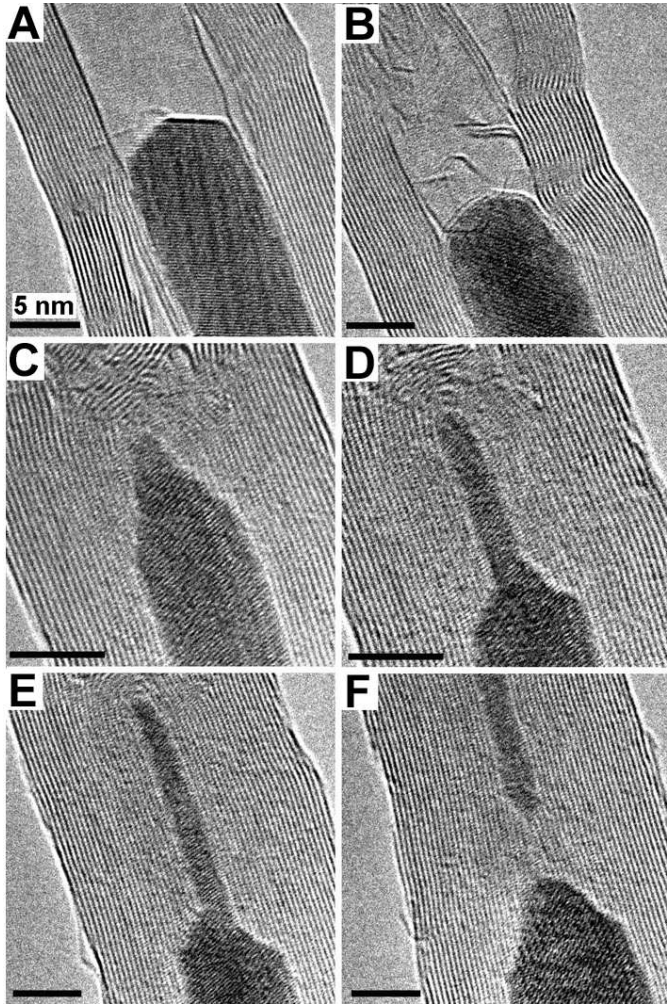
Figure 4.8: Fe$_3$C@MWNT sample under electron irradiation. (**A**) Sample at the beginning of the experiment; (**B** to **E**) irradiation lead to a collapse of the MWNT and extrusion of the crystal, and (**F**) the collapsed tube cuts off the thinned crystal nanowire [27].

of the tube fills up with graphitic material (Fig. 4.8B). After further irradiation, carbon material that migrates from the open side of the tube core aggregates at the end of the Fe$_3$C nanowire by closing the inner hollow with graphene layers, and this is observed as a local increase in the number of layers. The collapsing tube clearly deforms the carbide crystal (Figs. 4.8C, D and E). The diameter of the nanowire decreases from 9 to 2 nm in the extrusion process, and the final collapse of the MWNT pinches and cuts off the thinned nanowire (Fig. 4.8F). The rest of the nanowire continues moving downward. The total irradiation time in this sequence was 50 minutes.

The complete modification process that an encapsulated nanowire undergoes is shown in Fig. 4.9 at low magnification for a FeCo@MWNT that was irradiated for two hours with a beam current of ~ 40 A/cm^2. The length variation of the nanowire with time shows that the nanowire experiences different modification stages with
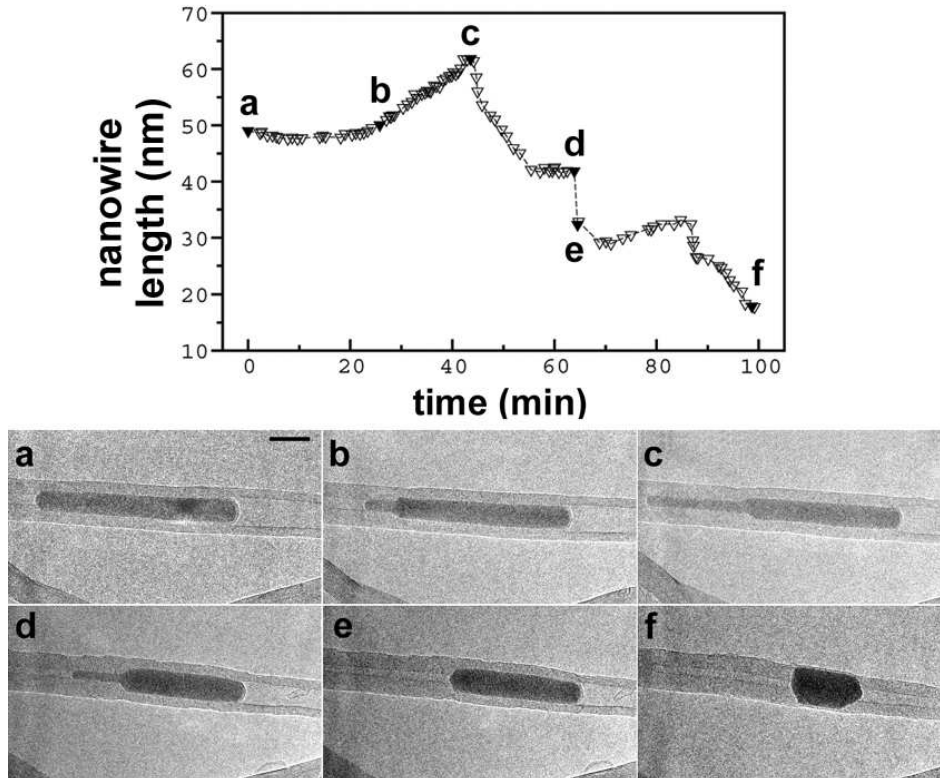
Figure 4.9: The graph shows the length of an encapsulated FeCo nanowire as a function of time of irradiation. Images for representative points (dark triangles) of the complete evolution are shown below (scale bar: 10 nm).

the evolution of the surrounding tube walls. At the beginning of the experiment (points (a) and (b) in Fig. 4.9) the variation in length is of approximately 1 nm. Then, for about 20 minutes, the nanowire is steadily extruded, up to a maximum length of 61 nm (point (c)), which is approximately 1.3 times the original one (48 nm). As the inner layers of the tube start to disintegrate, the crystal is modified by minimizing the surface area, which is observed as a contraction (points (c) to (d)). The discontinuity that appears at point (d) occurs because the thin part of the nanowire is pinched off, reducing drastically the length. Surprisingly, the sliced fragment moved away from the irradiated area, apparently without restriction. The process repeats until finally there are no more tube walls to exert pressure (point (f)) after ~ 100 minutes of irradiation, and the structure's last configuration looks like a MWNT-metal-MWNT junction (see section 4.6).
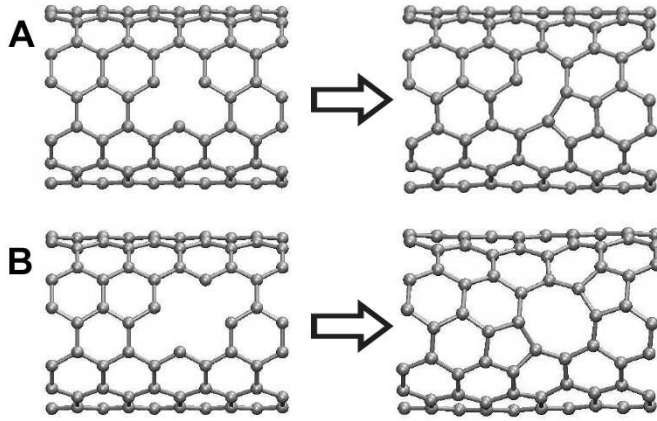
Figure 4.10: Lattice reconstruction of a single and a di-vacancy in a (6,6) SWNT. (**A**) Original non-reconstructed single vacancy, and lowest energy configuration. (**B**) Original non-reconstructed di-vacancy, and lowest energy configuration. [22]

4.4.2   Mechanism of pressure buildup

Theoretical simulations have provided some insight related to the MWNT contraction mechanism and the pressure buildup process inside the contracting tubes [27]. Since the T_{thr} for metals and carbides is higher than for MWNTs (at 600°C and a TEM voltage of 300 kV), it can be safely assumed that vacancies and interstitials are generated only in the carbon tube. Interstitial-vacancy pairs at 600°C tend to annihilate, and single vacancies are mobile to create di-vacancies, which have a formation energy less than that of single vacancies [22]. Vacancies in CNTs generate a strong reconstruction of the atomic lattice (Fig. 4.10). In Fig. 4.10A, it can be seen that in the stable configuration for a single vacancy a dangling bond is left (one carbon atom has only two neighbors), thus perfect reconstruction of the lattice is not possible. However, for di-vacancy reconstruction, all carbon atoms have three nearest neighbors, satisfying all bonds (Fig. 4.10B). This is achieved by the incorporation of two pentagonal and one octagonal ring in the lattice and is the reason why the di-vacancy configuration is energetically favorable over the single vacancy configuration. Once formed, di-vacancies are practically immobile ($E_{\text{m}} > 5$ eV) [22]. Thus, it is assumed that di-vacancies are responsible for the tube contraction.

Figure 4.11A shows a cross section of the studied model where the contraction of the MWNT is indicated by the small arrows. The theoretical study, based on a non-orthogonal density functional theory-based tight-binding (DFTB) method [28], considers that the forces acting on the shells are functions of shell radii and inter shell-spacing. Shell radii in turn depends on di-vacancy concentration n, where the
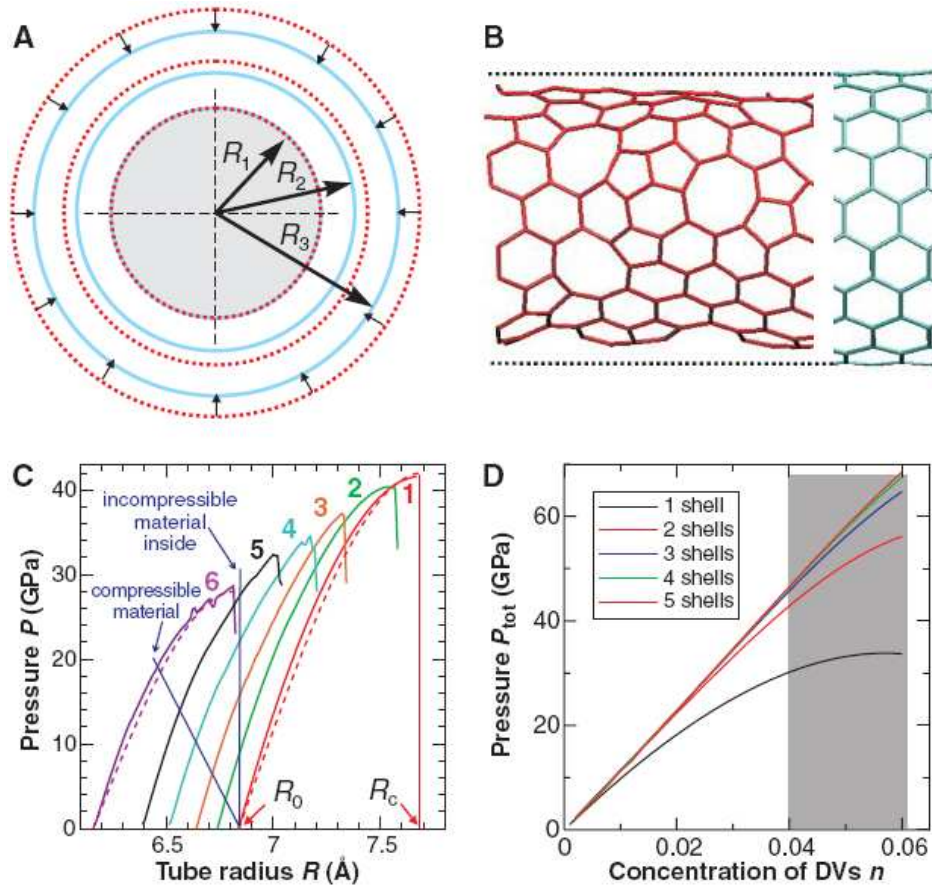
Figure 4.11: (Color) Mechanism of pressure buildup within an irradiated MWNT. (**A**) Cross section of a contracting MWNT (indicated by the small arrows). Dashed (red) circles indicate the pristine tube and solid (blue) circles, the tube after contraction . The inner core is filled with an incompressible material. Shell radii (R) are indicated by vectors. (**B**) A (10, 10) SWNT without (right) and with (left) double vacancies ($n = 0.05$). (**C**) Pressure versus tube radius for different di-vacancy concentrations n. Curve 1 corresponds to $n = 0$, 2 to $n = 0.007$, 3 to $n = 0.018$, 4 to $n = 0.028$, 5 to $n = 0.039$, and 6 to $n = 0.061$. The straight blue lines illustrate the determination of pressure inside a SWNT filled with incompressible and compressible material; the intersection of the blue lines with the curves gives pressure for the corresponding di-vacancy concentration. (**D**) Pressure inside tubes with different number of shells as a function of n (DVs n, di-vacancy concentration n) [27].

concentration n is defined as half the ratio of missing atoms to the number of atoms in the pristine tube. The structural change expected for a tube under irradiation is shown in Fig. 4.11B for a (10,10) SWNT. The average equilibrium radius $R_0(n)$ of the empty tube decreases linearly with n. The pressure exerted by a SWNT (i.e., the inner shell) is considered first, for clarity. As the filling of the tube should increase

R with respect to $R_0(n)$, numerically the pressure P was calculated as the derivate of the total energy with respect to R for $R > R_0(n)$. For all n, P increases linearly with R to a point where a nonlinear regime appears. Finally, when the bonds near vacancies start to break at the critical value $R_c(n)$, P abruptly drops. Figure 4.11C shows the pressure P inside a (10, 10) SWNT as a function of nanotube radius R for various n. The maximum pressure inside a SWNT for any n can be estimated from the $P(R)$ curves. For an incompressible material inside the core, the maximum P as a function of n is defined by the intersection of the vertical line drawn at the radius of the intact tube with the corresponding $P(R)$ curve. The pressure inside a SWNT as a function of n is shown in Fig. 4.11D (one shell). If the tube is filled with an incompressible material, there exists an upper limit on pressure, because for a given concentration of defects the tube will break. This shows that the pressure inside a single shell can be as high as 20 GPa.

An analytical approach previously used in a model of contracting graphitic shells in carbon onions [29] was used to estimate the total pressure P_{tot} inside MWNTs composed of two or more shells. The P_{tot} in the inner core of MWNTs filled with an incompressible material is shown in Fig. 4.11D for various numbers of shells. P_{tot} increases as the number of shells increases, but the pressure saturates quickly and pressure changes are not observed when the number of shells exceeds 6. Pressure values of 40 GPa or higher are expected for MWNTs.

4.5 Carbon nanotube growth

As mentioned in chapter 3, there have been numerous advances in the production of CNTs and nanofibers using the chemical vapor deposition (CVD) approach. However, the precise growth control of CNTs with desired chiralities and diameters is still an open challenge. For this reason, a better understanding of the carbon diffusion mechanism by which CNTs form from catalyst particles of transition metals is particularly important in CNT research.

In order to elucidate the nanotube growth process various experimental efforts have been carried out, and *in situ* observations of CNT growth (based on the CVD

process) have been reported by several groups [30, 31, 32, 33]. The environmental transmission electron microscope (ETEM) technique has been the dominant method, because it permits atomic resolution observations of gas-solid interactions. The growth of carbon whiskers [31], carbon nano-cages [32], MWNTs [31, 33] and SWNTs [32, 33] has been observed in the ETEM by the decomposition of hydrocarbons over supported nickel nanocrystals at temperatures in the range of 450–750°C.

In the ETEM approach, as in the CVD process, nanotube growth requires the presence of a gaseous hydrocarbon source, such as CH_4 or C_2H_2. In this section, the formation of SWNTs and MWNTs in a condensed phase process that does not involve the presence of a gaseous source of carbon is shown. This is achieved by electron irradiation of MWNTs containing transition metal particle cores (Co, Fe, FeCo) at 600°C. Carbon atoms are injected into the catalytically active metal particles by knocking carbon atoms from graphitic shells surrounding the metal crystals. The process has been monitored at atomic resolution in the TEM and the observations indicate that in this case bulk diffusion of carbon atoms through the body, rather than migration over the surface of the catalytic particle, takes place.

4.5.1   SWNT growth

The growth of a SWNT from an encapsulated Co nanowire (*fcc* structure) is shown in Fig. 4.12. Irradiation was carried out with an electron beam intensity of ∼ 100 A/cm². The encapsulated Co nanowire before nanoutube growth shows a flat surface at the top, apparently with no graphene layers (Fig. 4.12A). After 345 seconds of irradiation, a capped SWNT of 2.8 nm in length protrudes from the Co wire with what looks like a perfect hemisphere (Fig. 4.12B). The SWNT keeps growing as the irradiation continues (Figs. 4.12C and D). During the experiment, the Co crystal shrinks in the axial direction due to diffusion of Co atoms through the carbon shells under irradiation. This effect, that has already been observed [35], does not seem to influence tube growth, as other examples show (see below).

The number of carbon atoms that are displaced from the host tube to the metal particle can be estimated as follows. Equation (4.3) gives the displacement rate per atom. For $j = 100$ A/cm² $= 6 \times 10^{24}$ electrons/m²s, and $\sigma_{\mathrm{d}} = 2.8 \times 10^{-27} \mathrm{m}^2$
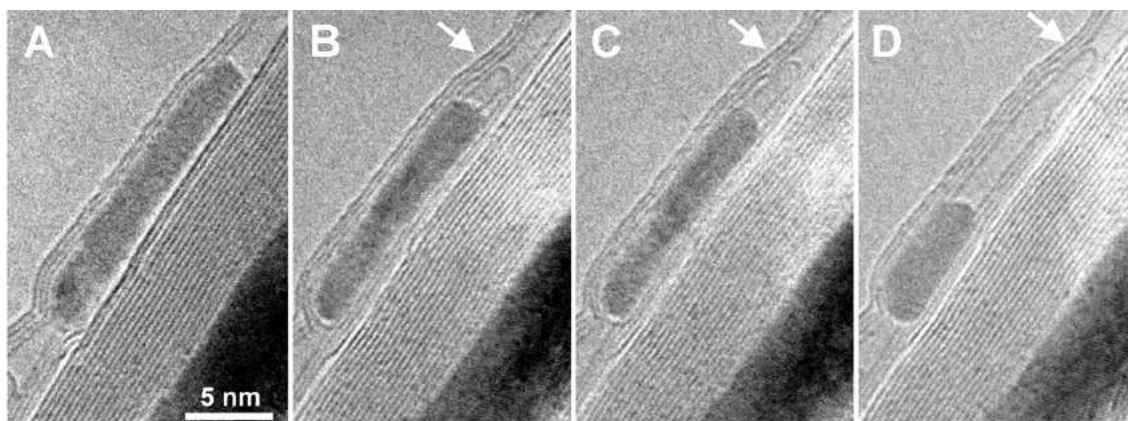
Figure 4.12: Growth of a capped SWNT from a Co crystal inside a host tube. The specimen temperature is 600°C during irradiation (intensity ~ 100 A/cm^2). (**A**) The Co@MWNT at the beginning of the experiment (the host nanotube is sitting on a larger Co@MWNT); (**B**) after 345 seconds of irradiation the nucleation of a capped SWNT is clearly seen (arrowed). The growth continues for (**C**) 408 and (**D**) 475 seconds of irradiation [34].
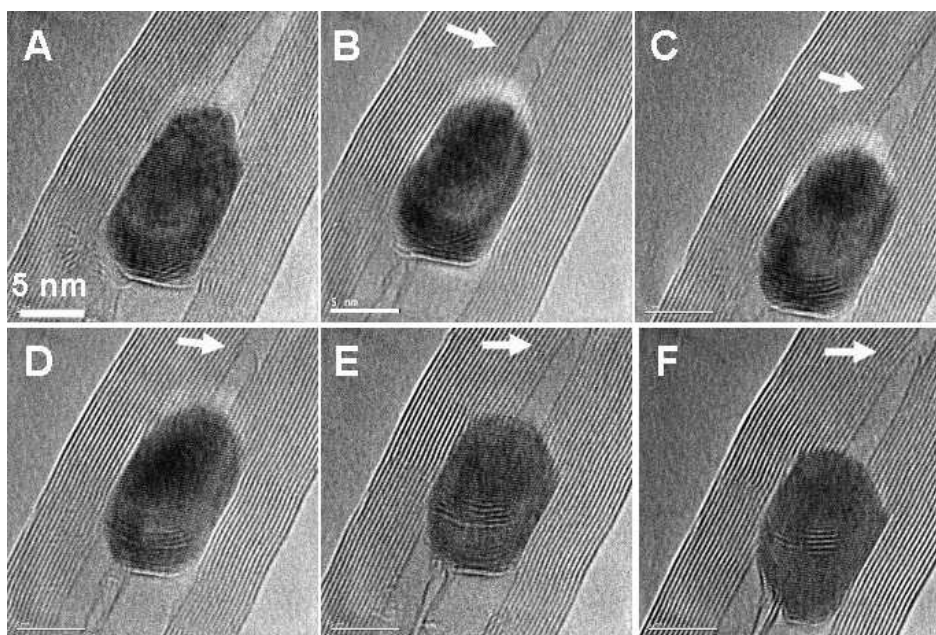
Figure 4.13: Growth of a SWNT inside a Fe@MWNT under electron irradiation (about 200 A/cm^2 in intensity) at 600°C. Arrows show the tip of the growing SWNT. (**A**) At the initial stage of growth a cap with one carbon layer forms at the tip of the Fe crystal. (**B**) After 5 minutes of irradiation a SWNT of 3.1 nm in length appears at the top of the crystal. The growth proceeds slowly for (**C**) 6, (**D**) 7, (**E**) 13, and (**F**) 15 minutes of irradiation [34].

(considering $T_{thr} = 15$ eV), a displacement rate value of $p = 0.017$ displacements per C atom in one second is obtained. Assuming (from geometrical considerations) that roughly 25% of all ejected carbon atoms reach the Co core, approximately 55 C atoms should be injected into the Co nanowire per second, if a density of 45 atoms/nm^2 is considered for the walls' atomic network. From these 55 C atoms, some might diffuse back to the carbon shells and recombine with vacancies. The rest are expected to diffuse towards both ends of the nanowire. The surface area ratio between the nanowire end faces and the cylindrical surface (waist) is of ca. 0.07. Since the growth takes place only on one of the end faces, an estimated 3.5% of all injected atoms might reach the end face where growth takes place. Therefore, approximately 2 C atoms per second can contribute to SWNT growth. The diameter of the SWNT in Fig. 4.12 is roughly 1 nm. This corresponds to approximately 140 C atoms per nm in length. With a feed of 2 C atoms per second the expected growth speed is of 1 nm per minute. On average, the growth speed in Fig. 4.12 is ca. 1.4 nm/min, which is in close agreement with the expected value.

SWNT growth was also observed inside a Fe@MWNT, as shown in Fig. 4.13. Here, the particle does not slide in the opposite direction during growth. In this example, a domain inside the metallic core, which appears to exhibit three or four layers, is observed; probably, this is a carbidic domain (Fe$_3$C). As the tube grows, the domain moves from the bottom of the particle (Fig. 4.13B) in the upward direction (Fig. 4.13F), seemingly coupled to tube growth at the top part of the particle. The surrounding Fe crystal remains in the *fcc* phase. There is a possibility that this migration domain is an artifact, such as Moiré fringes or some nanostructure outside the central core. However, the fact that the domain exhibits and retains a fringe pattern with a contour similar to the end of the particle from which the domain starts its migration is consistent with the bulk migration explanation.

4.5.2 MWNT growth

Besides the formation of SWNTs, the growth of MWNTs was also witnessed. Figure 4.14 shows a portion of a MWNT partially filled with a FeCo nanowire from which a MWNT grows. Irradiation was carried out with an electron beam intensity
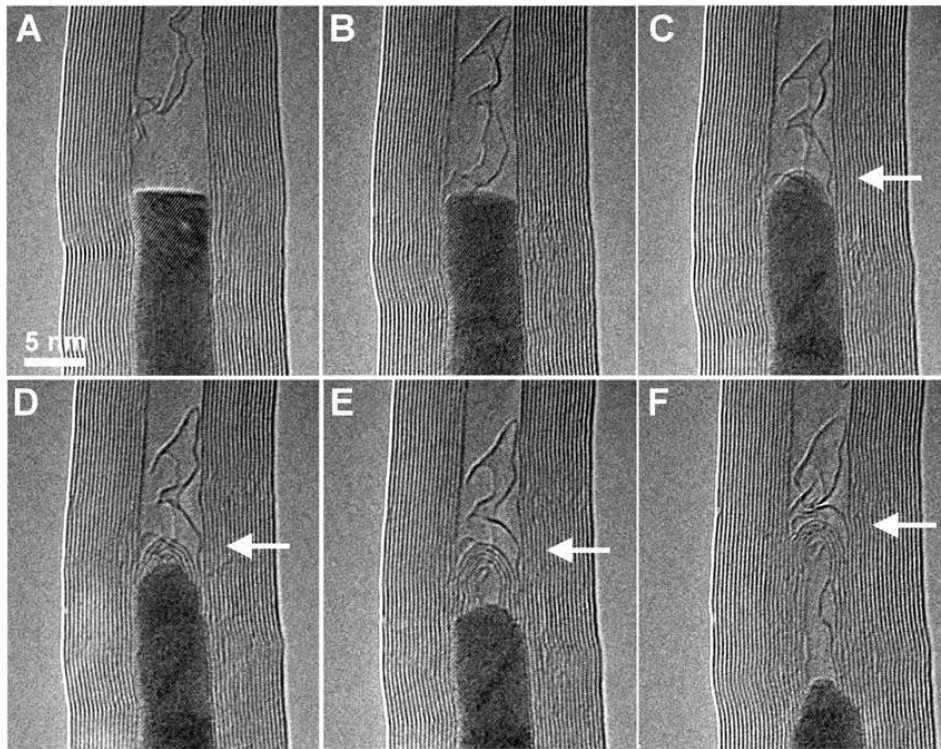
Figure 4.14: Growth of a MWNT from a FeCo nanowire inside a larger host nanotube under electron irradiation (intensity: 50–120 A/cm^2) at 600°C. (**A**) At the beginning of the experiment the end face of the nanowire is flat, and a graphitic sheet appears in the hollow core of the tube; (**B**) after 360 seconds of irradiation the graphitic material touches the nanowire end face; (**C**) after 386 seconds the initially flat nanowire surface has rounded off and it is completely cover by a graphene layer; (**D**) after 411 seconds of irradiation a new tube (arrowed) starts to grow while the FeCo slowly slides downward. The MWNT continues to grow for (**E**) 420 and (**F**) 502 seconds of irradiation. At this point a five-layer MWNT of 13 nm in length is clearly visible [34].

of 50–120 A/cm^2. Fig. 4.14A shows the 17 layer MWNT host at the initial stage of the experiment; the metallic nanowire clearly shows the (110) lattice fringes (*bcc* structure) and a flat end face. The highly misshapen graphitic filaments at the central hollow core seem to be due to the sputtering of carbon under irradiation from the inner wall. After 360 seconds of irradiation, carbonaceous material starts to aggregate close to the nanowire surface and attaches to it (Fig. 4.14B). As soon as the nanowire surface is completely covered by a graphene layer (386 seconds), the initially flat surface deforms into a round shape and develops steps (Fig. 4.14C). Almost immediately, after 411 seconds of irradiation, three more dome shaped car-
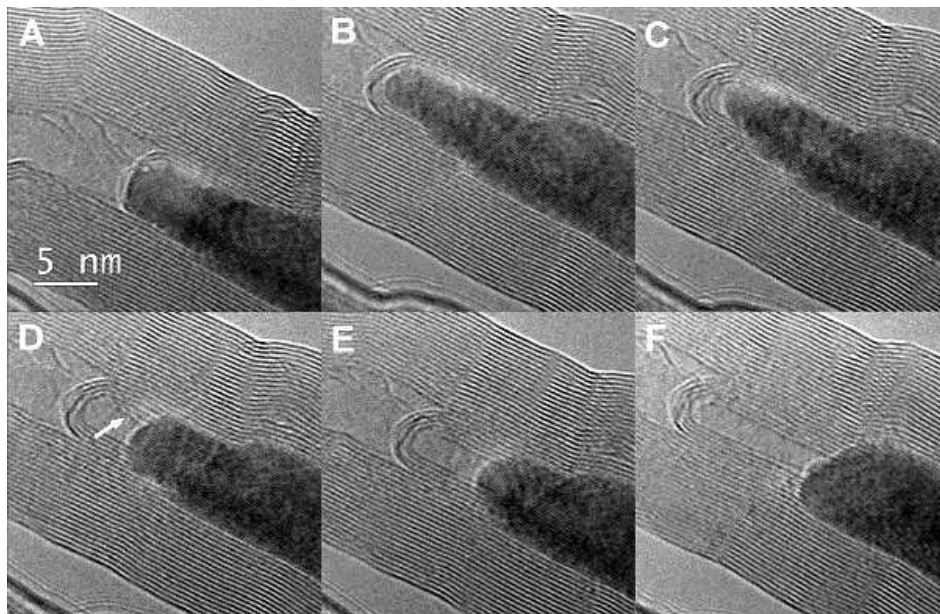
Figure 4.15: Growth of a MWNT from a Co nanowire under electron irradiation (intensity: 150 A/cm^2) at 600°C. (**A**) Two graphene layers cover the end face of the Co crystal after a period of irradiation; (**B**) after 50 seconds further of irradiation, the number of graphene sheets covering the end face increases to three; (**C**) after 90 seconds a four layer MWNT starts to grow while the Co crystal deforms; (**D**) after 145 seconds, an open graphene filament inside the new nanotube is growing (arrowed) at the same speed as the tube. The MWNT continues to grow after (**E**) 180 and (**F**) 240 seconds of irradiation. At this point the MWNT has reached a length of 10 nm [34].

bon layers form, one inside the other, apparently extruding from the surface of the metal particle (Fig. 4.14D). The length of the incipient MWNT is already 5 nm after 420 seconds of irradiation (Fig. 4.14E), and after 502 seconds five extra internal walls are clearly observed just above the nanowire (Fig. 4.14F). During growth, the metal inner core appears to migrate in the opposite direction (downwards) of growth, presumably due to compressive forces inside the host tube [27]

Figure 4.15 shows an example of a MWNT formation involving a Co nanowire (*fcc* structure) core. The irradiation intensity during the experiment was approximately 150 A/cm^2. In this case, the formation of step edges appears significantly more pronounced (Figs. 4.15B and C). In addition to a new set of complete inner walls, an incomplete graphene layer also grows (arrow Fig. 4.15D) indicating that graphitic structures other than nanotubes can also be extruded in such a process.

4.5.3   Possible nanotube growth mechanism

Although one of the first growth models for catalyst-assisted carbon fiber growth (Baker *et al.* [30]) proposed carbon diffusion through the bulk of the particle followed by precipitation of carbon in the form of tubes or fibers, recent theoretical studies of the initial stages of CNT growth tend to disregard carbon bulk diffusion through the body of the catalyst because the energy barrier for carbon diffusion in bulk metal is higher than for carbon migration on a metal surface or along the metal-graphene interface [31, 36]. It is important to determine whether one or the other of these two mechanisms actually occurs or indeed whether both may occur and under what conditions, because the synthesis of CNTs with precise reproducible structure will heavily depend upon a deep understanding of the growth mechanism. Thus, a possible growth mechanism of CNTs for the particular experimental conditions seen in this section is proposed.

The solubility of carbon in pure Co or Fe is very low (atom ratio C/metal $< 10^{-3}$) at 600°C, so a continuous transfer of carbon atoms in low concentration through the metal must be assumed. The displaced carbon atoms that come from the walls of the host MWNT (the only carbon source), have maximum energies of approximately 70 eV (see Fig. 4.1), which is high enough to implant them underneath the surface layer in Co or Fe. Because of their low solubility in the metal, the injected C atoms leave the metal via fast bulk diffusion (the diffusion coefficient of C in *fcc* Co is 1.4×10^{-14} m^2/s) and precipitate at the surface. Surface diffusion of C atoms along the metal-tube interface is certainly possible but would lead to preferential growth of a shell adjacent to the inner MWNT layer. Although this is what is observed for SWNT growth in the Fe case (Fig. 4.13), for the Co case (Fig. 4.12), the distance between the inner layer of the MWNT and the part of the growing SWNT above the nanowire is 0.48 nm on one side and 0.63 nm on the other (Fig. 4.12B), much larger than the expected 0.34 nm. In the above examples, it is important to notice that all the layers of the forming MWNT segments (Figs. 4.14 and 4.15) grow simultaneously. It is difficult to visualize how such a process would be the consequence of only surface migration. Moreover, this fact supports the explanation that the nanotubes that appear to grow from the surface result from carbon migration *through* the metal

Figure 4.16: (Color) Possible carbon nanotube growth mechanism. (**A**) Carbon atoms are displaced from the MWNT host layers by the electron beam into the metal crystal and the hollow core; (**B**) the end face of the metal forms a dome, that simultaneously, appears covered by a hemispherical graphene cap that serves as the starting point of tube growth, and (**C**) a new nanotube grows from steps on the metal surface, and carbon atoms are fed from diffuse atoms through the metal particle [34].

particle.

From these observations a possible CNT growth scenario is summarized as follows (Fig. 4.16): 1)Electron irradiation causes displacement of carbon atoms from the host MWNT, and these atoms are directed either into the hollow core or into the metal crystal. 2)The flat end surface of the metal particle changes shape, forming a convex dome. 3)During the formation of the convex dome, apparently simultaneously, a curved layer of carbon, resembling a hemispherical fullerene structure, covers the dome-type particle surface. The formation of the dome, could be driven by pressure or parallel wetting effects such as those in mercury. 4)At the base of the dome, steps develop from where the walls of new MWNT segments sprout. The shape of the particle dome acts like a pattern for the new nanotube caps. 5)Carbon atoms are continuously fed into the metal, where they diffuse rapidly through the bulk and reach the root of the growing tube.

In addition, for Fe catalyst particles, the possibility of small carbide domains migrating through the crystal towards the end face of the metal, where they decompose and precipitate carbon material, should be considered (see 4.13.) Such scenario has been suggested by Schaper *et al.*, who observed the segregation of carbon at the end face of carbide crystals [37]. The preference of MWNT rather than SWNT growth seems to depend on the available space at the end face of the metal particle, because we observe SWNT formation when the space is < 5 nm and MWNTs grow from hollow regions > 5 nm.

This set of observations indicates that CNT growth is essentially the same whether the catalyst is Fe, Co or FeCo, and that the carbon atoms injected into the metallic cores migrate through the bulk (not only the surface) to the positions where the nanotubes sprout from the surface. This process is by no means fully analogous to the CVD growth, but the fact that very similar structures are obtained suggests that some of the detailed observations may also apply to the CVD process. More importantly, the process by itself may also provide new CNT synthesis pathways for large scale nanotube fabrication.

4.6   MWNT-metal-MWNT junctions

In Fig. 4.9 it was shown that the continued irradiation of a metal filled MWNT could lead to a junction, where two MWNT segments are joined by a metal particle. These type of structures, that from now on are termed MWNT-m-MWNT junctions (where the m stands for metal), are important to study because the use of CNTs in future electronic devices, among other parameters, will depend on the nature of nanotube-metal contacts, since this interface has a profound effect on charge transport [38].

In this section, a more detailed study is given on the formation process of such structures from MWNTs that contain encapsulated metal particles and are irradiated at high temperature with electrons. The rupture of MWNT-m-MWNT junctions under the electron beam is also discussed.

4.6.1   Formation of MWNT-metal-MWNT junctions

The formation of MWNT-m-MWNT junctions was achieved with the TEM beam, either by controlled irradiation of a metal filled MWNT with a beam diameter much larger than the tube diameter or by the precise irradiation of a small region of a metal filled MWNT with a beam diameter of the size of the tube diameter or smaller. For such small beam diameters, the current density can be as high as 10^4 A/cm^2, and the tube can be altered layer by layer (see Fig. 4.5C). During these experiments the temperature was maintained at 600°C.

Figure 4.17: MWNT-m-MWNT junction formed by irradiation with a beam diameter much larger than the tube diameter at 600°C. The metal particle seems to act like a joint between two MWNT segments. Scale bar: 5 nm.
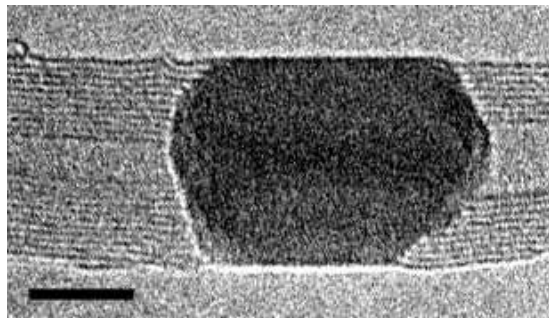
The first approach is depicted in Fig. 4.9 (point (f)). Producing such structure requires very long irradiation times ($\sim$ 100 minutes). Figure 4.17 provides more detail of the formed junction. The initially encapsulated FeCo nanowire is transformed to a piece of material that seems to act as a joint between two MWNT segments, one with 10 concentric cylinders and the other with 8. Apparently, the process is driven by the continuous breaking of the MWNT host layers. As the layers break, they leave space that is immediately filled with the encapsulated material.

MWNT-m-MWNT junctions are produced faster if the second approach is used. Figure 4.18 shows such a process for a Co@MWNT, where the electron beam was made to converge into a small region of the tube (and then expanded to take the images), causing breakage of the walls, and consequently reconstruction of the encapsulated material. The MWNT has 6 concentric layers, and the Co nanowire dimensions are 47.0 nm in length and 7.3 nm in diameter at the beginning of the experiment (Fig. 4.18A). Layers of the MWNT are damaged by irradiating one side of the tube with a small diameter beam, and the Co nanowire starts to deform (Fig. 4.18B). The reconstruction of the Co nanowire continues (Figs. 4.18C and D) and a MWNT-m-MWNT junction configuration is generated (Fig. 4.18E). The length of the Co particle is reduced to < 15 nm and the diameter increase to 12.7 nm (Fig. 4.18F), which is almost the same as the diameter of the initial MWNT (12.4 nm). Thus, the metal occupied the space vacated by the carbon layers. The complete process took only 13 minutes, much less when compared to the first approach to produce junctions.

The size of the starting nanowire does not seem to matter, as Fig. 4.19 shows. The initial FeCo nanowire has a length of approximately 150 nm (Fig. 4.19A), and after irradiation with a small diameter beam at the middle region of the nanowire,
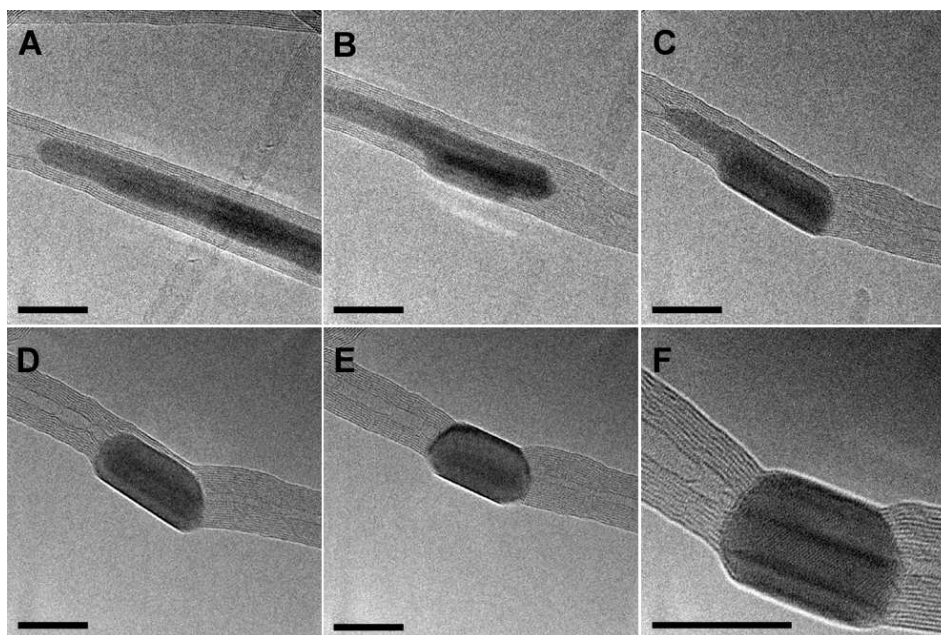
Figure 4.18: Formation of a MWNT-m-MWNT junction with a small diameter beam ($\sim$ 5 nm). (**A**) Co@MWNT sample at the beginning of the experiment. (**B**) The focused electron beam damages a side of the tube, and the Co nanowire is modified. The Co nanowire reconstruction continues for (**C**) 115 and (**D**) 237 seconds. Finally, the Co particle joins together two MWNT segments (**E** and **F**). Scale bar: 10 nm.
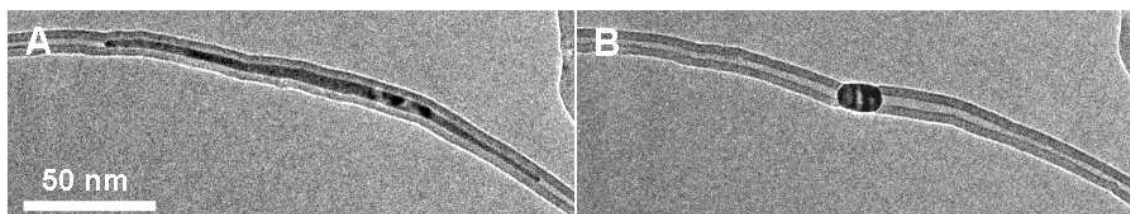
Figure 4.19: A large FeCo nanowire ($\sim$ 150 nm in length) contained in a MWNT transforms to a union particle in a MWNT-m-MWNT junction. FeCo@MWNT sample (**A**) before and (**B**) after irradiation with a small beam diameter.

a MWNT-m-MWNT junction is formed (Fig. 4.19B). Apparently, no strong interaction exists between the metal nanowire and the inner wall of the tube, since as soon as the disintegrating layers leave some open space, the encapsulated material slides freely to fill it, leaving a hollow region on both MWNT segments. It seems that the high aspect ratio (length/width) cylindrical structure of the metal is only sustained as long as there are carbon layers to contain it, in a metastable state.

A more detailed insight into the MWNT-metal interface in these junctions is
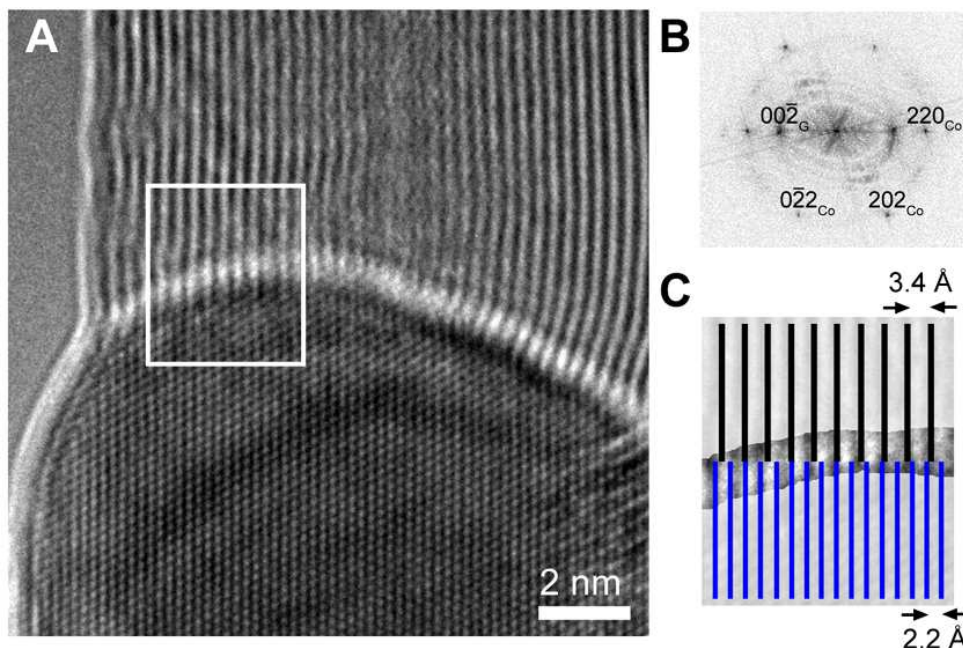
Figure 4.20: (Color) Details of a MWNT-metal intersection in a MWNT-m-MWNT junction. (**A**) Interface between the Co particle and the MWNT segment. (**B**) FFT of image (**A**). The FFT pattern agrees with the [111] zone axis of the Co *fcc* structure. (**C**) Scheme of the area marked in (**A**). Lines have been drawn to visualize planes. In order to compensate the mismatch between graphitic layers (black) and cobalt layers (blue) dislocations must occur at the interface (shown in the scheme).

shown in Fig. 4.20, where a Co particle forms the joint between the MWNT segments. The reciprocal space pattern of the interface (Fig. 4.20B), closely agrees with the [111] zone axis diffraction of the Co *fcc* structure. The set of planes (220) from the Co particle are aligned almost parallel to the graphitic layers, and thus to the tube axis. The length of 10 graphitic layers is 3.4 nm and the length of 16 Co (220) planes is 3.5 nm. Extrapolating the planes to the intersection zone, it is clear that dislocations in the Co particle must exist to compensate the mismatch between the metal-graphite layers distances (Fig. 4.20C).

The formation of MWNT-m-MWNT junctions seems to be driven by the surface minimization of the metal nanowires. The induced modifications expected for Co or Fe crystals under irradiation, with electron energies of 300 keV, certainly does not account for the complete reconstruction observed in the crystal nanowires. It is known that materials with surface tensions above 0.1 J/m^2 will not wet the surface

of CNTs [39]. The surface energy value for crystalline Fe or Co is approximately 2.5 J/m^2 [40]. Thus, once the disrupted layers of the MWNT cease forcing the nanowire shape, the metal will try to reduce its surface area in order to minimize energy. Since the metal particles are crystalline in the form of contained nanowires and, after irradiation, in the form of joints between MWNT segments, surface minimization most probably occurs by metal atom self-diffusion and diffusion of metal atoms through the metal-graphene interface.

4.6.2 Rupture of MWNT-metal-MWNT junctions

If electron irradiation is not stopped (or is increased), MWNT-m-MWNT junctions separate as shown in Fig. 4.21. Impressively, after almost two hours of irradiation (117 minutes), it seems that a layer of graphene remains enclosing the metal particle, and as the particle separates from the MWNT segment a cylindrical shell (resembling a SWNT, marked with an arrow in Fig. 4.21) serves as a bridge between the metal particle and the MWNT segment. Clearly, the particle was acting like
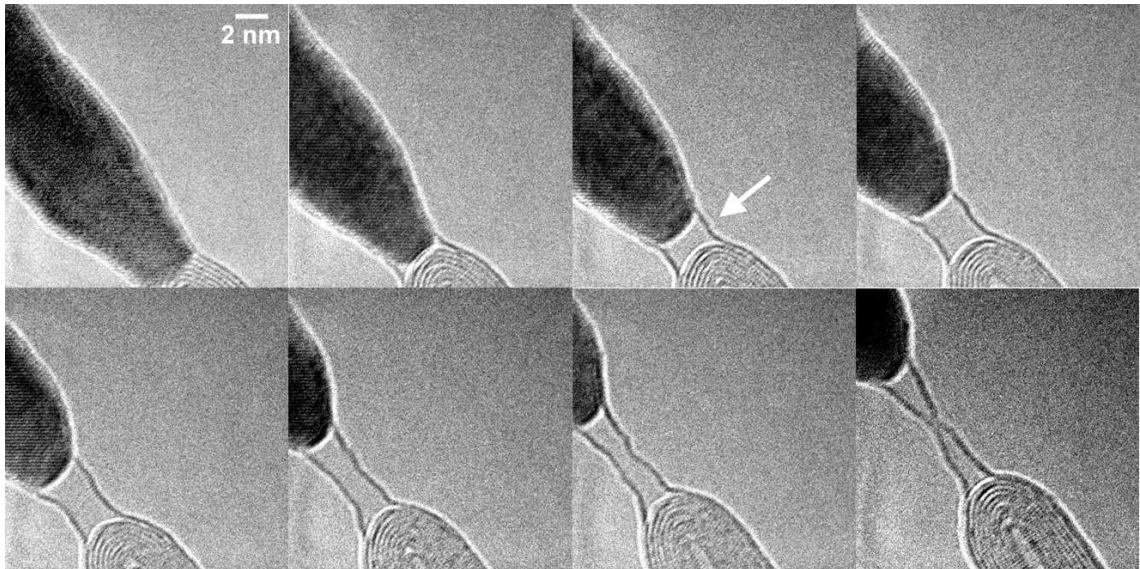
Figure 4.21: The series of images shows, from left to right and top to bottom, the evolution of a MWNT-m-MWNT junction before rupture. The time elapsed between the first and last frame is 175 seconds. The arrow marks the formation of a carbon cylindrical layer (resembling a SWNT) of 3 nm in diameter. In the series, lattice fringes show the crystalline state of the particle.
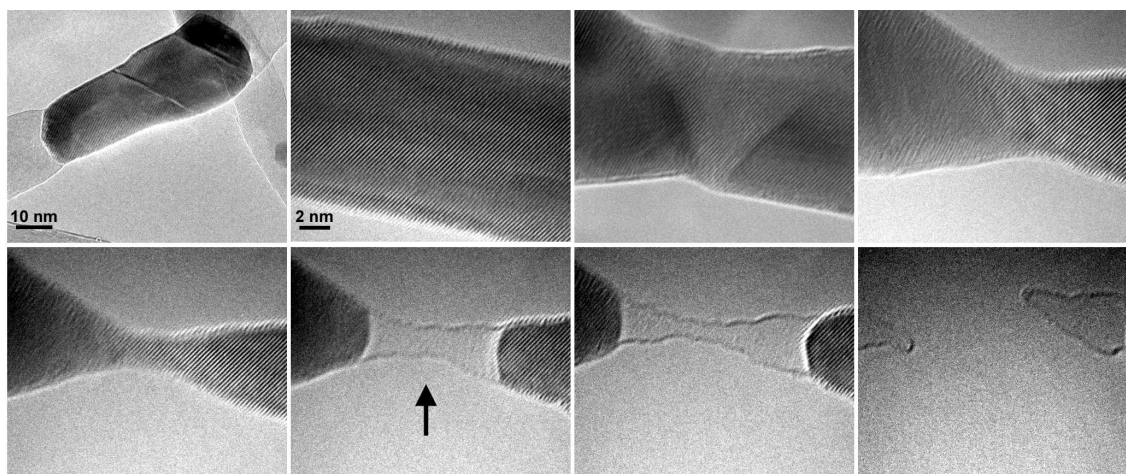
Figure 4.22: The series of images shows, from left to right and top to bottom, the evolution of a MWNT-m-MWNT junction before rupture. The time elapsed between the first and last frame was 422 seconds. The first frame shows a low magnification image of the complete junction. The arrow marks the formation of a SWNT.

a bridge between two separated segments, because the tip of the MWNT exhibits closed caps, with the exception of the outermost layer. As the separation between the particle and the tip of the MWNT segment increases, the SWNT elongates up to a distance of 10 nm. This elongation is accompanied by a reduction of the diameter, until finally the rupture of the nanotube joint occurs. The double cone morphology of the carbon layer observed just before rupture ("hour glass") has been reported before for hollow MWNTs and SWNTs under electron irradiation (cf. Fig. 4.5B), and for SWNTs under tensile stress [41].

In Fig 4.21 the rupture of the junction occurs at the MWNT-metal interface. However, rupture can occur in other regions of the junction. Figure 4.22 shows an example, where breakage occurs at the middle region of a FeCo metal particle. The first frame of the series of Fig. 4.22 depicts the complete junction, where a nanowire of 60 nm in length (displaying two dislocations) joins together two MWNT segments. The beam was made to converge into the middle region of the nanowire, which shows a slow elongation and thinning evolution, also seen in studies of quantum conductance in Au nanowires [42]. Again, a SWNT (mark with an arrow in Fig. 4.22) appears as the last bond between the two disrupting sections. The SWNT elongates up to 12 nm before rupture, where two closed carbon cones (one on each side) formed

(last frame Fig. 4.22).

In this case, the simplest explanation (that of a layer of carbon covering the metal particle) is less obvious. If this was the case, a perfect coupling between the deformation of the nanowire and the deformation of the layer should occur, since before the metal breaks no clear evidence of the carbon cylindrical layer standing alone or layer kinks caused by the abrupt reduction of diameter are observed in the images. Another possibility is that carbon atoms are diffusing on the nanowire surface, and when distortions are induced in the thinning region of the nanowire, these serve as sinks for the carbon atoms, which agglomerate to form the SWNT.

4.7   Coda: curvature in carbon nanostructures

As mentioned above, by reducing the electron beam diameter (reducing the spot size and focusing the beam with the condenser lens), the graphitic layers of carbon nanostructures can be modified with monolayer precision [21]. Figure 4.23 shows this effect for the outermost layers of a MWNT. The local removal of four layers observed in Fig. 4.23B is achieved with a focused beam of approximately 5 nm in diameter. To anneal dangling bonds left by the removal of material, the modified layers interact with their neighbors and form hairpin structures, introducing curvature in the structure. Several ways of restructuring defective graphene have been proposed; they involve the formation of pentagonal rings, leading to positive Gaussian curvature, and heptagonal or octagonal rings, leading to negative curvature of the graphene sheet.   Figure 4.24 shows another example of precise modification of carbon layers. With a focused electron beam (approximately 5 nm in diameter) two incisions, 5 nm in depth, were made on one side of a MWNT, 15 nm apart one from the other (Figs. 4.24B and C). In this experiment, the stiff metal nanowire prevents distortions of the MWNT caused by the incisions [21]. Open edges anneal by closing dangling bonds and forming hairpin structures. The center part between incisions is unstable and during its evolution in time the layers farthest away from the center of the tube, closed at their side by hairpin structures, could become at some point cylindrical, as shown in Fig. 4.24D (arrow), where a small double wall cross section
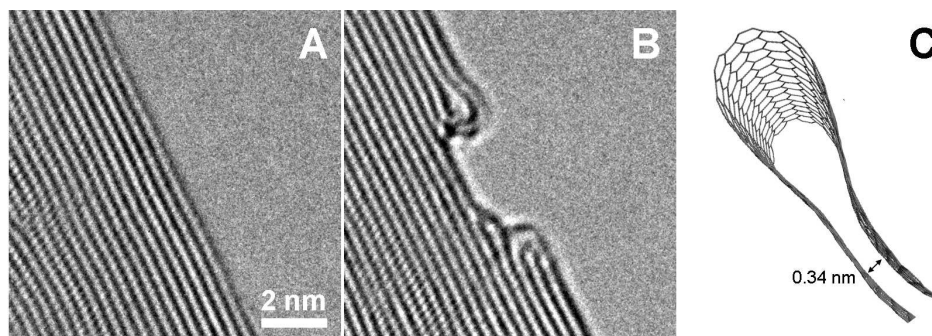
Figure 4.23: Removal of graphitic layers with a focused electron beam. (**A**) Carbon layers of a MWNT. (**B**) The outermost layers of the MWNT are locally removed with tangential electron irradiation. (**C**) Molecular model of the hairpin structure (Courtesy of H. Terrones).
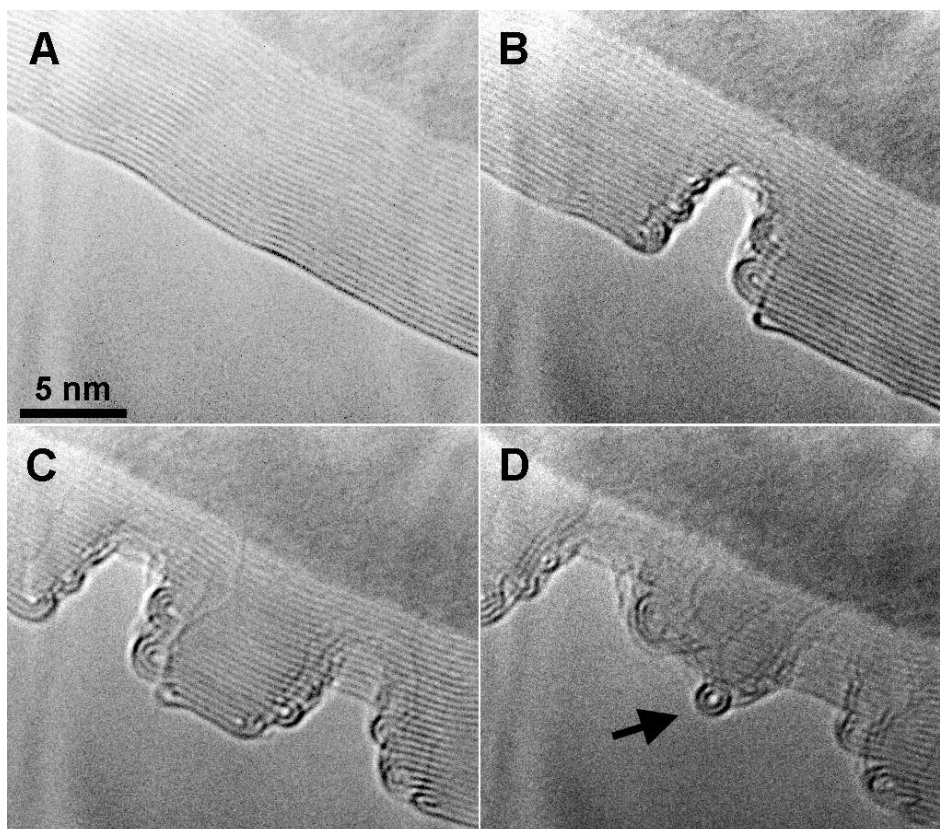
Figure 4.24: (**A**) Side of a 24 layer metal filled MWNT. (**B**) A 5 nm in depth incision is made with a beam of approximately 5 nm. (**C**) Another incision is made, 15 nm apart from the first. (**D**) The arrow marks a double wall cross section.

is observed.

Thus, one can think of electron irradiation as a tool to introduce curvature on carbon nanostructures and create even smaller nanosystems.

4.8   Conclusions

Controlled electron irradiation of carbon nanostructures inside a TEM can serve as a powerful tool to investigate structural modifications at the nanoscale. The production of defects in carbon nanostructures during irradiation can be inhibited by heating the sample at 600°C, which causes annealing of defects by lattice reconstruction.

In this chapter, it was shown that MWNTs can act as high-pressure cells when subjected to controlled electron irradiation at 600°C in a 300 kV TEM. Theoretical calculations estimate that the pressure experienced inside a MWNT could be as high as 40 GPa. In this way, solid materials (Co, FeCo, or Fe_3C) contained inside the core of MWNTs can be plastically deformed, extruded or even broken, and these effects can be monitored with high resolution microscopy. Besides pressure driven effects, irradiation effects in the crystal might occur and have to be considered.

Metal-filled MWNTs could also be used as solid-state reaction cells where nanotube growth can be monitored *in situ*. SWNT, as well as MWNT, growth was observed for different encapsulated metals (Fe, Co, FeCo), which proves the generality of the method. The experimental conditions are different from reports related to the monitoring of CVD-based nanotube growth (mainly using Ni as a catalyst). In the work presented here, the source of carbon comes from atoms extracted from the walls of a host MWNT by electron irradiation, as opposed to a gaseous carbon source. These carbon atoms are injected into the crystalline metallic wires that are responsible for extruding capped nanotubes via a bulk diffusion process.

In addition, metal-filled MWNTs can be converted to MWNT-metal-MWNT junctions, either by continued electron irradiation with a beam diameter larger than the MWNT diameter or by irradiation with a focused beam with a size of the MWNT diameter or smaller. If irradiation is not stopped, these junctions break, and a SWNT appears as the last interlink between the two disrupting sections. These type of junctions could be important in charge transport experiments, since the use of CNTs in electronic devices will depend on the quality of contact between CNTs and metals.

Finally, we showed that electron irradiation with the focused beam can induce

curvature in carbon layered materials. Point-like modifications of less than 5 nm can be produced, thus electron irradiation can be used as a tool to produce new morphologies using carbon nanostructures.

References

[1] F. Banhart. Irradiation effects in carbon nanostructures. *Rep. Prog. Phys.*, 62:1181–1221, 1999.

[2] D. B. Williams and C. B. Carter. *Transmission electron microscopy: a textbook for materials science*, chapter 4. Plenum press, 1996.

[3] F. Banhart, T. Füller, Ph. Redlich, and P. M. Ajayan. The formation, annealing and self-compression of carbon onions under electron irradiation. *Chem. Phys. Lett.*, 269:349–355, 1997.

[4] P. G. Lucasson and R. M. Walker. Production and recovery of electron-induced radiation damage in a number of metals. *Phys. Rev.*, 127:485–500, 1962.

[5] W. D. Callister. *Materials science and engineering: an introduction*, chapter 5. John Wiley & Sons, 2003.

[6] P. A. Thrower and R. M. Mayer. Point defects and self-diffusion in graphite. *Phys. Status Solidi (a)*, 47:11–36, 1978.

[7] E. Kaxiras and K. C. Pandey. Energetics of defects and diffusion mechanisms in graphite. *Phys. Rev. Lett.*, 61:2693–2696, 1988.

[8] P. O. Lehtinen, A. S. Foster, A. Ayuela, A. Kresheninnikov, K. Norlund, and R. M. Nieminen. Magnetic properties and diffusion of adatoms on a graphene sheet. *Phys. Rev. Lett.*, 91:17202, 2003.

[9] C. H. Xu, C. L. Fu, and D. F. Pedraza. Simulations of point-defect properties in graphite by a tight-binding-force model. *Phys. Rev. B*, 48:13273–13279, 1993.

[10] J. Koike and D. F. Pedraza. Dimensional changes in highly oriented pyrolytic graphite due to electron-irradiation. *J. Mater. Res.*, 9:1899–1907, 1994.

[11] D. Ugarte. Curling and closure of graphitic networks under electron-beam irradiation. *Nature*, 359:707–709, 1992.

[12] D. Ugarte. Formation mechanism of quasi-spherical carbon particles induced by electron bombardment. *Chem. Phys. Lett.*, 207:473–479, 1993.

[13] C.-H. Kiang, W. A. III. Goddard, R. Beyers, and Bethune D. S. Structural modification of single-layer carbon nanotubes with an electron beam. *J. Phys. Chem.*, 100:3749–3752, 1996.

[14] P. M. Ajayan, V. Ravikumar, and J.-C. Charlier. Surface reconstruction and dimensional changes in single-walled carbon nanotubes. *Phys. Rev. Lett.*, 81:1437–1440, 1998.

[15] F Banhart, J. X. Li, and A. V. Krasheninnikov. Carbon nanotubes under electron irradiation: stability of the tubes and their action as pipes for atom transport. *Phys. Rev. B*, 71:241408, 2005.

[16] N. G. Chopra, F. M. Ross, and A. Zettl. Collapsing carbon nanotubes with an electron beam. *Chem. Phys. Lett.*, 256:241–245, 1996.

[17] V. H. Crespi, N. G. Chopra, M. L. Cohen, A. Zettl, and S. G. Louie. Anisotropic electron-beam damage and the collapse of carbon nanotubes. *Phys. Rev. B*, 54:5927–5931, 1996.

[18] A. P. Burden and J. L. Hutchison. Real-time observation of fullerene generation in a modified electron microscope. *J. Cryst. Growth*, 158:185–8, 1996.

[19] M. Terrones, W. K. Hsu, J. P. Hare, H. W. Kroto, H. Terrones, and D. R. M. Walton. Graphitic structures: from planar to spheres, toroids and helices. *Phil. Trans. R. Soc. Lond. A*, 354, 1996. 2025-2054.

[20] F. Banhart and P. M. Ajayan. Carbon onions as nanoscopic pressure cells for diamond formation. *Nature*, 382:433–435, 1996.

[21] J. Li and F. Banhart. The engineering of hot carbon nanotubes with a focused electron beam. *Nano Lett.*, 4:1143–1146, 2004.

[22] A. V. Krashenininnikov, P. O. Lethinen, A. S. Foster, and R. M. Nieminen. Bending the rules: contrasting vacancy energetics and migration in graphite and carbon nanotubes. *Chem. Phys. Lett.*, 418:132–136, 2006.

[23] A. V. Krashenininnikov, F. Banhart, J. X. Li, A. S. Foster, and R. M. Nieminen. Stability of carbon nanotubes under electron irradiation: role of tube diameter and chirality. *Phys. Rev. B*, 72:125428, 2005.

[24] F. Banhart, J. Li, and M. Terrones. Cutting single-walled carbon nanotubes with an electron beam: evidence of atom migration inside nanotubes. *Small*, 1:953–956, 2005.

[25] J. P. Lu. Elastic properties of carbon nanotubes and nanoropes. *Phys. Rev. Lett.*, 79:1297, 1997.

[26] E. W. Wong, P. E. Sheenan, and C. M. Lieber. Nanobeam mechanics: elasticity, strength, and toughness of nanorods and nanotubes. *Science*, 277:1971–1975, 1997.

[27] L. Sun, F. Banhart, A. V. Krasheninnikov, J. A. Rodríguez-Manzo, M. Terrones, and P. M. Ajayan. Carbon nanotubes as high-pressure cylinders and nanoextruders. *Science*, 312:1199–1202, 2006.

[28] T. Frauenheim, G. Seifert, M. Elstner, T. Niehaus, C. Köhler, M. Amkreutz, M. Sternberg, Z. Hajnal, A. Di Carlo, and S. Suhai. Atomistic simulations of complex materials: ground-state and excited-state properties. *J. Phys.: Condens. Matter.*, 14:3015–3047, 2002.

[29] M. Zaiser. Self-compression and diamond nucleation in irradiated carbon onions - a theoretical model. *Mater. Res. Soc. Symp. Proc.*, 540:243, 1999.

[30] R. T. K. Baker and P. S. Harris. The formation of filamentous carbon. In *Chemistry and physics of carbon*, volume 14, pages 83–165. Marcel Dekker, New York, 1978.

[31] S. Helveg, C. López-Cartes, J. Sehested, P. L. Hansen, B. S. Clausen, J. R. Rostrup-Nielsen, F. Abild-Pedersen, and J. K. Nø rskov. Atomic-scale imaging of carbon nanofiber growth. *Nature*, 427:426–429, 2004.

[32] M. Lin, J. Pei Ying Tan, C. Boothroyd, K. Ping Loh, E. Soon Tok, and Y-L. Foo. Direct observation of single-walled carbon nanotube growth at the atomic scale. *Nano Lett.*, 6:449–452, 2006.

[33] R. Sharma and Z. Iqbal. *In situ* observations of carbon nanotube formation using environmental transmission electron microscopy. *Appl. Phys. Lett.*, 84:990–992, 2004.

[34] J. A. Rodríguez-Manzo, M. Terrones, H. Terrones, H. W. Kroto, L. Sun, and F. Banhart. In-situ nucleation of carbon nanotubes by the injection of carbon atoms into metal particles. *Nature Nanotechnology*, 2007. Accepted for publication.

[35] F. Banhart, Ph. Redlich, and P. M. Ajayan. The migration of of metal atoms through carbon onions. *Chem. Phys. Lett.*, 92:554–560, 1998.

[36] J.-Y. Raty, F. Gygi, and G. Galli. Growth of carbon nanotubes on metal nanoparticles: a microscopic mechanism from *ab initio* molecular dynamics simulations. *Phys. Rev. Lett.*, 95:096103, 2005.

[37] A. K. Schaper, H. Hou, A. Greiner, and F. Phillipp. The role of iron carbide in multiwalled carbon nanotube growth. *J. Catal.*, 222:250–254, 2004.

[38] N. Nemec, D. Tománek, and G. Cuniberti. Contact dependence of carrier injection in carbon nanotubes: an *ab initio* study. *Phys. Rev. Lett.*, 96:76802, 2006.

[39] E. Dujardin, T. W. Ebbesen, H. Hiura, and K. Tanigaki. Capillarity and wetting of carbon nanotubes. *Science*, 265:1850–1852, 1994.

[40] H. L. Skriver and N. M Rosengaard. Surface energy and work function of elemental metals. *Phys. Rev. B*, 46:7157–7168, 1992.

[41] M. A. L. Marques, H. E. Troiani, M. Miki-Yoshida, M. Jose-Yacaman, and Rubio. A. On the breaking of carbon nanotubes under tension. *Nano Lett.*, 4:811–815, 2004.

[42] V. Rodriguez, T. Fuhrer, and D. Ugarte. Signature of atomic structure in the quantum conductance of gold nanowires. *Phys. Rev. Lett.*, 85:4124–4127, 2000.

Chapter 5

Conclusions and future work

5.1 Conclusions

In this thesis, results are presented about three themes relating carbon nanostructures: 1) The magnetic response of carbon nanostructures that possess negative or positive Gaussian curvature. 2) The synthesis of CNTs and the encapsulation of metals within MWNTs. 3) The response of carbon nanostructures under electron irradiation.

1) It was found that sp^2 carbon nanostructures that contain polygons other than hexagons could show strong paramagnetic behavior, in contrast to graphite and aromatic molecules which are diamagnetic. This effect, studied only for π-electrons, is a consequence of the geometrical configurations of the non-magnetic carbon atoms.

The magnetic susceptibility of polymerized fullerenes formed by coalescing C_{60} and C_{70} molecules could reach values up to ~ 200 CGS p.p.m per mol C for the ring current magnetic susceptibility, which is more than the total magnetic susceptibility of graphite in absolute value.

Also, large paramagnetic moments of ~ 10 emu/g could be induced in corrugated nanotori formed from coalesced C_{60} molecules along the 5-fold axis of symmetry, with an applied magnetic field perpendicular to the tori plane of 1 kGs at low temperatures.

The doping of carbon nanostructures is an alternative to greatly alter their

magnetic properties. Low dopant concentrations of electrons or holes could induce diamagnetic-paramagnetic transitions in these carbon complexes.

2) SWNTs, MWNTs and CN_x were synthesized with the pyrolysis of aerosolized solutions method.

The SWNTs produced are metallic and semiconducting. It was found that an increment on the catalyst concentration inhibits the growth of smaller diameter SWNTs. Equally, an increase in the temperature of reaction promotes the growth of large diameter SWNTs. More crystalline SWNTs are obtained at high temperature ($\sim 950^\circ$C).

Yields of ~ 1 gr of MWNTs could be obtained in a single experiment by using toluene as the carbon source.

For CN_x, an increment in the time of reaction does not alter significantly the diameter distribution. Thus, it appears that the diameter of the CN_x is established at the initial steps of growth.

Encapsulation of Fe, Co, Ni and a FeCo alloy was achieved by using different metallocenes as the catalyst precursor. Results shown indicate that the filling of the metals increases at lower temperatures of reaction ($\sim 650^\circ$C).

3) The controlled electron irradiation of MWNTs inside a TEM at 600°C was used to induce pressure on encapsulated materials. It was shown that solid materials (Co, FeCo, or Fe_3C) contained inside the core of MWNTs can be plastically deformed, extruded or even broken, and the effects were monitored with high resolution electron microscopy. Theoretical calculations estimate that the pressure experienced inside a MWNT could be as high as 40 GPa.

In addition, SWNT and MWNT growth was observed during electron irradiation of MWNTs containing encapsulated metals (Fe, Co, FeCo), inside the TEM. In this process, displaced carbon atoms by the electron beam are injected into the crystalline metallic wires that are responsible for extruding capped CNTs via a bulk diffusion process.

Metal-filled MWNTs were converted to MWNT-metal-MWNT junctions by elec-

tron irradiation inside the TEM. The rupture of such junctions was observed. Interestingly, a SWNT is formed at the very last last moment before rupture.

5.2 Future work

Further research on the magnetic response of curved carbon nanostructures should include an extension of the London theory to 3D carbon systems. The recent synthesis of a magnetic carbon foam still asks for a theoretical explanation. In this context, the electron spin variable should be considered, and this could be done by using more robust calculations. Much needs to be done experimentally in order to clarify the magnetic response of curved carbon structures. Steps in this direction should explore the transformations that C_{60}@SWNTs and CNTs undergo when irradiated with different radiation sources like electrons, ions or high energy lasers. Also, the formation of coil-like structures from C_{60}@SWNTs could be explored.

The pyrolysis of aerosolized solutions for CNT growth offers the possibility to produce alternating layers of different types of MWNTs. In this way, novel MWNT forests could be used in developing the spinning technique to produce complex carbon fibers. In addition, alternating layers of MWNTs containing different metals could be produced, and the magnetic properties of such structures should be investigated. The temperature dependence on the filling rate of metals inside MWNTs could be studied, in order to better understand the filling mechanism.

Electron irradiation of carbon nanostructures presents a great opportunity to modify their structure with great precision at the nano-scale. In particular, *in situ* modifications achieved inside the TEM could benefit from local measurements of physical properties such as conductivity and mechanical properties. This could be realized nowadays with the use of a nanomanipulator stage mounted in the TEM. In this way, measurements of properties before and after electron irradiation could be monitored with atomic resolution. Although *in situ* modifications inside the TEM provide a deep understanding at the atomic level of the processes involved in the

modification of carbon nanostructures, further studies should explore the possibility of irradiating larger areas of already patterned carbon nanostructures, like MWNTs and SWNTs forests. This could be realized with available technology. Finally, the growth of CNTs by injecting carbon atoms into catalyst particles should be explored with more depth, both theoretically and experimentally. Since the catalyst particles in this process remain in their crystalline state, studies of the relationship between crystal plane directions and carbon diffusion paths could help in resolving the problem of producing CNTs with desired chiralities.

Published articles

1. **Induced ring currents in polymerized C_{60} and C_{70} molecules**. F. López-Urías, J. A. Rodríguez-Manzo, M. Terrones, and H. Terrones. *Journal of Computational and Theoretical Nanoscience* , 4:252-256 (2007).

2. **Anomalous paramagnetism in doped carbon nanostructures**. J. A. Rodríguez-Manzo, F. López-Urías, M. Terrones, and H. Terrones. *Small*, 3:120-125 (2007).

3. **The elastic deformation of nanometer-sized metal crystals in graphitic shells**. L. Sun, J. A. Rodríguez-Manzo, and F. Banhart. *Applied Physics Letters*, 89:263104 (2006).

4. **Magnetic response in finite carbon graphene sheets and nanotubes**. F. López-Urías, J. A. Rodríguez-Manzo, E. Muñoz-Sandoval, M. Terrones, and H. Terrones. *Optical Materials*, 29:110-115 (2006).

5. **Decorating carbon nanotubes with nanostructured nickel particles via chemical methods**. P. Ayala, F. L. Freire, Jr., L. Gu, David J. Smith, I. G. Solórzano, D. W. Macedo, J. B. Vander Sande, H. Terrones, J. A. Rodríguez-Manzo and M. Terrones. *Chemical Physics Letters*, 431:104-109 (2006).

6. **Carbon nanotubes as high-pressure cylinders and nanoextruders**. L. Sun, F. Banhart, A. V. Krasheninnikov, J. A. Rodríguez-Manzo, M. Terrones, and P. M. Ajayan. *Science*, 312:1199-1202 (2006).

7. **Efficient anchoring of silver nanoparticles on N-doped carbon nanotubes**. A. Zamudio, A. L. Elías, J. A. Rodríguez-Manzo, F. López-Urías, G.

Rodríguez-Gattorno, F. Lupo, M. Rühle, D. J. Smith, H. Terrones, D. Díaz, and M. Terrones. *Small*, 3:346-350 (2006).

8. **Magnetism in Fe-based and carbon nanostructures: theory and applications**. H. Terrones, F. López-Urías, E. Muñoz-Sandoval, J. A. Rodríguez-Manzo, A. Zamudio, A. L. Elías, and M. Terrones. *Solid State Sciences*, 8:303-320 (2006).

9. **Pyrolytic synthesis of long strands of large diameter single-walled carbon nanotubes at atmospheric pressure in the absence of sulphur and hydrogen**. F. Lupo, J. A. Rodríguez-Manzo, A. Zamudio, A. L. Elías, Y. A. Kim, T. Hayashi. M. Muramatsu, R. Kamalakaran, H. Terrones, M. Endo, M. Rühle, and M. Terrones. *Chemical Physics Letters*, 410:384-390 (2005).

10. **Production and characterization of single-crystal FeCo nanowires inside carbon nanotubes**. A. L. Elías, J. A. Rodríguez-Manzo, M.R. Mc-Cartney, D. Goldberg, A. Zamudio, S. E. Baltazar, F. López-Urías, E. Muñoz-Sandoval, L. Gu, C. C. Tang, D. J. Smith, Y. Bando, H. Terrones, and M. Terrones. *Nano Letters*, 3:467-472 (2005).

11. **Magnetism in corrugated carbon nanotori: the importance of symmetry, defects, and negative curvature**. J. A. Rodríguez-Manzo, F. López-Urías, M. Terrones, and H. Terrones. *Nano Letters*, 11:2179-2183 (2004).

12. **Shape and complexity at the atomic scale: the case of layered materials**. H. Terrones, M. Terrones, F. López-Urías, J. A. Rodríguez-Manzo, and A. L. Mackay. *Phil. Trans. Roy. Soc. A.*, 362: 2039-2063 (2004).

144